People's Democratic Republic of Algeria

Ministry of Higher Education and Scientific Research

Mohamed Boudiaf University of M’sila - M'sila

Faculty Of Sciences

Physics Department

Serial number: ……………………….

Enrolment number: D.PHM/3C/02/17

Thesis

Submitted for the diploma of

3rd cycle Doctorate degree

Major : Physics

THEME

Development of phosphocalcic bioceramics from natural phosphate

Presented By:

KHERIFI Djelel

Defended on:17/06/2021

In front of the jury composed of:

Name & First name	Grade	Establishment	Quality
DEGHFEL Bahri	Professor	Univ. of M'sila	President
BELHOUCHET Hocine	Professor	Univ. of M'sila	Supervisor
RAMESH Singh	Professor	Univ. of Malaya	Co-supervisor
IBRIR Miloud	Professor	Univ. of M'sila	Examiner
KOLLI Mostafa	Professor	Univ. of Setif 1	Examiner

Academic year: **2020 /2021**

Dedicates

To my parents, may God give them health and long life...

To my dear sister and brothers

To all my family

To all my teachers

To all my friends

To all those who are dear to me...

Djelel kherifi

Thanks

Praise be to God for the success in the realization and completion of this project.

I would like to express my sincere gratitude to my supervisors Pr. BELHOUCHET Hocine and Pr. RAMESH Singh; I am grateful to them for having directed my work while leaving me free to explore my ideas. I thank them for their advice, opinions, help, and guidance throughout this thesis and for being present and motivating.

It is an honor for me that Prof. DEGHFEL Bahri has accepted to chair the jury.

My sincere thanks go to Prof. IBRIR Miloud for accepting to participate as an examiner in this jury.

My thanks also go to Prof. KOLLI Mustafa from Farhat Abbas University - Sétif 1 for having accepted to examine this work.

My sincere thanks also go to my parents for their infinite patience and provide me with an ideal working environment. This project was made possible thanks to their support.

I am deeply grateful to all the members of the LPCM lab, especially Pr. SAHNOUNE Foudil and HERAIZ Menad for their valuable advice, opinions, and help.

My great thanks also go to all those who have helped me in any way, notably the engineers and professors at the LPCM lab and all my colleagues in the Physics department.

I cannot also fail to express with tenderness all my gratitude to my close relations for their precious help, their comfort, and their practical encouragements: in particular KENZOUR Abdelghani and DJEMLI Amar.

I thank Dr. Mohamed Kamel Abbas and Dr. Marjan very much: the E.Lab Pn Hartini, Shokri, and Zaman "CAREF Members" from the Faculty of Engineering, University of MALAYA-Malaysia. For their hospitality, respectful treatment, and valuable help.

Finally, I would like to express my deepest thanks to all the academic and administrative staff of the Physics department, University of MOHAMED Boudiaf - M'sila.

Contents

Contents

Introduction

General Introduction

Bioceramics have been used in surgery either as a support or as a replacement element. Over the last few decades, these bioceramics have become important in the field of biomaterials for orthopaedic use and have shown interesting bioactivity and osteoconduction properties.

The body's assimilation or rejection of these materials depends on their compatibility with the tissues and their chemical, physical, and mechanical properties.

Calcium phosphate is among the bioceramics widely used in biomedical applications as bone substitutes to repair defective hard tissue due to their favorable characteristics (composition and properties), which are very similar to those of the mineral part of the human skeleton. Indeed, among calcium phosphates family members, we find hydroxyapatite (HAp, $Ca_{10}(PO_4)_6(OH)_2$), fluorapatite (FAp, $Ca_{10}(PO_4)_6F_2$), and tricalcium phosphate (β-TCP, $Ca_3(PO_4)_2$), which are excellent candidates as biomaterial ceramics for biomedical applications, because of its multiple properties such as its exceptional biocompatibility in the biological environment, its osteoconductivity and osteoinductivity with the surrounding tissues.

The aim is to replace the bone with implants made of hydroxyapatite and β-tricalcium phosphate, which promote bone regrowth. However, their fragility, poor mechanical strength, and small defects limit their use in biomechanical and highly mechanically stressed areas. In fact, fluorapatite has Physico-chemical properties close to those of bone and presents quite good mechanical properties compared to β-TCP alone and hydroxyapatite. Moreover, the presence of fluorine slows down the appearance of tooth decay.

Therefore, several works have been carried out to synthesize a high-temperature stable Fluoroapatite (FAP), either as a single-phase or as a phase of a composite material.

Indeed, FAp crystallizes in many commercial glass-ceramics and biomedical ceramics. Besides, the FAp-Anorthite biphasic system is studied in vitro, and it has shown excellent bioactivity and biocompatibility. Other oxides such as ZrO_2 and Al_2O_3 are added to FAp, and their effects on mechanical properties are studied.

According to the US Geological Survey, Algeria ranks third (after China and Morocco) in world reserves of rock phosphate. At the same time, its production is very low (third before last). In order to valorize the Djebel El-Onk deposit, rock phosphate mixtures are reinforced by different content of several oxide additions, namely: quartz, Titania, and alumina.

The conventional method of elaboration was followed to synthesize dense composites and study the mechanical and biological properties and the change of these composites' mineralogical composition following each oxide's addition.

To present the results obtained during this study, we have chosen to divide this thesis into three parts.

In this context, the first part is focused on a bibliographical study. An effort has been made to summarize biomaterials' essentials and their applications, natural phosphates, fluorapatite, and biocomposites on alumina, quartz, and FAp.

The main experimental equipment and techniques used in the elaboration, preparation, and characterization and the various initial materials used along this work are discussed in the second part of this thesis.

The third part consists in turn of two parts:

The first part is devoted to the preparation and study of phosphate-quartz mixtures. Thus, the treatment of these mixtures and the characterization at each stage of the research during this part are detailed and discussed.

The second part is reserved for studying the effect of the TiO_2 mass fraction on the morphological, mineralogical, and mechanical properties of alumina/natural phosphate composites.

Finally, we conclude by showing the main results achieved by this study.

Chapter 1

Bibliographic overview

Part I. Biomaterials

I.1. History and definition of biomaterials

Native bone tissue has a nanocomposite structure, which is composed primarily of non-stoichiometric hydroxyapatite (HAp; $Ca_{10}(PO_4)_6(OH)_2$) and collagen fiber matrix, that provides appropriate physical and biological properties, particularly mechanical support and protection for the vertebrate skeleton. When the bone is damaged, it must be repaired or regenerated. Biomaterials were first created by humans using a combination of natural materials such as wood, glue, rubber, and tissues from living organisms and manufactured materials such as iron, gold, zinc, and glass. The reactions of the hosts to these materials were highly diverse [1]. The body tolerated some materials while rejecting others; the body accepted some materials under certain conditions (host tissue characteristics and surgical procedure). In contrast, the same materials were rejected in another situation.

These and other products were used to help treat damaged or missing tissue before establishing the principles of aseptic surgical technique by Lister in 1860. Still, the results were not always the best for patients. Biomaterials are technically applicable as a result, and because of them, biomaterials became theoretically useful, with a high probability of success in contact with the body [1-4]. As a significant and dynamic field, its confined and rapid changes have influenced modern medicine and therapeutics in various ways over the last decade [1, 2]. For example, in the reconstruction period after World War II, restoring the consequences of this global catastrophe was somehow beneficial to provide a powerful driving impetus to advance in this field. As a result, innovators treating painful arthritic joints started by restoring joint mobility and function with corrosion-resistant metals [3]. Unlike ancient civilizations and previous implants, this time, the production of these materials is focused on scientific science, which enabled the field of biomaterials to be developed up in the 1950s, which would not have been possible otherwise.

Various bone grafts and bone graft replacements are currently used for surgical procedures, including autografts, allografts, and synthetic bone grafts [1, 3], where existing graft materials and synthetic grafts for fracture repair can be enhanced. As a result, there's a lot of demand for healthy and safe tissue regeneration materials [4]. Today, "biomaterials" is a maturing field of research [3]. Its market has been steadily growing, with millions of patients benefiting from biomedical materials' success [5], where the demand in the surgical market is highlighted by the fact that there are approximately four million operations involving bone grafting or bone substitutes performed around the world annually [2].

The development path chosen by engineers (scientific research) to advance in this field requires the overlap of several disciplines [1]. With this wide range of integrated disciplines, it is clear that the field of biomaterials is moving from the category of fundamental disciplines to the category of multidisciplinary sciences [3]. There are always concepts, assumptions, and criteria that generate generations of biomaterials in maturing the biomaterials field. These concepts, beliefs, and criteria result from several factors, including the reactivity of the materials implanted in the body or otherwise the metabolic responses to the existence of these materials within the body and the intended application of these materials.

On this basis, many definitions of the term biomaterial can be found, including:

- According to the Clemson University Advisory Board for Biomaterials, a biomaterial is "a systemically and pharmacologically inert product intended for implantation inside or integration with living systems."
- They are generally "non-living materials used in a medical device intended to interact with biological systems." (From the Chester Conference of the European Biomaterials Society 1986).
- A biomaterial is used to create devices that replace a part or element of the body in a healthy, durable, cost-effective, and physiologically appropriate manner [6].
- Primarily these materials are defined as ″natural or synthetic substances intended to replace or assist a damaged biological system, or introduced into a living tissue ″ that can settle temporarily and/or permanently in the human body. They are used to support or replace human cells or tissues; the term "biomaterial" refers to materials in contact with the body for a minimum of 3 weeks [7].

According to these concepts, to create and use biomaterials in medicine and dentistry, one must have a broad field of knowledge or collaborate with people from various specialties, as shown in table I.1 and table I.2 summarises significant advancements in the implants field. Many more advancements have been made in recent years.

Table I.1: Knowledge Fields of Biomaterials Development [8].

Discipline	Examples
Science and engineering	Materials sciences: structure-property relationship of synthetic and biological materials including metals, ceramics, polymers, composites, tissues (blood and connective tissues), etc.
Biology and physiology	Cell and molecular biology, anatomy, animal and human physiology, histopathology, experimental surgery, immunology, etc.
Clinical sciences	All the clinical specialties: dentistry, maxillofacial, neurosurgery, obstetrics and gynecology, ophthalmology, orthopedics, otolaryngology, plastic and reconstructive surgery, thoracic and cardiovascular surgery, veterinary medicine, and surgery, etc.

Table I.2: Notable Developments Relating to Implants [9].

Year	Investigators	Development
Late 18-19th century		Various metal devices to fix bone fractures; wires and pins from Fe, Au, Ag, and Pt
1860-1870	J. Lister	Aseptic surgical techniques
1886	H. Hansmann	Ni-plated steel bone fracture plate
1893-1912	W.A. Lane	Steel screws and plates (Lane fracture plate)
1912	W.D. Sherman	Vanadium steel plates, first developed for medical use; lesser stress concentration and corrosion (Sherman plate)
1924	A.A. Zierola	Introduced Stellites (CoCrMo alloy)
1926	M.Z. Lange	Introduced 18-8sMo stainless steel, better than 18-8 stainless steel
1926	E.W. Hey-Groves	Used carpenter's screw for femoral neck fracture
1931	M.N. Smith-Petersen	First femoral neck fracture fixation device made of stainless steel
1936	C.S. Venable, W.G. Stuck	Introduced Vitallium® (19-9 stainless steel), later changed the material to CoCr alloys
1938	P. Wiles	First total hip replacement prosthesis
1939	J.C. Burch, H.M Carney	Introduced tantalum (Ta)
1946	J. and R. Judet	First biomechanically designed femoral head replacement prosthesis. First plastics (PMMA) used in joint replacements

The 1940s	M.J. Dorzee, A. Franceschetti	First used acrylics (PMMA) for corneal replacement
1947	J. Cotton	Introduced Ti and its alloys
1952	A.B. Voorhees, A. aretzta, A. B. Blackmore	First successful blood vessel replacement made of cloth for tissue ingrowth
1958	S. Furman, G. Robinson	First successful direct heart stimulation
1958	J. Charnley	The first use of acrylic bone cement in total hip replacement on the advice of Dr. D. Smith
1960	A. Starr, M.L. Edwards	First commercial heart valves
The 1970s	W.J. Kolff	Total heart replacement

I.2. Biomaterials' behaviors in the body

Biocompatibility is defined as "the ability of a material to behave in a particular application with a positive and acceptable host response" [10], and it is an important property for a biomaterial. A biomaterial's biological evaluation typically requires two steps: in vitro and in vivo. Although a direct in vivo study of the host tissue response to a scaffold material would be ideal, the high complexity of in vivo processes can make understanding a particular cellular response difficult. Therefore, rather than testing the complex response in vivo, isolated cell lines' responses to a biomaterial are evaluated in vitro, allowing for a controlled analysis of a particular cellular response to a test material.

The expertise acquired in vitro can be used to adapt the material to the host site, making screening a new biomaterial much easier. Still, it cannot completely replace in vivo testing.

The type of tissue response at the interface is directly related to the mechanism of tissue attachment. Depending on the type of tissue reaction at the material and tissue interface, there are four types of materials (table I.3), and fig I.1 resumes the reactivity of biomaterials in vivo as a function of implantation time. A few surgical therapeutics do not use biomaterials to encompass the diverse range of material applications that exist today and develop many advanced tissue engineering and hybrid artificial organ applications that use living cells [1].

From the previous, a multidisciplinary science is known as biomaterials science" can be defined as the collection of physical, chemical, and biological studies of materials and their interactions with the biological environment. The overall goal of these studies and the most intense development and investigation have been directed towards the synthesis, optimization, and characterization of new biomaterials in the organism (receptor) to understand the organism's interactions with a biomaterial designed newly [1]. Most biomaterials incorporate non-specific and stereotyped biological interactions, which are the starting point and fundamental to creating these materials. Considerable effort is being put into developing engineered surfaces that could cause rapid and very precise reactions with cells and proteins, tailored to a specific application, directing those reactions that are unavoidable in the right direction.

Table I.3: Various types of materials and tissue response at material with tissue interface [1].

	Type of material	Tissue response
Toxic		Death of the surrounding tissue
Non-toxic	Biologically inactive (bioinert)	Formation of a fibrous tissue
	Biologically active (bioactive)	Formation of an interfacial bond
	Dissolves or degrades (biodegradable)	Replacement of the surrounding tissue

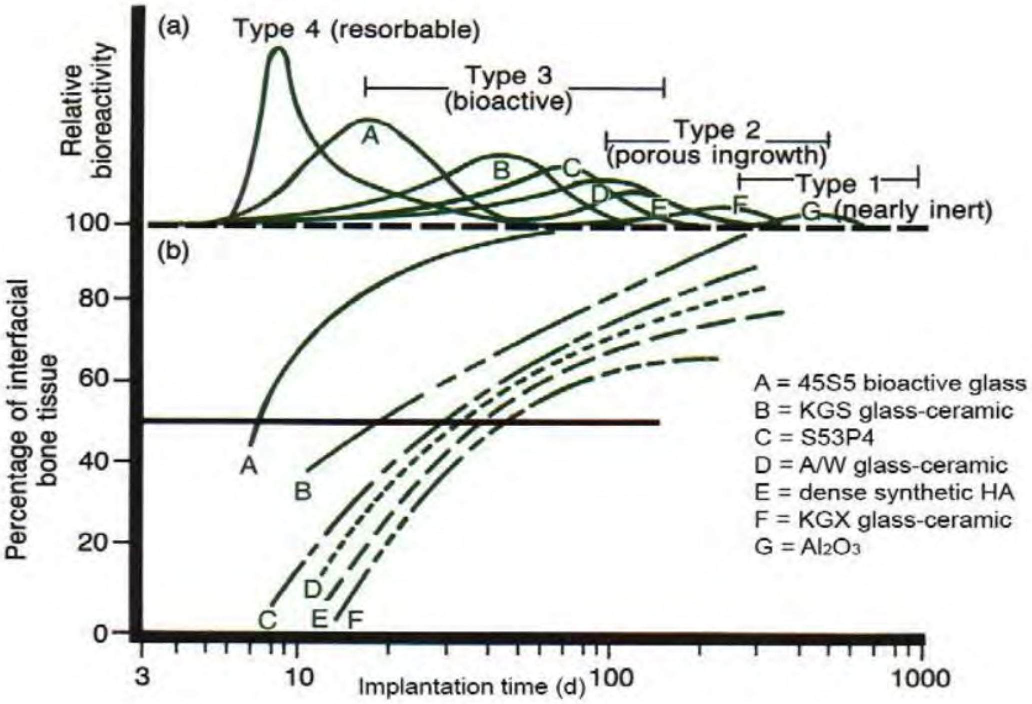

Fig I.1: Reactivity of biomaterials in vivo as a function of implantation time[1, 11].

I.3. Classes and applications of biomaterials

Each field of biomaterials comprises various materials depending on the application's requirements (the conditions under which these materials work). It can be classified according to the family of materials (materials) in which the biomaterial is made. There are five families of materials used as biomaterials [4, 11]:

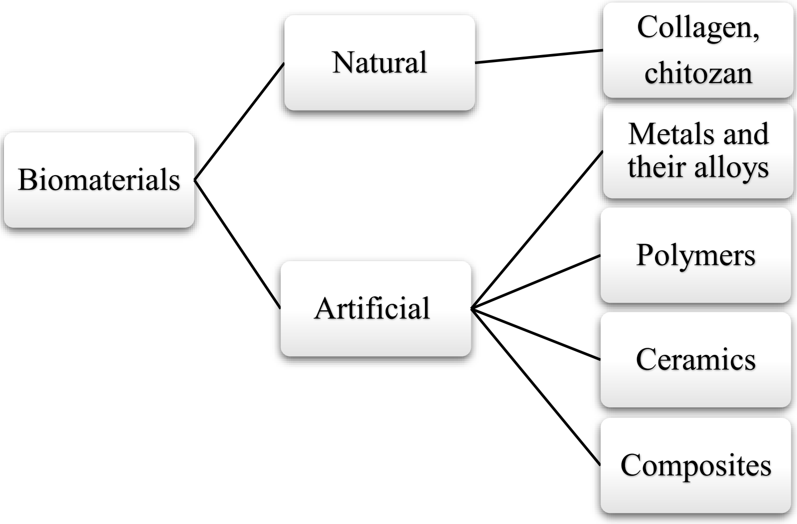

Fig I.2: A diagram representing the classification of biomaterials according to their nature.

I.3.1. Natural biomaterials

Materials of natural (biological) origin are one of the types of resources for biomaterials. They are divided into biomaterials of plant origin (polysaccharides, cellulose, etc.) and biomaterials of animal origin (chitin, collagen, bovine bone, etc.) [12].

I.3.2. Metals and their alloys

It is the first family of materials from which the first biomaterials were made [3]. From the point of view of osteogenesis and biocompatibility, titanium and its alloys are widely used among the known metallic biomaterials, because in addition to their common properties with stainless steels, titanium alloys have mechanical properties close to those of bone, without forgetting the shape memory alloys based on Ti-Ni alloys [12], and Mg alloys [13, 14], . Table I.4. below summarises some examples of metal alloys with their mechanical properties [1].

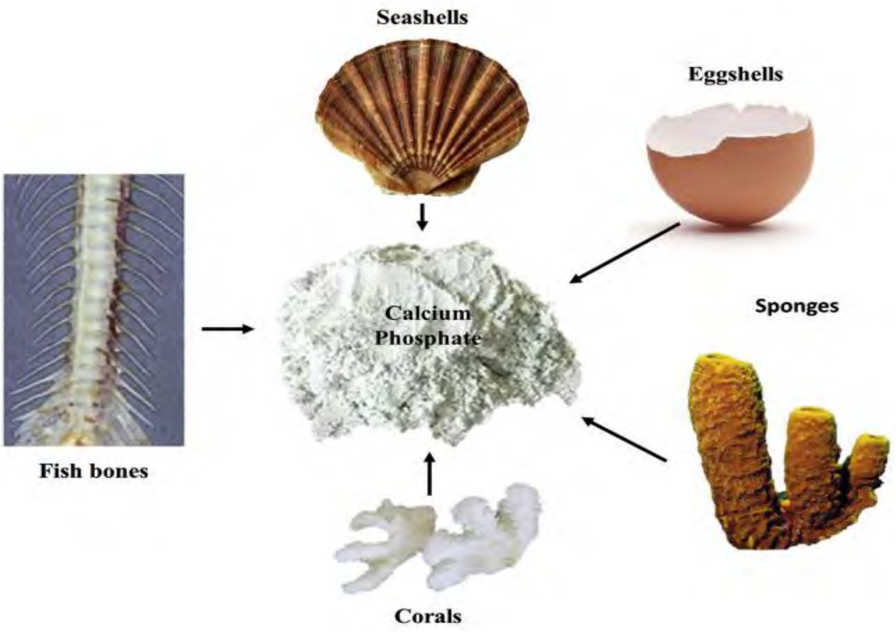

Fig I.3: Some sources of calcium phosphate [15].

Table I.4: Examples of metal alloys widely used as biomaterials [1].

Materials	Designation ASTM	Production conditions	Young's modulus (GPa)	Yield strength (MPa)	Tensile strength (MPa)	Fatigue at 107 cycles, R=-1 (MPa)
Stainless steel	F745	Annealing	190	221	483	221-280
	F55, F56, F138, F139	Annealing	190	331	586	241-276
		Cold-formed	190	792	930	310-448
		30% (in the case of the latter, it's the case of the former)	190	1213	1351	820
Co-Cr alloy	F75	Cold Forged	210	448-517	655-889	207-310
		Cast/annealed	253	841	1277	725-950
	F799	P/M HIP	210	896-1200	1399-1586	600-896
	F90	Hot forged	210	448-648	951-1220	-
		Annealing	210	1606	1896	586
	F562	Cold deformed	232	965-1000	1206	500
		44	232	1500	1795	689-793 (axial tension R=0.05, 30 Hz)
		Hot forged				
		Cold working matured				
Ti alloy	F67	Cold worked 30% Grade 4	110	485	760	300
	F136	Hot forging	116	896	965	620
			116	1034	1103	620-689

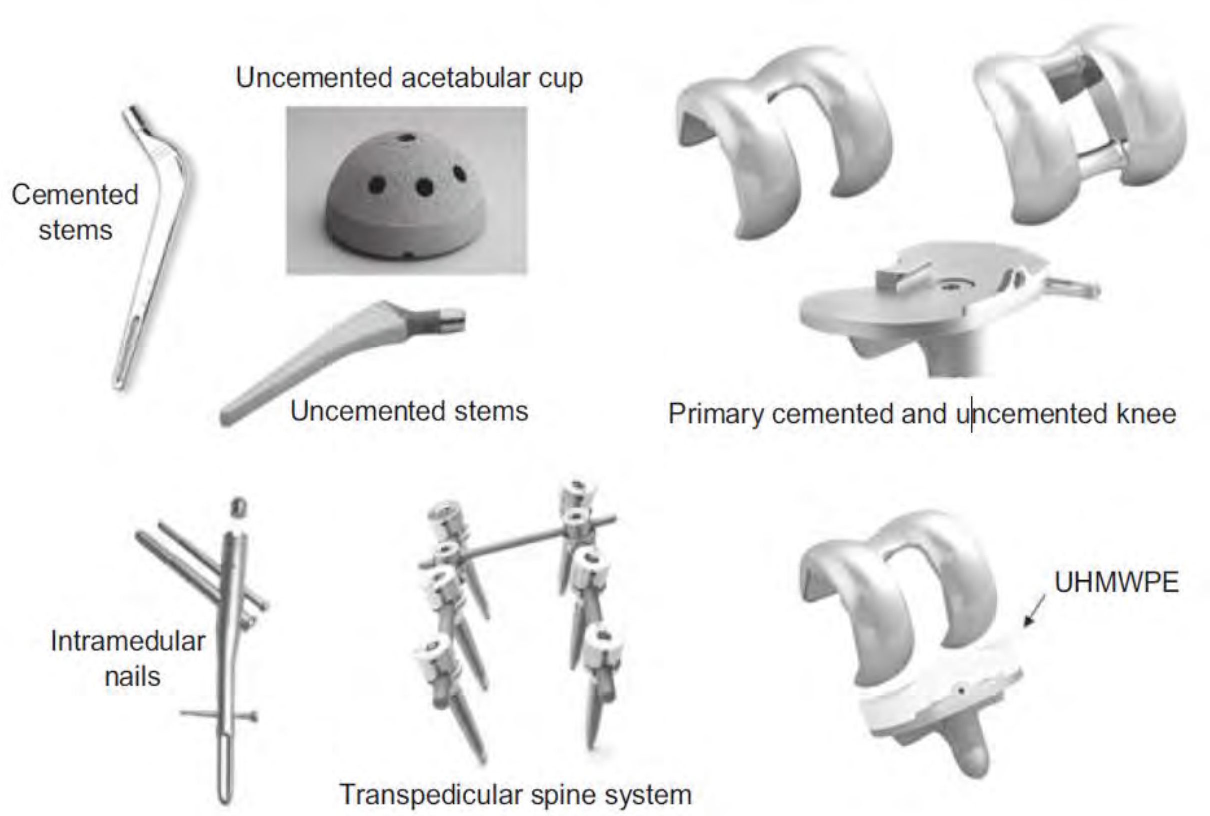

Fig I.4: Photography showing different metallic prosthesis components [1].

I.3.3. Polymers

Since their properties (such as porosity, degradation time, and mechanical characteristics) can be customized for particular applications, synthetic polymers are extremely useful in the biomedical field. They are often less costly than natural polymers, and they can be manufactured in broad, predictable quantities with a long shelf life. This family of materials has significantly expanded since the first use of PMMA as a biomaterial in 1930 [3], which can now be used in several applications, namely, dental and orthopedic cement, ophthalmology, ...etc. [3].

Other polymers are used such as LDPE, HDPE, UHMWPE, e-PTFE, PP, polyesters, polyamides (nylons), PU, siloxanes (silicones), polyetheretherketone (PEEK), in a wide range of biomedical devices, including restorative dentistry, soft tissue reconstruction, orthopedic implants and vascular structures [3]. Table I.5 lists the polymers used with some physical properties (crystallinity, glass transition, and melting temperature).

Table I. 5: Examples of polymers widely used as biomaterials [1].

Polymer	Monomer	Morphology	T_g (° C)	T_f (° C)
Polyethylene (PE)	$-(C_2H_4)-$	Semi-cristalline	-80	125-135
Polypropylene (PP)	$-(CH_2.CH.CH_3)-$	Semi-cristalline	-10	125-167
	$-(C_2F_4)-$	Semi-cristalline	-70	340
Polytetrafluoroethylene (PTFE)	-(RC=OOR ')-	Semi-cristalline	50-70	250-265
Polyester (PET)	$-(C_5O_2H_8)-$	Amorpha	118	-
Polymethylmethacrylate (PMMA)	$-(R_1-O-C=ONR_2R_3)-$	Amorphe /Semi-cristalline	-80 à 140	240
Polyurethane (PU)	$(NHCO(CH_2)_4CONH(CH_2)_6)-$	Amorphe /Semi-cristalline	45	190-350

I.3.4. Ceramics

Ceramic biomaterials are ceramics intended for biomedical use in general [11]. Whether bio-ceramic, bio-glass, or bio-vitro-ceramic, the members of each of these three subgroups, with their non-metallic/inorganic compositions as well as their physicochemical properties, offer a multitude of applications in several biomedical fields, including dentistry, orthopedics, and medicine in general (inert ceramics, for diagnostic instruments and endoscopy) [1]. There are several classifications of ceramics, namely: category based on shape, composition, and reactivity. According to the latter category, three types of ceramics are distinguished: inert ceramics, degradable ceramics, and reactive ceramics [15].

The first ceramics used are inert bioceramics (otherwise the first generation of ceramics used in biomedicine), especially in total hip and knee replacement [3]. In the case of bioresorbable bioceramics, the tissue's natural reconstruction is accompanied by the implant's simultaneous resorption. Such implants' mechanical properties decrease as the material resorbs unless the loss of mechanical properties due to resorption is compensated for by implant host tissue gain. The rate of biodegradation is a function of material bulk density, PH, crystallinity [12].

I.3.5. Composite materials

The term "composite" is usually reserved for materials. The distinct phases are separated at a scale larger than the atomic scale. Properties such as modulus of elasticity are significantly altered compared to those of a homogeneous material [16]. The human body's anatomical structures consist of hard and soft tissue that differ drastically in composition, structure, and properties yet integrate and function together efficiently and harmoniously. Due to their ability to mimic the extracellular matrix structure, composite biomaterials have been developed to solve clinical cases in which non-healing conditions prevent tissue repair.

It should be noted that there are composite materials of natural origin such as wood, bone, dentin, cartilage, skin, and natural foams (lung, cancellous bone, and wood) [17], as well as synthetic composite biomaterials, namely: PMMA/ UHMWPE fibers, PE/ HA particles [17]. Like all biomaterials classes, the biocomposite must be biocompatible [16, 18], as well as each component of the matrix or reinforcement being biocompatible[16]. The interface between the different components (reinforcement/matrix) must also not be degradable in vivo [3, 16]. Table I.6 summarizes examples of the most commonly used bio-composites with their applications, and fig I.5 resume some clinical applications of biomaterial [19].

Table I. 6: Examples of composites widely used as biomaterials [2].

The Field of application	Matrix/reinforcement
External fixation	Epoxy resin/ carbon fiber
Fractured bone fixation plates	Epoxy resin/ carbon fiber
Pins and screws	PMMA/ carbon fibre, PSU/ carbon fibre PP/ carbon fibre, PE/ carbon fibre PBT/ carbon fibre, PEEK/ carbon fibre PEEK/GF, PLLA/Hydroxyapatite PLLA/ PLLA fibre, PGA/PGA fibre
Spinal surgery	PU/bioverre, PSU/bioverre PEEK/carbon fiber, Hydrogels/PET fibre
Bone cement	PMMA/HA particles, PMMA/glass beads Calcium phosphate/aramid PMMA/UHMWPF fibers

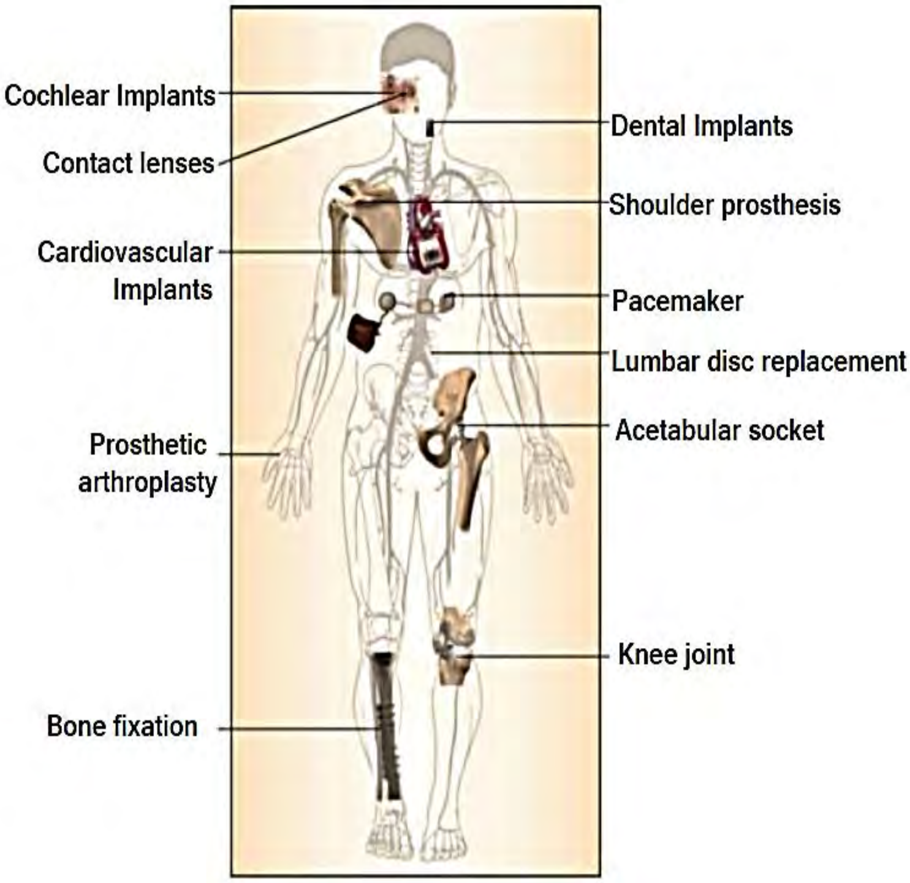

Fig I.5: Some clinical applications of biomaterial [19].

I.4. Bioceramics

As we mentioned in the first part, there are four main families of materials: metallic materials, polymers, composites and ceramics, polymers, composites, and ceramics.

The use of minerals and polymers for biomedical applications has encountered problems of weak bonding at the interface of the prosthesis and the surrounding tissue. For these reasons, the research has focused on ceramic materials known for their hardness, chemical inertness, and wear resistance [20].

Bio-ceramics are used in many biomedical applications, especially reconstructive surgery, either as a support or as an alternative. They are needed to restore the function of diseased or damaged calcified tissues (bone or teeth) for the body, repair and/or replace human organs.

Ceramics are the only bioactive and bioresorbable materials among inorganic substances. A bioactive ceramics occupy an intermediate position between bioinert and bioresorbable [21]. When a substance causes a particular biological reaction at the material–tissue interface, such as forming biochemical bonds between living tissue and the material, it is called bioactive.

I.4.1. Definition of bioceramics

Bioceramics are non-metallic, non-organic materials that require sintering heat treatment [22]. They are characterized by a high melting temperature, rigidity, lightness, heat resistance, excessive brittleness, and high chemical inertia, determining their application fields [23]. These bioceramics are also characterized by excellent friction properties (surface finish, wettability) and the absence of sensitivity to electrochemical corrosion. These materials are designed for various specific biomedical applications, particularly in implantable systems, due to their properties and good biocompatibility. They can have structural functions such as joint replacements or tissue replacements. They can also be used as coatings to improve metallic implants' biocompatibility and fixation [24].

I.4.2. Classifications

In terms of bioceramic reactivity within the living body, we can roughly divide the categories of bioceramics into bioinert, bioactive, and resorbable ceramics [16]. Reactivity, instead of chemical composition or crystallinity, is a better criterion for classifying bioceramics. For example, in the field of amorphous ceramics, it is possible to obtain glasses with the same chemical framework that behave as bioinert, bioactive, or resorbable due to composition differences [25].

I.4.2.1. Inert bioceramics

The concept of these biomaterials refers to the material's stable behavior concerning the host tissue. They show little or no reaction to the biological environment, but they cause an inflammatory reaction immediately after the operation. They are frequently used in the manufacture of heart valves or joint prostheses, where properties such as durability and stability are very important [26].

I.4.2.2. Bioactive bioceramics

The term bioactive bioceramics refer to biomaterials designed to create or modulate biological activity [27]. They exhibit chemical activity in relation to the physiological environment. They possess ions commonly found in bone (calcium Ca^{2+}, phosphate PO_4^{3-}, magnesium $Mg^{2+,}$ sodium Na^+), and they are characterized by the creation of a biological bond between the material and the bone. This results in an adhesion phenomenon capable of transmitting forces.

Although their surface properties are essential, their fragility their fragility and poor mechanical strength limit their use. These biomaterials, often based on calcium phosphate, have a chemical formula close to that of tissues (bone or teeth), and They can be used alone or sprayed on other materials (hydroxyapatite coating on femoral stems). The two main representatives of this family of compounds are bioveres and hydroxyapatite ($Ca_{10}(PO_4)_6(OH)_2$, HAp) [23].

I.4.2.3. Bioresorbable bioceramics

A bioceramic is considered resorbable when its solubility is such that the implant's rapid degradation occurs in the body; they are usually composed of elements such as calcium and phosphorus that are easily metabolized [28].

On the other hand, these ceramics accompany the development of the new tissue. Bone reconstruction and implant resorption coincide. As the bioceramic dissolves in the physiological medium, its porosity increases, allowing the tissue to grow back into the implant. Such implants progressively lose their mechanical properties as the material resorbs unless the loss of mechanical properties due to resorption is compensated by the gain of those of the implant host tissue. Among this bioceramic type, we find those based on tricalcium phosphate, which is the most commonly used. Other ceramics intended for specific use are mainly used as bone substitutes. Other ceramics for a particular service are primarily used as bone substitutes and are part of orthopaedic, maxillofacial, and plastic surgeons' daily practice. Examples are natural materials such as calcium carbonates and calcium phosphates which belong to this family of bioceramics.

Table I.7 summarizes the properties and applications of these different types of bioceramics.

Table I.7: The properties and applications of different types of bioceramics [26].

Type of bioceramic	In vivo reactivity	Examples	Clinical applications
Bioinert	Isolated by a nonadherent fibrous capsule	-Al_2O_3, ZrO_2	-Bearing-surface total joint arthroplasty components: hip implants (ball and cup), knee prosthesis, Bone screws, Maxillofacial and alveolar ridge reconstruction, Dental implants, crowns, and brackets, and inlay Ossicular bone substitutes, cochlear replacement Ophthalmology.
		-Carbons	

			- Heart valve coatings, Orthopedics implants
Bioactive	Tightly bonded to living tissues	-Hydroxyapatite (HA), pure and substituted -Hydroxycarbonate apatite (HCA) -Glasses: by melting and sol-gel -Glass-ceramics: A/W glass-ceramic and Ceravital	- Fixation or revision arthroplasty - Filler in periodontal defects Bone graft substitutes & cranial repair. - Endosseous alveolar ridge maintenance - Middle ear prosthesis - Vertebral prostheses - Iliac crest prostheses
Resorbable	Dissolved after a specific time	-Calcium phosphate -Calcium sulfate -Coralline $CaCO_3$	- Bone graft substitutes, cell scaffolds - Surface coatings on a total joint prosthesis - Bone graft substitutes

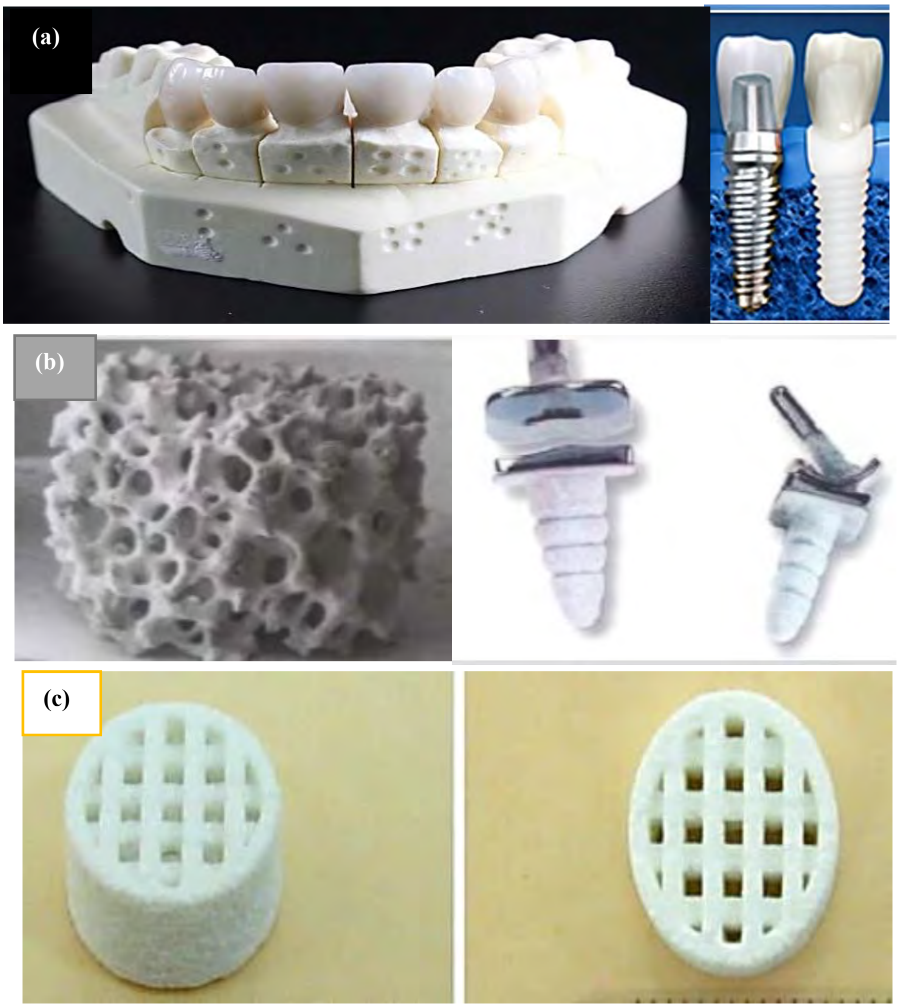

Fig I.6: some examples of bioceramics: (a) inert [26], (b) resorbable [27], (c) bioactive[28].

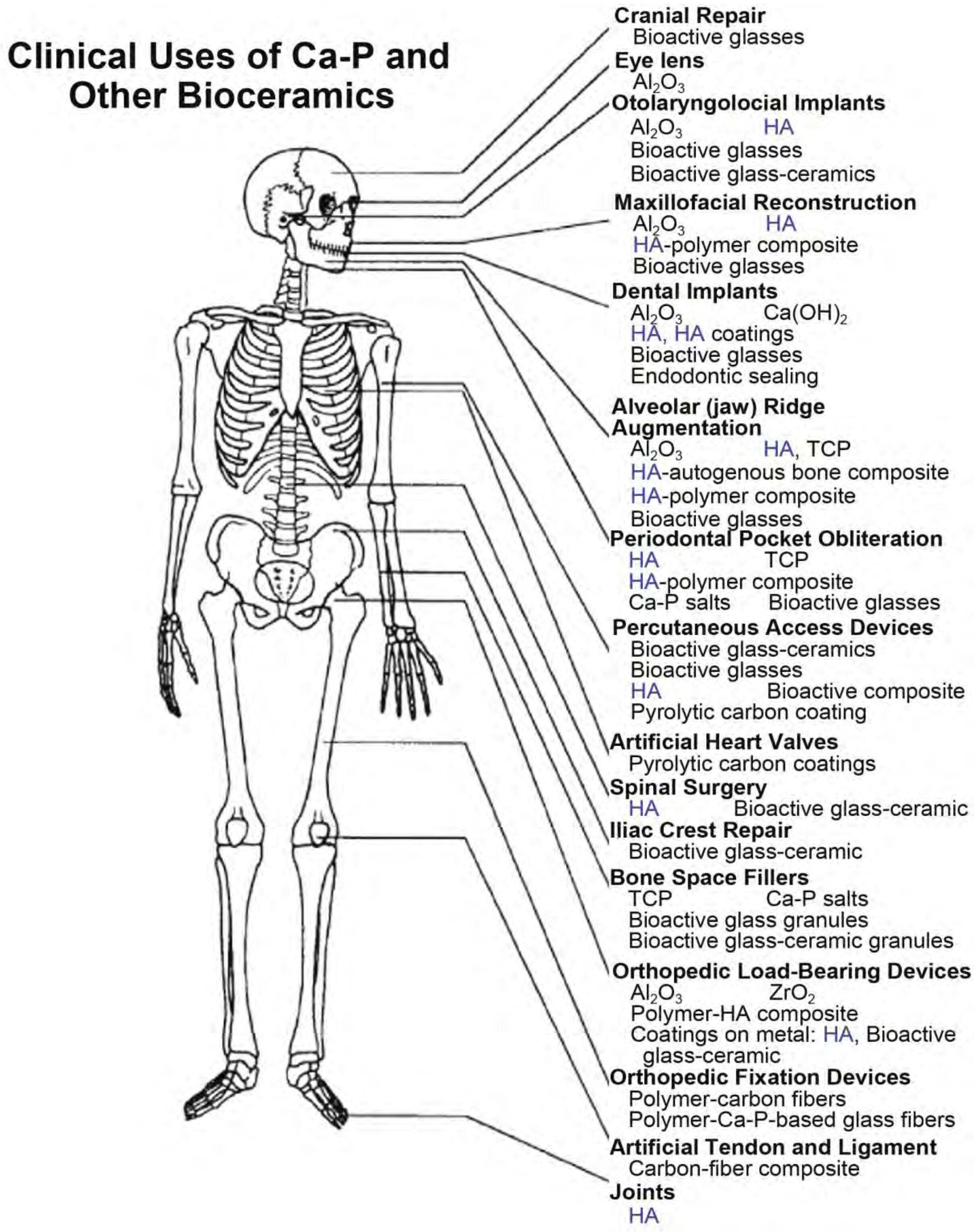

Fig I. 7: the most commonly used bioceramics for replacement or enhancement of skeletal and other elements of the human body [21].

Part II. Calcium Phosphate

For decades, mineralogists, chemists, material researchers, biologists, and clinicians have been very interested in calcium orthophosphates (abbreviated as $CaPO_4$). They were discovered in 1769 and have been investigated since then [29]. The reasons for this are apparent: they are the minerals that make up the principal component of bones and teeth.

As a result, $CaPO_4$ appears to be a biologically friendly inorganic, and it is increasingly being used as an implantable biomaterial for a variety of bone fillers and substitutes. Finally, $CaPO_4$ minerals are abundant in nature and provide the world's phosphorus supply, especially phosphates.

Calcium phosphate ceramic biomaterials have been thoroughly researched and used in several medical fields, including dentistry, orthopaedics, and facial surgery. The use of various calcium phosphates is dependent on properties such as absorption ability and bioactivity.

II.1. The behavior of calcium orthophosphates in solution

The solubility of calcium phosphates is sensitive to pH, which is essential for various applications in different fields, including agrochemical and biochemical. Table I. 8 summarises some physicochemical properties of the main calcium orthophosphates [30, 31]. The wide range of variation of the solubility constant of PAHs and PAFs is due to the strong affinity of these apatites to substitution, hence the change in their physicochemical behavior in solution.

In neutral or alkaline solution, the order of stability (insolubility) is as follows: hydroxyapatite > β-tricalcium phosphate > octacalcium phosphate > dicalcium phosphate (monetite) > dicalcium phosphate dihydrate (brushite) > monocalcium phosphate [30]. In general, calcium phosphates' solubility increases when the Ca:P molar ratio of the compound decreases. The solubility of $CaPO_4$ in water decreases drastically from left to right, HAp being the most insoluble and stable phase, as shown in fig I.8 [32]. Below pH 4.8, however, monetite and brushite are the most important stable and insoluble phases, although these acid salts dissolve incongruously in water [30, 31]. In fact, H_2PO^{4-} containing compounds only form under acidic conditions and are only present in mineral systems. At most, those containing both HPO_4^{2-} and PO_4^{3-} are also present in minerals, also in bones and teeth, and are stable in acidic environments. On the other hand, hydroxyapatite, which contains the OH^- anion in its formula, is considered the most basic calcium phosphate and is the most stable member of its family in basic or even neutral media [31]. These bioactive products make interactions with the biological environment's cells and liquids, ensuring quality integration. Their biocompatibility is also well known. They have no immunological or toxic effects on the tissues, and they do not give any reaction to foreign bodies.

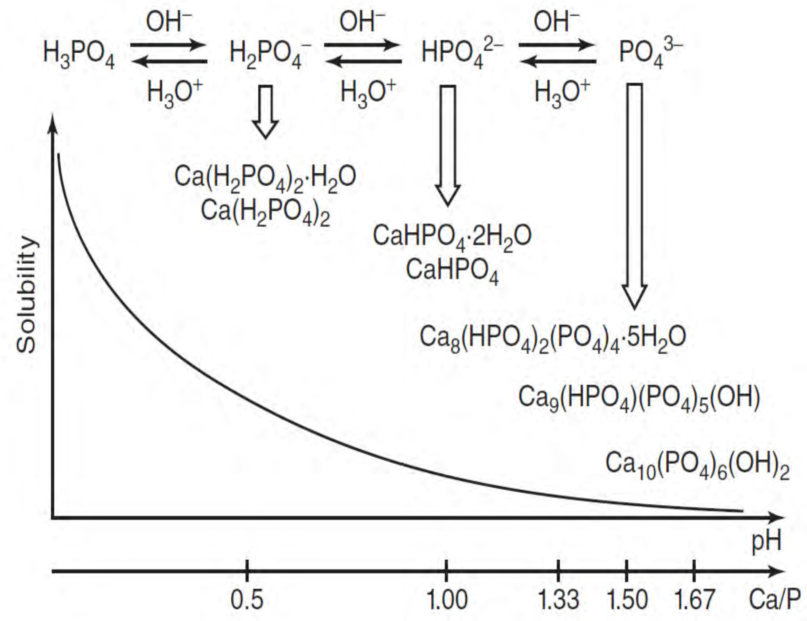

Fig I. 8: Various types of $CaPO_4$ obtained by neutralizing orthophosphoric acid by calcium hydroxide [32].

Table I. 8: Physico-chemical characteristics of natural and synthetic calcium orthophosphates [30, 31].

Formula	**Compound**	**-log Ksp at 25 °C**		**Ca/P**	**Density (g/cm^3)**
		Synthétiques	**Naturelles**		
$Ca(H_2PO_4)_2.H_2O$ (MCPM)	Monocalcium phosphate monohydrate	1.14	-	0.5	2.23
$Ca(HPO_4)$, $2H_2O$ (DCPD)	Dicalcium phosphate dihydrate	6.59 - 6.61	6.59	1	2.3
$Ca(HPO_4)$ (DCPA)	Dicalcium phosphate anhydrous	6.90	-	1	2.93
$Ca_8(PO_4)_4(HPO_4)_2,5H_2O$ (OCP)	Octacalcium phosphate	46.9 - 96.6	-	1.33	2.67
$Ca_8(PO_4)_4(HPO_4)_2$		-	48.7 – 94	1.33	-
α-$Ca_3(PO_4)_2$ (α-TCP)	α-Tricalcium phosphate	25.5 – 28.9	-	1.5	2.86

β-$Ca_3(PO_4)_2$ (β-TCP)	β-Tricalcium phosphate	28.9	28.9	1.5	3.07
ATCP	Amorphous calcium phosphates	25.5	-	1.5	-
$Ca_{10}(PO_4)_6(OH)_2$ (HAp)	Hydroxyapatite	4.33 - 116.8	58.64 – 125.18	1.67	3.16
$Ca_{10}(PO_4)_6F_2$ (FAp)	Fluorapatite	121	59.5 – 136	1.67	3.16
$Ca_{10}(PO_4)_6O$ (OAp)	Oxyapatite	~69	-	1.67	~3.2
$Ca_4(PO_4)_2O$ (TTCP)	Tetracalcium phosphate	38	-	2	3.05

II.2. Calcium Orthophosphate family members

There are twelve non-ion-substituted calcium orthophosphates with Ca/P molar ratios ranging from 0.5 to 2.0 (table I. 8) in the ternary aqueous system (CaO-P_2O_5-H_2O) Fig I. 9 [33].

Fig I. 10 [34] shows an anhydrous phase diagram of CaO-P_2O_5 at temperatures between 200 and 2200°C. Some of them may be used in the food industry in terms of applications, and calcium orthophosphates of food-grade quality are classified as an E341 additive in the European classification of food additives. Below is a list of all known calcium orthophosphates (table I. 8), with a short description of each.

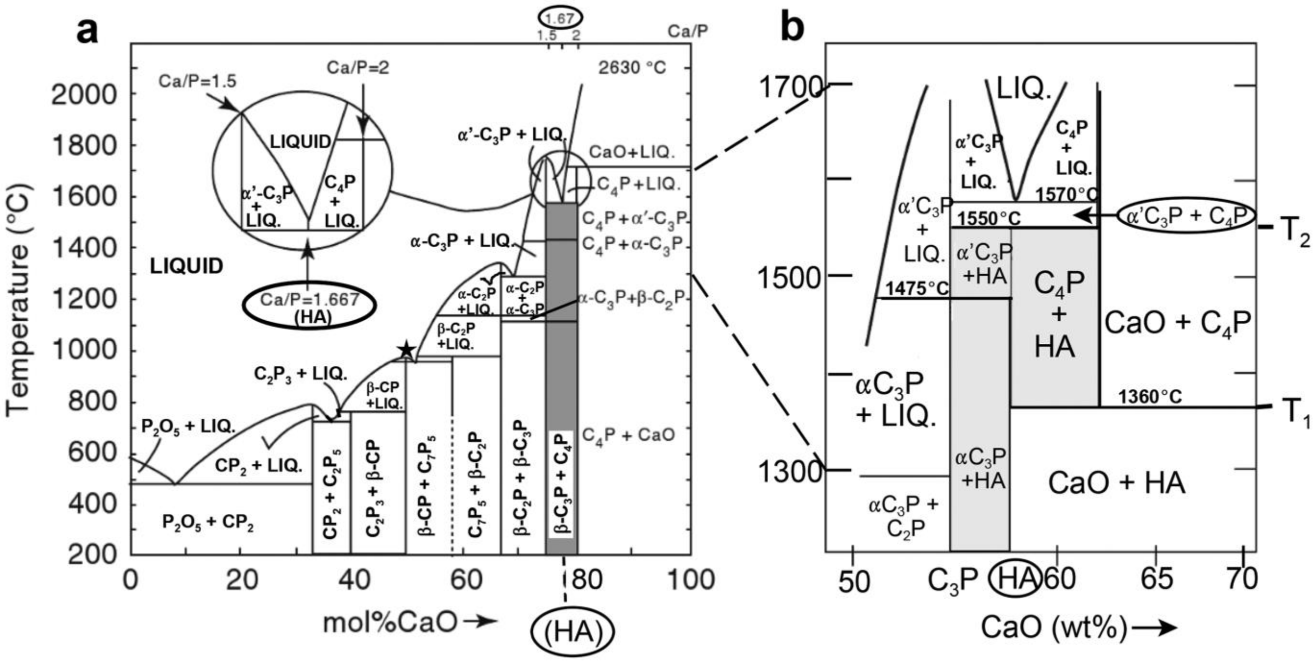

Fig I. 9: Phase diagram of the system CaO–P_2O_5 (C = CaO, P = P2O5)

at elevated temperatures [34].

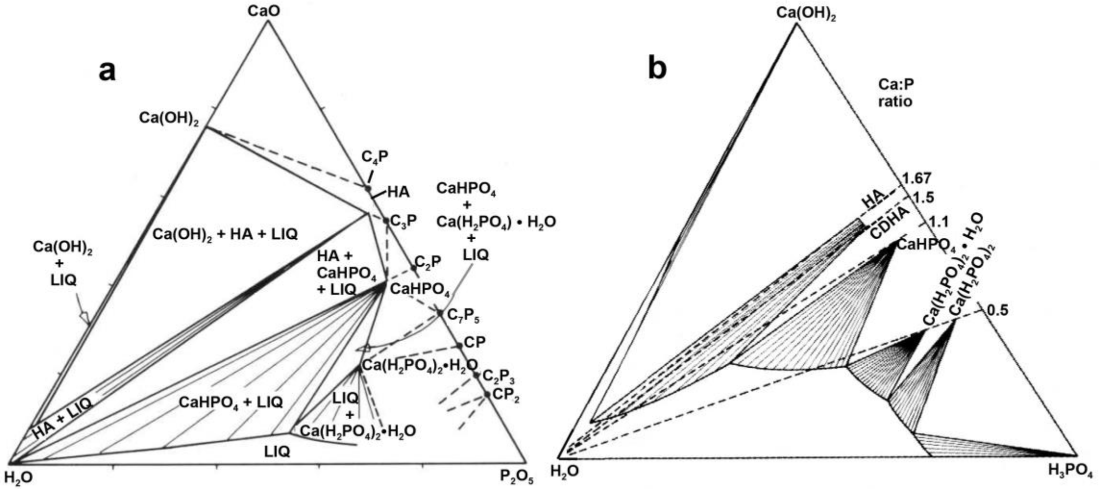

Fig I. 10: (a) The system $CaO-P_2O_5-H_2O$ at 200°C and 1700 kPa, (b) Schematic representation of the system $CaO-H_3PO_4-H_2O$ at 25°C [33].

II.2.1. Monocalcium Phosphate Monohydrate (MCPM)

Monocalcium phosphate monohydrate ($Ca(H_2PO_4)_2.H_2O$) is the acidic and most water-soluble calcium orthophosphate. Although they were known as "superphosphate of lime" by 1795[35], their differentiation began in the 1800s, at a Ca/P ratio of 0.5 and a solution pH below 2.0, MCPM crystallizes from aqueous solutions containing dissolved ions of H_2PO_4 and Ca^{2+}. Furthermore, MCPM could be precipitated from organic solvent-containing aqueous solutions.

MCPM releases a molecule of water and transforms into MCPA at temperatures above 100 C, but at temperatures ≳500 C, MCPA turns into $Ca(PO_3)_2$ [36, 37].

MCPM is never found in biological calcifications due to its high acidity and solubility. On the other side, pure MCPM is incompatible with bones. However, in medicine, MCPM is used as a component of several self-hardening calcium orthophosphate formulations.

MCPM is also used in dry baking powders, meals, feed, and some drinks as a nutrient, acidulant, and mineral supplement. Furthermore, MCPM could be used in ceramics and glasses, while agriculture is the primary consumer of technical grade MCPM, used as a triple superphosphate fertilizer [37, 38].

II.2.2. Dicalcium Phosphate Dihydrate (DCPD)

Since at least 1804, dicalcium phosphate dihydrate ($CaHPO_4.2H_2O$) has been identified [35]. Brushite was discovered as a mineral in phosphatic from Avis (Caribbean Island) in 1865 and was named to honor an American mineralogist [39].

DCPD can be easily crystallized from aqueous solutions containing dissolved ions of HPO_4^{2-} and Ca^{2+} at the Ca/P ratio ~1 and solution pH within ~2.0< pH <~6.5.

Because it is often detected in pathological calcifications (dental calculi, crystalluria, chondrocalcinosis), DCPD is of biological significance. It was suggested as a link in bone mineralization and enamel dissolution in acids (dental erosion).

DCPD is used in self-setting calcium orthophosphate formulations and as tooth remineralization intermediate in medicine. DCPD is a caries-fighting agent that is often used as a mild polishing agent in toothpaste. A flame retardant, glass production, and a calcium supplement in meals, feed, and cereals are among the other uses [37, 38].

II.2.3. Dicalcium Phosphate Anhydrous (DCPA)

The anhydrous form of DCPD is dicalcium phosphate anhydrous ($CaHPO_4$). However, DCPD has been known since at least 1804 [29]. DCPA was identified in 1879 as “mono hydrogen calcium orthophosphate, $HCaPO_4$.” Monetite was first discovered as a mineral in rock phosphate deposits on the Moneta (now Monito) Island (a Puerto Rican archipelago), where it is found in abundance [40]. DCPA is less soluble than DCPD due to the absence of water inclusions.

DCPA, like DCPD, can be crystallized from aqueous solutions with a Ca/P ratio ~1 when the solution pH is between 2.0 and 6.5, but at temperatures $\gtrsim$90°C. Even when dispersed in water for over seven months at temperatures ranging from 4 to 50 C, DCPA remained physically stable and resisted hydration.

DCPA might also be implanted as bioceramics. Other uses include polishing, as a calcium and phosphate source in dietary supplements (e.g., in prepared breakfast cereals, enriched flour), as a tableting aid, and as a component of toothpaste. It's also used in the food industry as a dough conditioner [37, 38].

II.2.4. Octacalcium Phosphate (OCP)

OCP has been known since 1843 when Percy published a paper [41], in which he described the formation of “a new hydrated phosphate of lime” with a chemical formula $2CaO + PO_5 + 6OH$. During the precipitation of the thermodynamically more stable calcium orthophosphates, octacalcium phosphate ($Ca_8(HPO_4)_2(PO_4)_4.5H_2O$) is often discovered as an unstable transient intermediate. Preparation techniques of OCP are available in the literature. Briefly, to prepare OCP, Ca^- and PO^{4-} containing chemicals must be mixed to get the supersaturated aqueous solutions with the Ca/P ratio equal to 1.33.

OCP is essential in biology because it is one of the stable components of the human dental system. Through subsequent precipitation and stepwise hydrolysis of OCP, W. E. Brown suggested that OCP participates as the initial phase in enamel mineral formation and bone formation[42]. In vivo, OCP is essential for the formation of apatitic biominerals. Although OCP has not been detected in vascular calcifications, it has been proposed that it is a precursor phase to biological apatite, found in natural and prosthetic heart valves[42].

II.2.5. Beta Tricalcium Phosphate (β-TCP)

One of the polymorphs of TCP is tricalcium phosphate (b-$Ca_3(PO_4)_2$). Although calcium orthophosphates with a composition similar to TCP, CDHA, and HA were discovered in the 1770s [29], α- and β- polymorphs of TCP were differentiated only by 1932[43]. It is impossible to precipitate β-TCP from aqueous solutions. It is a high-temperature phase that can be made by thermal decomposition of CDHA or solid-state interaction of acidic calcium orthophosphates, such as DCPA with a base such as CaO at temperatures above 800°C. The chemicals must be mixed in the proportions required to achieve a Ca/P ratio of 1.50 in all cases.

β-TCP is used in the self-setting calcium orthophosphate formulations and other types of bone graft medicine. β-TCP has been used in dentistry also and Some toothpaste brands, for example, include β-TCP as a gentle polishing agent [37, 38].

II.2.6. Alpha Tricalcium Phosphate (α-TCP)

α-Tricalcium phosphate (α-$Ca_3(PO_4)_2$) is a polymorph of TCP, which was differentiated by 1932[43]. Because α-TCP is a high-temperature phase, it cannot be precipitated from aqueous solutions. As a result, α -TCP is typically prepared using the same methods as β-TCP, with the exception that calcining is done at temperatures above 1200°C because the β -TCP converted to α -TCP transition temperature is 1125°C. However, there is data available that α-TCP can be made at lower temperatures. Precisely, the previously forgotten data that the presence of silicates stabilized α-TCP at temperatures of 800–1000 C was rediscovered at the turn of the millennium. Furthermore, by thermal decomposition of low-temperature ACP, α-TCP can be prepared at even lower temperatures (700°C) [44].

The reactivity of α-TCP was improved even more after milling. α-TCP is a component of self-setting calcium orthophosphate formulations in medicine. Alternatively, the chemically pure α-TCP has sparked little interest in the biomedical field. The disadvantage of using α-TCP is that it has a high resorption rate (faster than new bone formation), limiting its use in this area.

However, the silicon stabilized α-TCP (more accurately, as a biphasic composite with HAp) has been commercialized as a starting material for bioresorbable porous ceramic scaffolds as artificial bone grafts. α-TCP tends to convert to CDHA after implantation, which significantly reduces the rate of further degradation; α-TCP of a technical grade, like β-TCP, might be used as a slow-release fertilizer for acidic soils[36].

II.2.7. Hydroxyapatite (Hap)

The crystal unit cell of hydroxyapatite ($Ca_5(PO_4)_3(OH)$ is usually written as $Ca_{10}(PO_4)_6(OH)_2$ to indicate that it includes two molecules. Apatites were first identified as calcium phosphates in 1789 [29]. It's worth noting that hydroxyapatite is a more precise abbreviation expansion of HAp (perhaps hydroxydeapatite would be even better because it refers to calcium hydroxide). Whereas HAp is commonly expanded as hydroxyapatite by both the medical and material communities.

Chemically pure HAp crystallizes in the monoclinic space group P21/b. However, at temperatures above 250°C, there is a monoclinic to hexagonal phase transition in HAp (space group P63/m) [36, 37]. In 1964, the first detailed description of the HAp structure was published [45]. Since the publication of Posner and Betts' article[46], their interpretation in terms of aggregation of $Ca_9(PO_4)_6$ clusters, known as Posner's clusters, has been widely used.

Preparation of HAp can be done in various methods, including solid-state reactions and wet processes via precipitation, hydrothermal synthesis, and hydrolysis of other calcium orthophosphates. However, in all cases, substances containing Ca and PO_4 must be mixed to obtain a Ca/P ratio strictly equal to 1,67. An aqueous solution, on the other way, can be used to prepare well-crystalline HAp. It's possible to produce HAp with a Ca/P ratio of >1.67 (HAp rich in Ca). There is more information on HA synthesis elsewhere[47].

HAp is widely used as a coating on orthopedic (e.g., hip joint prosthesis) and dental implants because of its chemical similarities to bone and teeth mineral[48, 49]. HAp bioceramics are also very popular. Because of its strong similarity to biological apatite, HAp has been used in liquid chromatography of nucleic acids, proteins, and other biological compounds and for drug delivery purposes for a long time. Also, HAp is added to some toothpaste brands as a gentle polishing agent instead of calcium carbonate. Non-biomedical applications of HAp include its use as an environmentally friendly sorbent of toxic chemical elements and a carrier for various catalysts[37].

II.2.8. Fluorapatite (Fap)

Fluorapatite (FAp, $Ca_5(PO_4)_3F$) is usually expressed as $Ca_{10}(PO_4)_6F_2$ to indicate that the crystal unit cell contains two molecules. Since the presence of 2.5 % of fluorides in natural apatites was established by 1798 [50], this date might be accepted as the earliest hearing of FAp. Among all calcium orthophosphates, FAp is the hardest (5 on the Mohs scale of mineral hardness), the most stable, and the least soluble. Due to its properties, FAp is the only calcium orthophosphate that naturally forms large deposits suitable for commercial use [51].

Chemically pure FAp can be prepared in the same way as HAp. Furthermore, FAp is the only calcium orthophosphate that melts without decomposition (melting point: 1650°C); thus, single FAp crystals can be grown from FAp melts. Also, FAp was prepared with an excess of CaF_2. In 1930, the crystal structure of FAp was studied for the first time in1930 and is well described elsewhere [36]. FAp easily forms solid solutions with HAp with any desired F/OH molar ratio. Such compounds are called fluorhydroxyapatites (FHAp) or hydroxyfluorapatites (HFAp) and described with a chemical formula $Ca_{10}(PO_4)6(OH)_{2-x}F_x$, where $0 < x <2$. If the F/OH ratio is either uncertain or not necessary, the chemical formula of FHAp and HFAp is often written as $Ca10(PO4)_6(F, OH)_2$. Chemically pure FAp is not used for grafting purposes. Contrary to the initial expectations, this is most likely due to FAp's low solubility, chemical stability, and toxicity from high fluoride levels. Attempts to test FA-containing formulations, ion-substituted FAp, FHAp, and porous FAp bioceramics, on the other hand, continue to be successful. Catalysts are one of FAp's non-biomedical applications [37].

II.2.9. Oxyapatite (OAp)

The least stable and therefore least known calcium orthophosphate is oxyapatite (OAp, $Ca_{10}(PO_4)_6O$), which most probably does not exist. Nonetheless, in 1912, A.F. Rogers (1887–1957) proposed the word "voelckerite" to describe a hypothetical mineral with the chemical formula $3Ca_3(PO_4)_2 + CaO$ [42], in honor of an English agricultural chemist named John Christopher Augustus Voelcker (1822–1884) who, in 1883, first showed an apparent halogen deficiency in some natural apatites [43].

Pure OAp has never been prepared; therefore, its properties are not well established. Furthermore, there are still severe doubts that pure OA can exist. However, a mixture (or a solid solution) of OAp and HAp(oxy-HAp) might be prepared by a partial dehydroxylation of HAp at temperatures exceeding ~900°C (e.g., during plasma spray of HAp) only in the absence of water vapor [44]. It also might be crystallized in glass-ceramics. In aqueous conditions, OAp is extremely unstable and lacks a stability field. Specifically, data show that oxy-HAp containing less than 25% HAp (i.e., almost OAp) decomposes to a mixture of α-TCP and TTCP during further dehydration. Furthermore, when OAp comes into contact with water vapor, it transforms into HAp [44].

OAp cannot be found in biological systems due to the aforementioned issues with OAp preparation. Furthermore, there is no information about OAp's biomedical applications. The only exception appears to be plasma-sprayed calcium orthophosphate coatings containing OAp as an admixture phase [39].

II.2.10. Tetracalcium Phosphate (TTCP)

The most basic calcium orthophosphate is tetracalcium phosphate, also known as tetracalcium diorthophosphate monoxide ($Ca_4(PO_4)_2O$), which has a higher solubility in water than HAp. The mineral hilgenstockite was named after a German metallurgist Gustav Hilgenstock (1844–1913), who found it in Thomas slag from blast furnaces in 1883[52]. Its substantial industrial significance stems from the fact that reactions between orthophosphates and lime produce iron manufacture. TTCP plays a significant role in controlling the properties of the metal as a result of these reactions.

Aqueous solutions will not precipitate TTCP. It can only be prepared by solid-state reactions at temperatures above 1300°C, such as heating homogenized equimolar quantities of DCPA and $CaCO_3$ in dry air or a dry nitrogen flow [53]. To avoid the uptake of water and the formation of HA, these reactions should be carried out in a dry atmosphere, in a vacuum, or with fast cooling, and the Ca/P ratio must be equal to 2,00 in all cases. TTCP is therefore never detected in biological calcifications. TTCP is commonly used in medicine to make various self-setting calcium orthophosphate formulations; however, there is no commercially available pure TTCP-only bone substitute [53].

II.2. Characterization of calcium phosphates

We will concentrate on physicochemical analyses with X-ray diffraction (XRD) and Fourier transform infrared spectroscopy (FTIR) because our study is based on these two methods, which are the most widely used for physicochemical studies of calcium phosphates.

II.2.1. Diffractograms and reference spectra of calcium phosphates

XRD is an indispensable technique for the characterization of calcium phosphate materials. XRD tests have been carried out on single crystals, solid polycrystalline ceramics, coatings, or powders [54, 55]. The position of the peaks on the XRD patterns allows the identification of all crystalline calcium phosphate compounds as recorded in diffraction pattern databases such as those of the International Centre for Diffraction Data (ICDD), the Joint Committee for Powder Diffraction Standards (JCPDS), or others [3]. In ordinary use, some specific intense peaks (so-called 100% peak) are used to recognize the main Ca-P phases [3]. Table I. 9 summarises the 100% peaks, the orientation corresponding to these peaks, the inter-article distance (d_{hkl}), and the diffraction angle according to this crystallographic orientation (the X-ray used is the characteristic copper line λk1Cu).

Table I. 9: Main data from the X-ray spectra of calcium phosphates [56].

Phase	JCPDS File	hkl (100%)	dhkl(°A)	$(2\theta, \lambda_{Cu})$
α-TCP	09-0348	441	2.905	30.753
β-TCP	09-0169	210	2.88	31.027
TTCP	25-1137	040	2.995	29.807
HAP	72-1243	211	2.81	31.820
FAP	15-0876	211	2.80	31,937
DCPA Monetite	09-0080	112	2.958	30.189
DCPD Brushite	09-0077	020	7.57	11.681
	09-0077	121	4.24	20.935
OCP	26-1056	010	18.7	4.722

II.2.2. Fourier transform infrared (FT-IR) spectra of calcium phosphates

FT-IR spectroscopy allows the identification of most phases of calcium phosphate. In general, this method focuses on using the internal vibrational levels of molecules and ions, which can vary according to these molecules or ions' close-range environments. Phosphate, carbonate, hydroxide, and water molecules are detected by FT-IR spectroscopy [57].

Phases that XRD cannot easily distinguish can be discriminated by using FT-IR spectroscopy. In this case, for example, for OCP and apatite. Amorphous calcium phosphate phases are sometimes not detectable by XRD, and therefore the FT-IR technique allows us to confirm their existence [57]. Table I. 10 summarises the main characteristic bands of phosphate groups' different vibrational modes in infrared spectroscopy.

Table I. 10: Vibrational modes characteristic of phosphate (PO_4^{3-}) and acid (HPO_4^{2-}) groups in calcium phosphate networks (cm^{-1}) [58, 59].

Phase Vibration mode	α-TCP	β-TCP	TTCP	HAp	FAp	DCPA	DCPD	OCP	ATCP
							1400		
							1350		
						1215		1295	
							1175	1193	
						1132	1128	1137	

υ_3 (PO_4^{3-})								1121	
		1119			1160			1103	
			1105						
		1094	1093	1092		1070		1077	
		1080	1073			1060	1064	1055	
	1055		1062						1040
	1039	1041	1046	1040	1038			1037	
	1025		1033					1023	
	1013					1000		1000	
	997	1010	1010						
	984								
υ_1 (PO_4^{3-})		972	989			992	984		
			962	962	968			962	
	954		956						
		945	946						949
			941						
υ_4 (PO_4^{3-})	613		620					627	
	597	602	594	601	604			601	
	585	589							
	563		571	575	571	577	576	575	
	551	550		561	566		563	560	560
		541	501			526	525	524	
υ_2 (PO_4^{3-})	471		471	472	471	480			
	463							466	
	454								
	430	432	450			428	418	449	
	415		429			405	400		
			399			398			
P-OH (HPO_4^{2-})								917	
						892	892	861	
OH^-				632					
				3570					

Part III. Fluorapatite

Fluorapatite (FAp, $Ca_{10}(PO_4)_6F_2$), Hydroxyapatite (HAp, $Ca_{10}(PO_4)_6(OH)_2$), chlorapatite (ClAp, $Ca_{10}(PO_4)_6C_{l2}$), and carbonated apatites are the principal components of the apatite family. Because several natural minerals containing FAp exist, they are used in a wide range of applications. Calcium apatites are also important in biology because they are part of the mineralization process and form the mineral part of bone and teeth. FAps are biocompatible materials that are used to replace and coat bone prostheses. In particular, FAp has recently attracted considerable attention because the presence of fluoride enhances biodegradability and compressive strength and stimulates the formation of bone tissues. Bogdanov et al[60]. Fluoride-containing coatings have also been shown to do an effect on bone cells. When compared to pure hydroxyapatite, the addition of fluoride to apatite has been shown to improve osteoblast response in terms of adhesion, differentiation [61], proliferation [62], and mineralization processes [63]. Several applications bolster the scientific interest in this compound.

III.1. Structure of fluoroapatite

Fluoroapatite of formula $Ca_{10}(PO_4)_6F_2$ crystallizes in the hexagonal system of space group P63/m[64]. Its structure was described by Naraz[65] and later by Beevers [66], and then by Young et al. [67] as a honeycomb assembly of PO_4 ions (Fig I. 11). The phosphocalcic fluorapatite $Ca_{10}(PO_4)_6F_2$, which is the most abundant component in nature, has mesh parameters:
a = 0.9372 nm and c = 0.6885 nm [68]. Its structure can be described by columns of calcium atoms arranged at the vertices and middles of the hexagonal mesh edges (Fig I. 11). The atoms of Ca occupy two different sites [69, 70]:

1. $Ca(I)O_9$ polyhedra in sevenfold coordination.
2. $Ca(II)O_5Z(O)$ polyhedra in ninefold coordination.

The quasi-compact arrangement of the anionic groups (PO^{3-}) forms the skeleton of this structure and reveals two types of tunnels.

The first tunnel, which coincides with the lattice's ternary axis, is occupied by Ca^{2+} cations spaced c/2 apart along the oz axis. These Ca^{2+} ions are denoted Ca (I) (Fig I.12, a).

The second tunnel has a larger diameter. Its axis, a helical axis, is occupied by fluoride ions while its walls contain the remaining Ca2+ ions, denoted by Ca (II). These cations are located on equilateral triangles offset from each other by an angle of 60° (Fig I.12, b). The presence of these tunnels is at the origin of the numerous substitution reactions observed in this family.

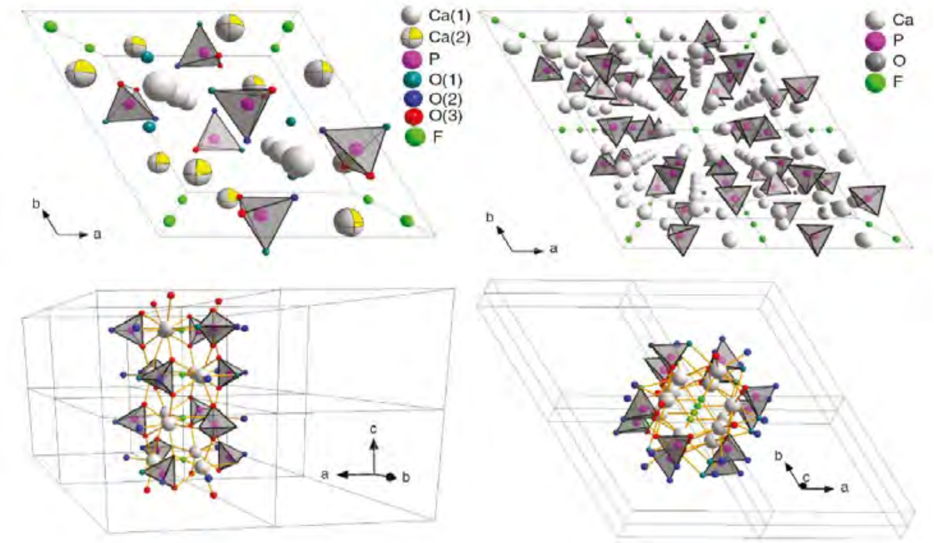

Fig I. 11: Projection of the structure of fluorapatite (Fap) [62-65].

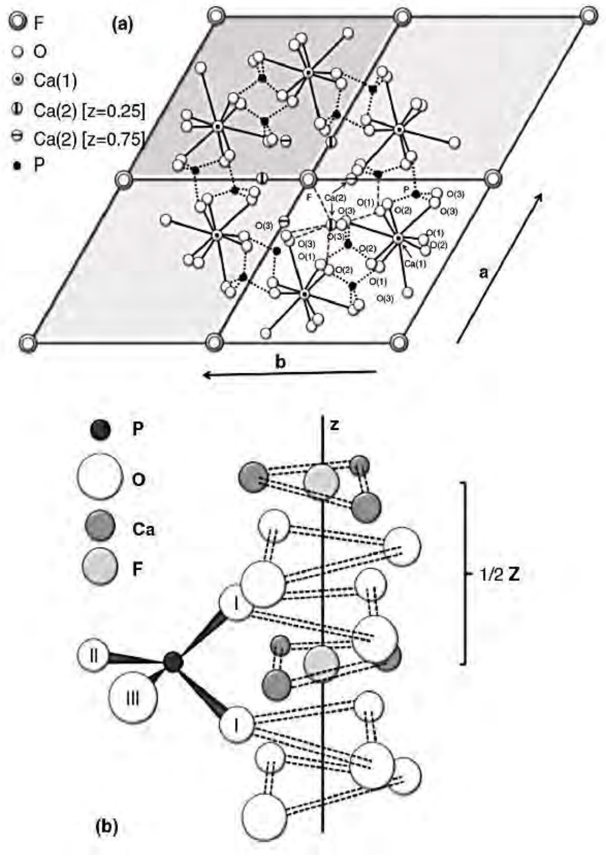

Fig I. 12: Schematic representation Elementary mesh of part of four unit cells of the fluorapatite structure projected on the plan (0001) [67, 68].

III.2. Properties of fluorapatite

Fluorapatite has been exploited in the biomedical field in recent years because of its high thermal and chemical stability.

- **Physicochemical properties**

FAp contains 39.68% calcium by mass, 18.45% phosphorus and 3.77% fluorine. The Ca/P atomic ratio is 1,67. The diffraction lines of pure FAp are shown in (Fig I.13, JCPDS 15-0876), Infrared (FT-IR), and Raman spectrum of FAp is shown in Fig I.14 (a) and (b), respectively. The most expressive infrared bands are attributed to fundamental frequencies of tetrahedral phosphate ion $(PO_4)^{3-}$. The structure of apatite leads to the reduction of ion symmetry (four fundamental frequencies with IR inactive ν_1 mode), where ν_1 mode becomes IR active [71, 72]:

1. The $\nu_1(PO_4)$ mode is a very weak (vw) band related to the symmetric stretching of phosphate ions.
2. Bending: ν_2 mode (vw)
3. Anti-symmetric stretching: ν_3 mode is the strongest (vs, vb) band in the infrared spectrum appearing in the spectral region from 1000 to 1150 cm^{-1}.
4. Bending: ν_4 mode (m, vb) is observed between 540 and 620 cm^{-1}.

(the spectrum: very weak (vw), weak (w), middle (m), strong (s), very strong (vs), shoulder (sh), broad (b), very broad (vb) and sharp (sp)).

The crystallinity of natural and synthetic apatite samples is often determined from the broadening of $\nu_4(PO_4)$ infrared absorption bands [73]. The presence of calcite causes the anti-symmetric stretching mode (ν_3) of planar CO_3^{2-} ion to appear in the investigated sample's infrared spectrum.

Fluoride is indeed known as an acid attack resistant agent. It has been used for many years in the biomedical field to treat osteoporosis or increase resistance to tooth enamel resistance [74, 75]. In contrast, human bone contains only 1% by mass of fluorine [76]. Excess fluoride can produce growth disorders and lead to disease, fluorosis.

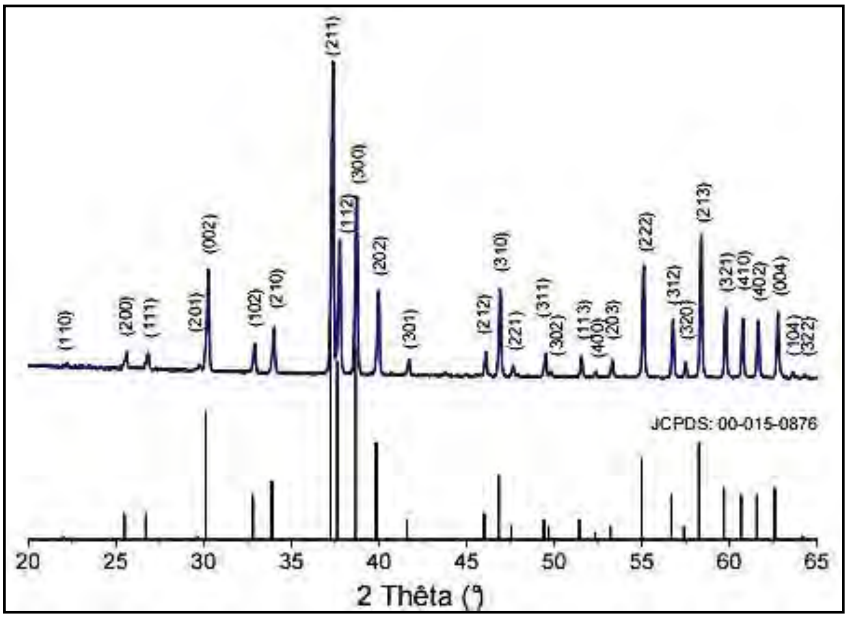

Fig I.13: X-ray diffraction spectrum of stoichiometric Fap powder [JCPDS 15-0876].

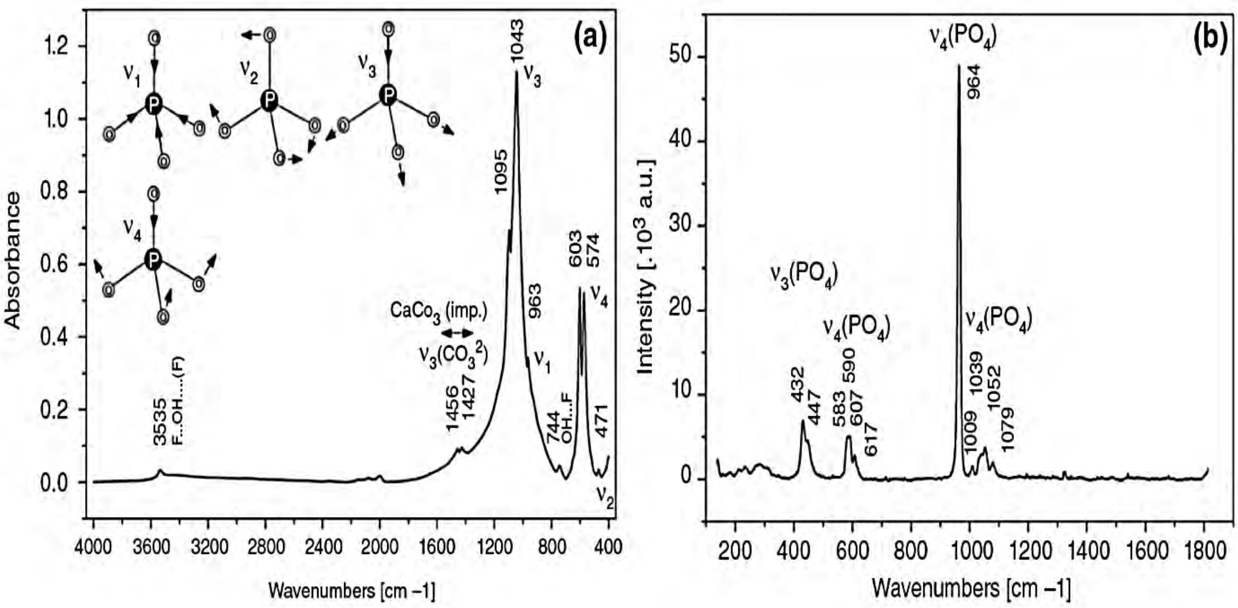

Fig I.14: Infrared (a) and Raman (b) spectrum of fluorapatite [69, 70].

- **Thermal properties**

Fluoroapatite is thermally relatively stable. Its melting temperature is 1644°C. Decomposition of fluorapatite occurs at a temperature above 1600°C, according to the following reaction [64]:

$$3\ Ca_{10}(PO_4)_6F_2(s) \longrightarrow 2POF_3\ (g) + 2Ca_3(PO_4)_2\ (s) + 6Ca_4(PO_4)_2(s) \qquad (1)$$

However, the behavior of fluorapatite at high temperatures depends on several factors: the synthesis method, the nature of the starting reagents, the Ca/P ratio of the product obtained, the presence of impurities such as CO_3^{2-} and HPO_4^{2-} ions.

Its Physico-chemical and mechanical properties are illustrated in table I.11.

Table I. 11: Physicochemical and mechanical properties of FAp.

Chemical formula	$Ca_{10}(PO_4)_6F_2$	Reference
Structure	Hexagonale, $P6_3/m$	[77]
Density	3,19	[78]
Solubility product	pks=60	[79]
Enthalpy of formation	-35,59kJ/mol	[80]
Melting point	1640°C	[64]
Dielectric constant	9,5-10,4 pFm^{-1}	[81]
Thermal conductivity	0,02W/Cm.K	[68]
Zeta potential	6,5-8,8	[77]
Young's module	94 GPa	[77]

III.3. Fluorapatite Synthesis Methods

Different methods can synthesize fluorapatite powder.

Aqueous synthesis

The principle consists of dissolving stoichiometric calcined hydroxyapatite with a stoichiometric quantity of fluoride ions. A superficial ionic exchange is established between fluoride and hydroxyl ions with the Hap's dissolution and fluorapatite precipitation. However, fluoride ions promote stoichiometric apatite formation on the surface and stop the surface hydrolysis of PO_4^{3-} ions. The fluorination in an aqueous medium is strongly dependent on the concentration of fluoride F^- ions [82].

This method does not produce pure and stoichiometric fluorapatite at the same time. However, it is less soluble and more resistant to acid attack than hydroxyapatite. This stability is linked to hydrogen bonds between the fluoride and hydroxide ions which stabilize the network [83].

Dry synthesis: two methods are known

- The first uses a mixture of tricalcium orthophosphate and calcium fluoride [84, 85]. The reaction is generally carried out at 900°C under dry gas (argon or helium) to avoid any hydrolysis of fluoride ions during heating. With an excess of 5% CaF_2 to facilitate the reaction. However, the fluorapatite thus obtained is non-stoichiometric and deficient in calcium [85].

$$3Ca_3(PO_4)_2 + CaF_2 \longrightarrow Ca_{10}(PO_4)_6F_2 \qquad (2)$$

At the temperature of 900°C, hydroxylapatite reacts with calcium fluoride to give fluorapatite [30]:

$$Ca_{10}(PO_4)_6(OH)_2 + CaF_2 \longrightarrow Ca_{10}(PO_4)_6F_2 + CaO + H_2O\ (g) \qquad (3)$$

FAp can also be prepared directly by firing a mix of $Ca_3(PO_4)_2$ with CaF_2 at 1600°C, or from calcium pyrophosphate and calcium fluoride:

$$18Ca_2P_2O_7 + 14CaF_2 \longrightarrow 5Ca_{10}(PO_4)_6F_2 + 6POF \qquad (4)$$

Initial phase diagram Fig I.15 (a) for the section $Ca_3(PO_4)_2$-CaF_2 [86] of the ternary system CaO-P_2O_5-CaF_2 was published by NACKEN [87]. The range of compositions was extended by BERAK [88] Fig I.15 (b) and further refined (Fig I.16) by BERAK and HUDINA [87]. Important features are congruent melting of FAp at 1650°C, eutectics with $Ca_3(PO_4)_2$ at 1620°C, and a second one with CaF_2 at 1203°C.

- The second method is high-temperature gas fluorination [82] of the hydroxyapatite according to the following equation (8):

$$Ca_{10}(PO_4)_6(OH)_2 + 2NH_4F \rightarrow Ca_{10}(PO_4)_6F_2 + 2NH_3 + 2H_2O \qquad (5)$$

The principle of this synthesis consists of putting the hydroxyapatite powder in a tubular furnace whose tube is swept by a flow of inert gas. Ammonium fluoride is placed upstream of the pod containing the HAp at a temperature of approximately 165°C to obtain slow sublimation. From 500°C onwards, ionic diffusion of fluorine into the apatite lattice is observed.

The level of fluorine introduced into the apatite increases with temperature and ionic mobility in the lattice. However, Hap also decomposes by reacting with gas, which leads to the formation of impurities (calcium fluoride and amorphous fluorinated phosphate). The fluoridation rate is difficult to control [82], and the cost is relatively high. This method is therefore not used industrially.

Thus, despite scientific studies showing the good mechanical properties, stability, and good behavior in biological media of fluorine-containing apatites, their biomedical applications in orthopedics have not yet reached the stage of industrial exploitation.

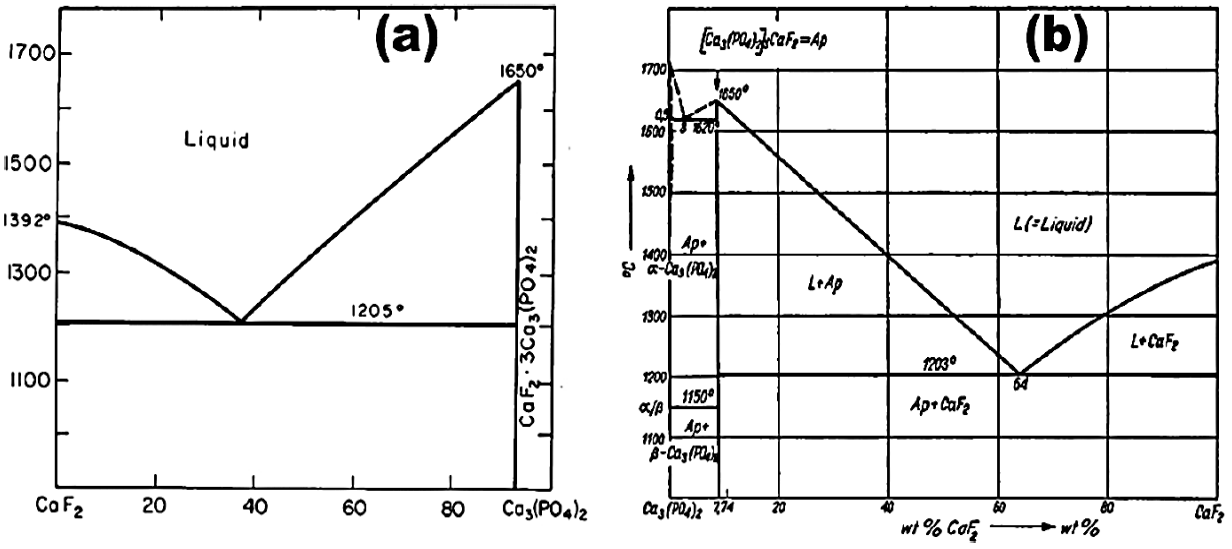

Fig I.15: Phase diagram of $Ca_3(PO_4)_2$–CaF_2 section [84].

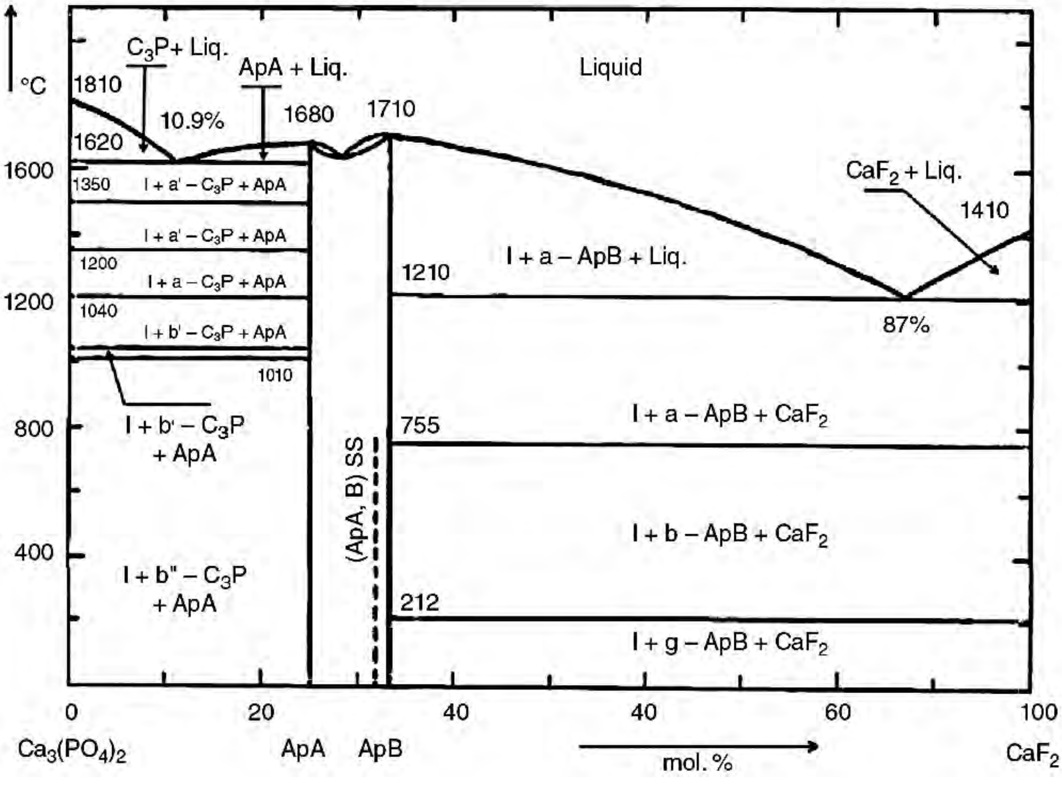

Fig I.16: Phase equilibrium in the system $Ca_3(PO_4)_2$-CaF_2: FAp (ApA) and $Ca_7(PO_4)_4F_2$ (ApB) [85].

Part IV. Quartz (SiO_2), Alumina (Al_2O_3), and their composites

IV.1. The quartz and its characteristics

Anhydrous silica occurs in three crystallized forms: quartz, tridymite, cristobalite, and a non-crystallized form, silica glass. Quartz is one of the most abundant of these species throughout the earth's crust. Quartz is found in igneous rocks (granites, granulites) and in sedimentary rocks (sands, sandstones, quartzite), from which it can be extracted in its pure state by acid washing. Quartz is a polymorph of crystalline silicon dioxide (SiO_2) that exists at ambient pressure. It can be found in nature as single crystals of various sizes and can also be produced synthetically as large crystals. The phase diagram of this quartz type is shown in Fig. I.17 to discuss the high temperature and pressure behavior of quartz.

Quartz crystallizes in its standard α-quartz structure at temperatures below 573°C. However, a reversible phase change to β-quartz occurs at temperatures above 573°C. α-quartz has a trigonal crystalline structure and a density of 2.65 g/cm^3. The SiO_4 tetrahedra in β-quartz have a slight twist, allowing the crystal to have hexagonal symmetry. The density is reduced as a result of the phase transformation to 2.53 g/cm^3. However, it does not break up any chemical bonds, and the tetrahedra display no distortion[89].

Synthetic quartz undergoes another phase transformation at 1050°C, transforming into -Cristobalite. Furthermore, at temperatures above 1705°C, quartz begins to melt (all temperatures are stated for 1 bar).

The composition of natural quartz is very similar to that of synthetic quartz. Synthetic quartz is most commonly grown from a smaller seed crystal under high temperature and heat in an autoclave, whereas natural quartz grows over long timescales.

Furthermore, natural quartz usually contains more impurities, resulting in a wider variety of thermodynamic phases, such as tridymite [90, 91].

IV.2. Applications of quartz

Quartz has a significant economic value. Amethyst, citrine, smoky quartz, and rose quartz are only a few examples of gemstones. Sandstone is a common building stone that is primarily composed of quartz. Quartz sand (also known as silica sand) is widely used in glass and ceramics production and foundry molds in metal casting. Sandpaper contains crushed quartz as an abrasive, silica sand is used in sandblasting, and whole sandstone is also used to produce whetstones, millstones, and grindstones. In optics, silica glass (also known as fused quartz) is used to transmit ultraviolet light.

Tubing and various vessels of fused quartz have critical laboratory applications, and quartz fibers are employed in susceptible weighing devices. Fused quartz tubing and vessels are used in a range of laboratory applications, and quartz fibers are used in ultra-sensitive weighing instruments.

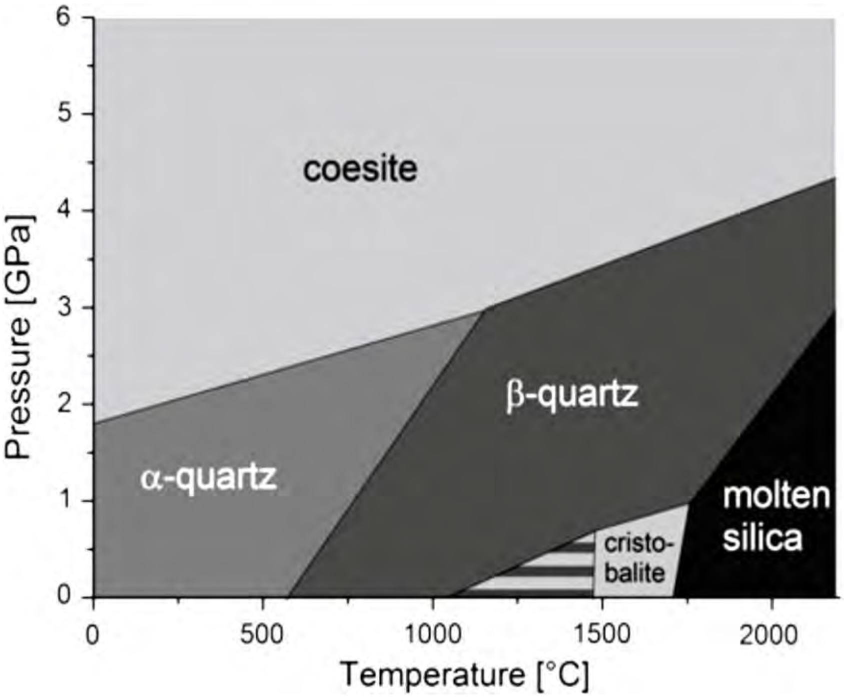

Fig I.17: Phase diagram of synthetic quartz / SiO_2[88, 89].

IV.3. Alumina (Al_2O_3)

Alumina is well known to ceramists for its inert and robust character. Dedicated to orthopedic use, it has proven biocompatibility, excellent mechanical properties, and great stability. Currently, alumina seems to be the most suitable material for orthopedic prostheses. Passuti et al. show that alumina-alumina pairs provide an excellent coefficient of friction and that the released particles do not lead to osteolysis [27]. Other studies have shown that alumina is the best material to reinforce calcium phosphates[92].

IV.3.1. Properties of alumina

Alumina is widely used in industry because it has good mechanical and electrical insulating properties and is characterized by its high melting point. It is a stable and chemically inert material. It is a stable and chemically inert material that can be obtained with very high purity

(> 99.5%) and a high density (>3.94). Its wettability is higher than that of metals and polymers (angle a=44°) and offers optimal joint lubrication. The main properties of alumina are shown in the table. I.12 [93]. When not used as a solid part, alumina is used in the biomedical field in the form of a deposit, most often produced using thermal spraying processes.

Table I.12: Mechanical, chemical, and thermal properties of alumina[93].

Properties	code	value
Volumetric mass (g /cm^3)	ρ	3,9
Molecular Weight (g / mole)	M	102
Young's modulus (GPa)	E	300 - 400
Poisson ratio	ν	0.25
Flexural strength (MPa)	σ_f	380
Dichotomy (Mpa.m$^{1/2}$)	K_{1C}	2-3
Dielectric constant	ε_r	9-10
Electrical resistance at 20°C (Ohm.cm)	σ	$>10^{14}$
Dielectric resistance (kV / mm)	-	10-20
Specific heat (J / K / kg)	C_p	900
Thermal conductivity (W / m / K) at 500 ° C	λ	10 - 15
Linear expansion (6 × 10) from 20 to 1000 ° C	α	8 - 9

IV.3.2. Application fields

The desirable mechanical and physico-chemical properties of alumina are exploited in a wide range of applications, namely

- Medicine: alumina is used in total hip prostheses in a dense polycrystalline form obtained from aluminum oxide powder compressed at very high temperature (1600°C).
- Chemical: Dense alumina films are used as a barrier to the chemical environment for metal substrates [94] and can also be used as a diffusion barrier [95];

- Mechanical: a cutting tool coated with an alumina film can increase its service life by ten times [96]; - Electronics: the use of alumina as an insulating layer allows the creation of MISFET-type devices [97, 98];

- Thermal: to protect the substrate from heat [99];

It should be noted that the manufacture of "surgical grade" alumina requires high technology and strict quality controls.

IV.4. Calcium silicate-based composites

Silicon (Si) is an essential trace element in the human body, where silicate-based materials have shown amazing potential in bone-related tissue engineering and tissue regeneration applications. Because of their improved and adjustable mechanical and biological properties, silicate-based bioactive composites with proper composition and structure promise bone regeneration materials. The primary benefit of silicate-based bioceramics is that silicon (Si) is needed for the mineralization and gene activation process [100].

Hench et al. discovered in the late 1960s that certain silicate-based glasses could activate the formation of HAp, the main mineral that composes bone [101]. Silicate-based bioactive ceramics can be classified into three types: silica-based bioactive glasses, such as Bioglass®; crystalline silicate-based ceramics, such as wollastonite (β-$CaSiO_3$), pseudowollastonite (α-$CaSiO_3$), diopside ($CaMgSi_2O_6$) [102]; and silicate-based glass–ceramics, which were first introduced as bone implant materials by Kokubo et al. in 1982 [103]. However, silicate-based inorganic biomaterials, like their phosphate-based counterparts, have high brittleness, low mechanical strength as significant drawbacks.

Preparing composite materials with other materials such as other types of ceramics, polymers, and metals to combine the advantages of two different kinds of materials is one technique for solving the problem of poor mechanical properties of certain ceramic materials. The nature of composite materials thus provides a unique opportunity to perfect material properties. Chemical composition is widely believed to be one of the most significant factors influencing material properties. Previous studies have shown that glass-ceramic containing CaO and SiO_2 possessed good bioactivity, and the CaO-SiO_2 system fig. I.18 [104] (like calcium silicate, CS) has been considered as the basis for the development of the third-generation tissue regeneration materials presently in development [105]. Besides that, some formulations of silicate-based bioceramics demonstrate excellent biodegradability. As a result, the production of calcium phosphate–silicate and bioinert ceramic/silicate composite ceramics could pave the way for new bioceramics with increased bioactivity and biodegradability.

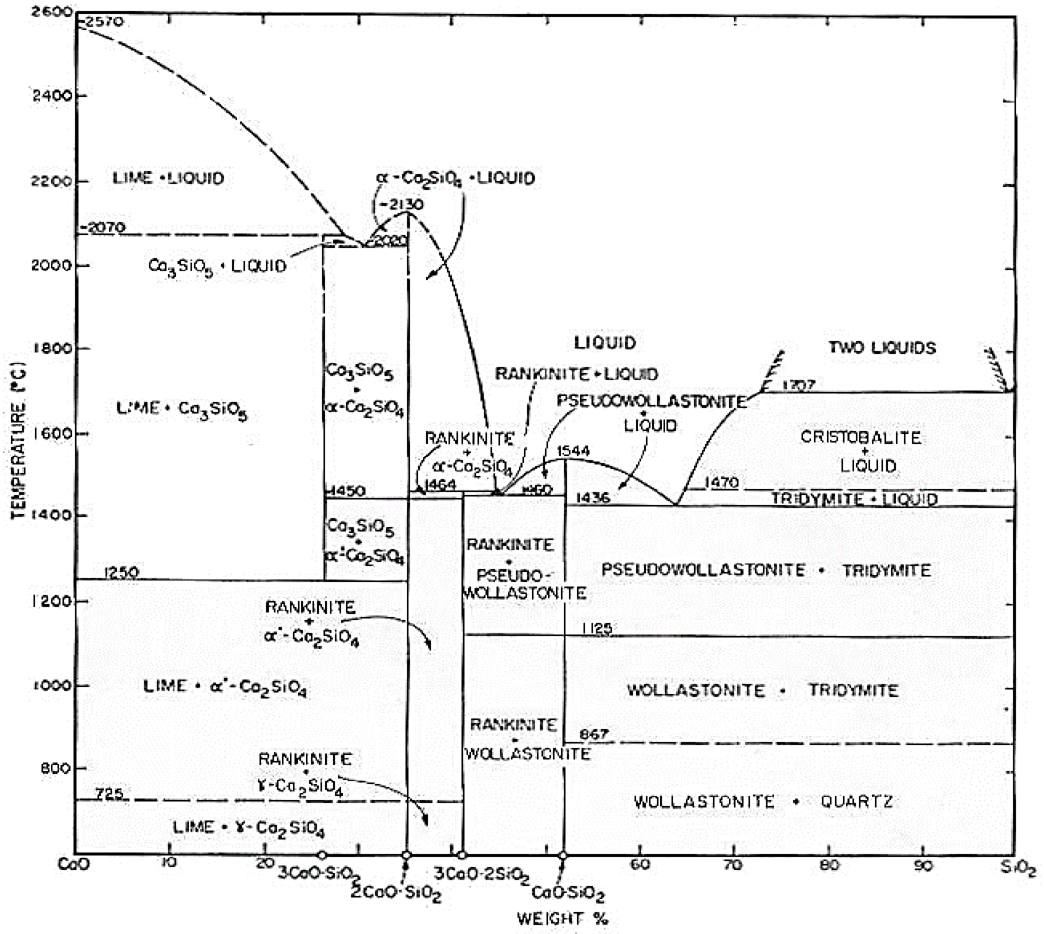

Fig I.18: Binary phase system CaO-SiO2 [102].

IV.4.1. Composite Ceramics of Calcium Silicate and Al_2O_3/ZrO_2

While silicate-based bioceramics have good bioactivity, their lack of mechanical properties prevents them from being used in clinical settings, particularly where high mechanical strength is needed.

Because of their high mechanical properties, alumina (Al_2O_3) and zirconia (ZrO_2) have been commonly used in prosthodontics and orthopaedics, making them perfect toughening fillers when it comes to enhancing the mechanical strength of silicate-based bioceramics. A mechanochemically fabricated uniform Al_2O_3 and -calcium silicate (α-$CaSiO_3$) composite ceramic was sintered at 1250°C to develop composite ceramics with open porosity, high hardness, and fracture toughness. The improvement of composite ceramics' mechanical properties was primarily attributed to a newly formed phase $CaAl_2O_4$ formed by CS and alumina's reaction (show Fig I.19) [106]. Another bioinert ceramic that can be used to strengthen silicate-based bioceramics is zirconia (ZrO_2), where the spark plasma sintering (SPS) technique was used to make $CaSiO_3/ZrO_2$ nanocomposites. The addition of ZrO_2 to CS could slow down the phase transition and boost the phase transition temperature. The fracture durability of the nanocomposites was significantly improved by the development of a nanocrystalline ZrO_2 network structure. The composites' in vitro bioactivity was fine, with the HAp layer forming on the nanocomposites' surface in SBF [107].

On another side, among the critical components of Portland cement, $Ca_3Al_2O_6$ has the highest hydration rate. The restricted presence of C_3A in C_3S, C_2S, or C_3S/C_2S (CSC) cements thought to speed up the hydration process and increase the short-term compressive strength of the materials, even though it is not appropriate as a single-phase bone cement due to its disputed cytocompatibility.

Biphasic mixtures can be formed using C_3S/C_3A and C_2S/C_3A composite systems. According to studies, the addition of C3A to C3S and C2S reduced the setting time and improved the substrates' compressive strength. Furthermore, when the content of C_3A is less than 10%, both mixtures are bioactive and biocompatible and have a stimulatory effect on L929 cell growth [108, 109]. Further research found that the CSC/C_3A cement was significantly more compatible with human dental pulp cells than Dycal® 'a commercially available cement' [110], because of their relatively short setting time, high compressive strength, better in vitro bioactivity, and biocompatibility, silicate-based cement mixed with a small amount of C_3A tend to be a promising candidate as dental cement. Fig I.19 and Fig I.20 show the binary phases of the $CaO-Al_2O_3$ system [111] and the diagram of the ternary system $CaO-Al_2O_3-SiO_2$ [112], respectively.

In recent years, many studies have demonstrated that combining silicates with other materials is an effective way to design bioactive biomaterials with improved properties for tissue regeneration, particularly as orthopaedic and dental implants or for bone tissue engineering applications.

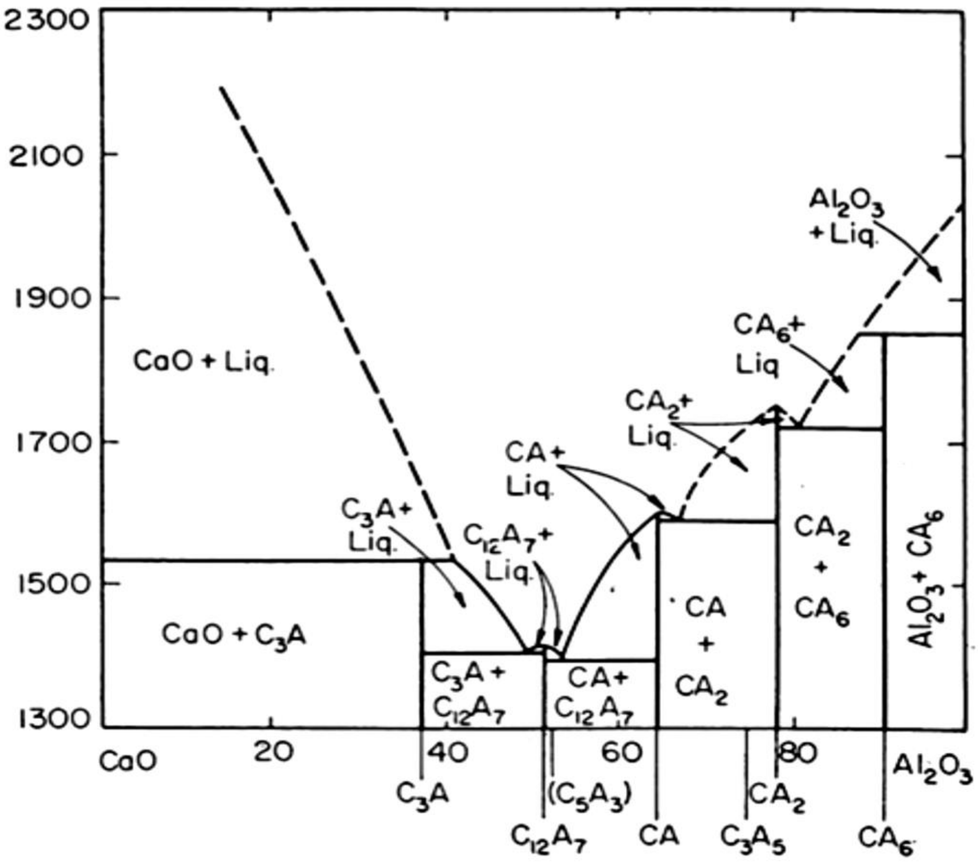

Fig I.19: Binary phase system CaO-Al2O3 [109].

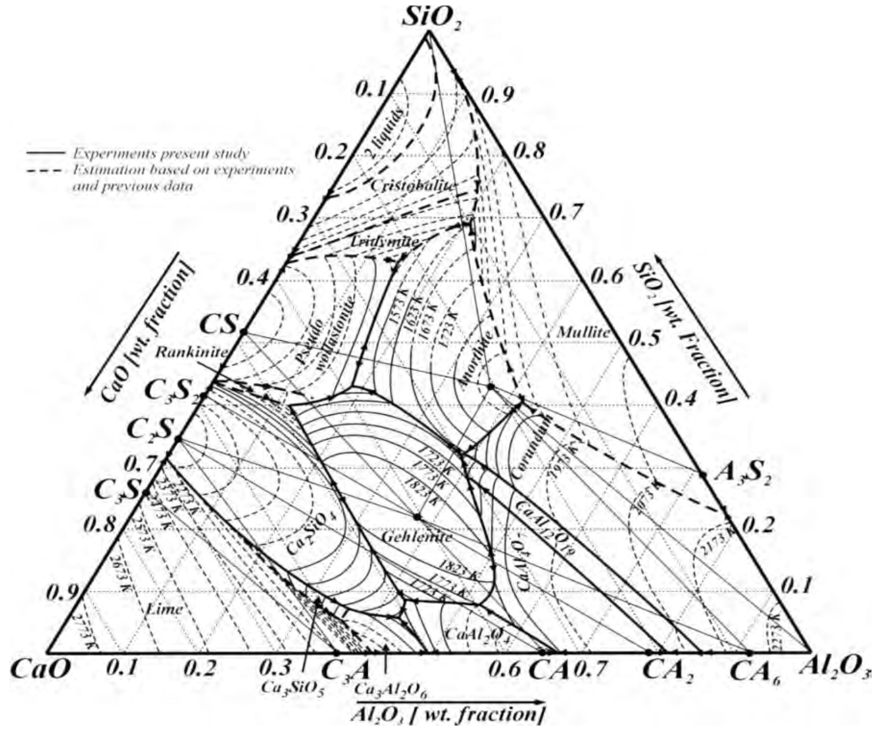

Fig I.20: Phase diagram of the ternary Al_2O_3-CaO-SiO2 system [109].

V. Recent research tendencies

Numerous studies have demonstrated that silica-containing bioceramics have excellent bioactivity and enhanced mechanical properties, thereby discovering their potential in biomedical applications [113-115]. Fuh et al. [113] prepared micro-porous Si-substituted HAp by immersing hydroxyapatite compact disc in tetraethoxysilane (TEOS) followed by hydrolysis and condensation reaction to allow silicon gel formation before sintering. The authors found that the TEOS-treated HA possessed higher biaxial flexural strength and excellent cytocompatibility when compared to pure HAp, having the same porosity level. Lin et al.[114] studied the effect of strontium (Sr) and silicon (Si) in $Sr_5(PO_4)_2SiO_4$ bioceramics on the in vitro cytocompatibility and osteogenic property for inducing osteogenesis. Their results indicated that Sr and Si ions' simultaneous release from the bioceramics played a significant role in improving the proliferation and osteogenic differentiation compared with pure β-TCP. Khan et al. [115] affirmed the benefits of Si-substituted bioceramics and agreed that Si inclusion improved the biological performance of calcium phosphate-based bioceramics. However, the authors inferred that the actual mechanism by which Si improves the bioceramics' osteoconductivity remains unclear and requires further investigation.

In another study, incorporating a 50% wollastonite ($CaSiO_3$) phase in the HAp matrix successfully improved the sintered body's compressive strength by more than 50%, accompanied by a higher degradation rate and excellent bioactivity compared with conventional HAp scaffold [116]. Spiro et al. [117] demonstrated that 20 wt% of dicalcium silicate (Ca_2SiO_4) effectively aids the densification of HAp. They found that the composite achieved 95% of theoretical density and flexural strength of 70.4 MPa when subjected to hot pressing at 1500°C, whereas the flexural strength of monolithic HAp only attained 45 MPa [117]. A kaolin-FAp composite was prepared in a recent study, where the main compositions in kaolin are silica and alumina. The density and hardness of the composites increased with an increase in kaolin content. It was shown that the sample with the addition of 57 wt% kaolin achieved a relative density of 97% and the highest hardness of approximately 6.5 GPa when sintered at 1325°C [118].

Borkowski et al. [119] studied the physicochemical and biological properties of FAp synthesized using the sol-gel method and sintered at various temperatures. It was found that FAp sintered at 800°C exhibited optimal porosity and fluoride release capacity, thus enhancing osteogenic cells' proliferation compared to the control group. Golafshan et al. [120] prepared strontium-fluorapatite (Sr-FAp), magnesium, and silicon-doped fluorapatite (Mg-SiFAp) by a mechanochemical method. They found that the dopants effectively promoted in vitro cellular proliferation and enhanced bone formation compared to the undoped FAp. Other dopants such as alumina (Al_2O_3) were also effective in promoting the sintering of FAp. Djouallah et al. [121] investigated the reaction-sintering between fluorapatite and Al_2O_3 using natural phosphate and boehmite by the mechanical mixing process. The sintering was performed in an air atmosphere at various temperatures (1000-1500°C). The results revealed that the densification and micro-hardness of FAp improved with increasing Al_2O_3 content and sintering temperature. It was found that the 25% Al_2O_3-doped FAp exhibited the highest density (2.95 g/cm^3) and hardness (6.5 ± 0.25 GPa) when sintered at 1450°C. The authors also noted that the physical and mechanical properties of the FAp were influenced by the phases formed, which were dependent on the alumina content and sintering conditions. Similar improvements in the mechanical properties were also reported by Youness et al. [122] for alumina-based carbonated fluorapatite.

In the present work, silicate-doped FAp composites were prepared for the first time by mixing natural FAp and quartz. This work aimed to investigate the effects of quartz addition up to 20 wt% on the phases and densification behavior of FAp when subjected to pressureless sintering.

In the second part of the current work, the alumina-fluorapatite-based composites were prepared from natural phosphate and pure alumina. Thus, this study investigates the effect of titania addition up to 10 wt% on the Physico-chemical proprieties of the composite.

Fluorapatite ($Ca_{10}(PO_4)_6F_2$) gained substantial attention recently .It is considered the most stable compound in the apatite family, as it is known for its pure presence practically in its natural state. Besides, FAp is a suitable host for many alternatives that can modify its physical, chemical, and biological properties as it stimulates the formation of bone tissue and increases compressive strength [60]. Besides, the advantages that FAp provides over HAp, such as thermal and chemical stability and a reduction in metals' solubility, are well known [123, 124]. Over and above these benefits, fluorine is well known to slow caries formation when incorporated into tooth enamel [123]. The fluoride ions themselves improve the morphology, proliferation, and differentiation of osteoblast cells directly in the cell attachment [125-127]. Even though the Fap, however, has low fracture toughness and resistance to wear, which restricts its use in biomedical applications [128].

Several necessary studies have devoted their efforts to enhance mechanical reliability by mixing the FAp with various bioceramics such as alumina and zirconia [129-130]. It was reported that the addition of 25% alumina (Al_2O_3) produced from boehmite transitions to the fluorapatite matrix effectively enhanced the hardness of the FAp (6.5 ± 0.25 GPa) accompanied by a higher density rate (2.95 g/cm^3) at 1400°C [121]. Much research has been interested in enhancing alumina-fluorapatite composite's mechanical reliability by including several additives[132]. For instance, Guidara et al. [126] investigated the mechanical properties of alumina-fluorapatite composite with various titania (TiO_2) content varies from (0 to 5wt%) sintered between 1200 to 1600°C. With the addition of 1.4wt% TiO2, the authors reported that the ceramic composite Al_2O_3–FAp was achieved successfully at 1500°C. The rupture resistance for alumina-fluorapatite samples containing 1.4wt% TiO2 when sintered at 1500°C reached ~75MPa corresponds to the lowest apparent porosity of 8%. As a result of this study, titania is a promising material for the reinforcement of alumina. At high sintering temperatures, titania can be dissolved in alumina to facilitate sintering. However, due to the new Al_2TiO_5 phase formatted at the grain boundary, TiO_2 may disproportionately inhibit alumina densification [132].

References

1. B.D. Ratner, AS. Hoffman, FJ. Schoen, JE. Lemons , Biomaterials science: an introduction to materials in medicine. 2004: Elsevier.
2. R. Borsa, Elaboration de poudres et de dépôts de phosphates de calcium silicatés à usage de biomatériaux, thèse de doctorat, Université de toulouse, france, 2008.
3. P. Ducheyne, Comprehensive biomaterials. Vol. 1. 2015: Elsevier.
4. J. Enderle, Introduction to biomedical engineering. 2012: Academic press.
5. L. Hench, and J. Jones, Biomaterials, artificial organs and tissue engineering. 2005: Elsevier.
6. H. Hench, L. Larry, and E. C. Ethridge. "Biomaterials: an interfacial approach." Academic Press, Inc., 1972, 385.
7. L. Sedel, Les biomatériaux. Service du Film de Recherche Scientifique, prod., éd 2000.
8. A.F. Von Recum, and M. Laberge, Educational goals for biomaterials science and engineering: prospective view. Journal of applied biomaterials, 1995. 6(2): p. 137-144.
9. J.B. Park, and J.D. Bronzino, Biomaterials: principles and applications. crc press, 2002.
10. D. Williams, A model for biocompatibility and its evaluation. Journal of biomedical engineering, 1989. 11(3): p. 185-191.
11. C.B. Carter, and M.G. Norton. "Ceramics in biology and medicine." Ceramic Materials: Science and Engineering, 2007: 635-651.
12. H. Mély, Modélisation de la transformation de biomatériaux par un modèle de percolation, thèse de doctorat, Université Blaise Pascal-Clermont-Ferrand II, 2011.
13. H. Azzeddine, A. Hanna, A. Dakhouche, B. Luthringer-Feyerabend,: Corrosion behaviour and cytocompatibility of selected binary magnesium-rare earth alloys. Journal of Magnesium and Alloys. 9, 2021, 2, 581 - 591. DOI: /10.1016/j.jma.2020.09.003.
14. A. Hanna, Etude de quelques propriétés des alliages à base de magnésium après déformation pour utilisation comme biomatériaux, thèse de doctorat, Université de M'sila. 2021.
15. J. Ong, M.R. Appleford, and G. Mani, Introduction to biomaterials: basic theory with engineering applications. Cambridge University Press, 2014.
16. P. Parida, A. Behera, and S. Mishra, Classification of Biomaterials used in Medicine. International Journal of Advances in Applied Sciences, 2012. 1. DOI: 10.11591/ijaas.v1i3.882.

17. J. Paulo Davim, Biomedical Composites. 2014: De Gruyter. DOI: 10.1515/9783110267488.

18. M. Arafat, P. Fouladian, A. Blencowe, H. Albrecht, Y. Song, S. Garg, Drug-eluting non-vascular stents for localised drug targeting in obstructive gastrointestinal cancers. Control Release, 2019. 308: p. 209-231. DOI: 10.1016/j.jconrel.2019.07.001.

19. S. Alijani, , A. Anvari, Cycle numbers to failure for magnesium and its alloys in human body fluid. Journal of Chemical Engineering, and M. Science. 2018. 9(1): p. 1-8.

20. S. Sakka, J. Bouaziz, and F. Ben Ayed, Sintering and mechanical properties of the alumina–tricalcium phosphate–titania composites. Materials Science and Engineering: C, 2014. 40: p. 92-101.DOI: 10.1016/j.msec.2014.03.036.

21. L. Hench, An introduction to bioceramics. Vol. 1. 1993: World scientific.

22. S. Raynaud, Synthèse, frittage et propriétés mécaniques de phosphates de calcium dans le système hydroxyapatite-phosphate tricalcique, thèse de doctorat, Université de Limoges. 1999.

23. D. Bernache-Assollant, , Chimie physique du frittage. 1993: Hermes.

24. S.V. Dorozhkin, Bioceramics of calcium orthophosphates. J Biomaterials. 2010. 31(7): p. 1465-1485. DOI: 0.1016/j.biomaterials.2009.11.050.

25. S.R. Paital, N. Dahotre, and E.R. Reports, Calcium phosphate coatings for bio-implant applications, Materials, performance factors, and methodologies. 2009. 66 (1-3): p. 1-70. DOI: 10.1016/j.mser.2009.05.001.

26. J.M. Thomine, Revue de Chirurgie Orthopédique et Réparatrice de l'Appareil Moteur, 2005. 91(2): p. 190. DOI: 10.1016/S0035-1040(05)84914-1.

27. N. Passuti, G. Daculsi, JM. Rogez, S. Martin, JV. Bainvel, Macroporous calcium phosphate ceramic performance in human spine fusion. Clinical orthopaedics and related research 1989 (248): p. 169-176.

28. N. Bouslama, F. Ben Ayed, and J. Bouaziz, Sintering and mechanical properties of tricalcium phosphate–fluorapatite composites. Ceramics International, 2009. 35(5): p. 1909-1917.DOI: 10.1016/j.ceramint.2008.10.030.

29. V. Dorozhkin, Sergey "A detailed history of calcium orthophosphates from 1770s till 1950. Materials Science and Engineering: C 33.6, 2013: 3085-3110.

30. D.E. Corbridge, Phosphorus: chemistry, biochemistry and technology. 2013: CRC press.

31. M. Bertolus, and M. Defranceschi, Les apatites: des phosphates naturels. 2004 (AF6610): p. AF6610. 1-AF6610. 8.

32. A.K. Lynn, and W. Bonfield, A Novel Method for the Simultaneous, Titrant-Free Control of pH and Calcium Phosphate Mass Yield. Accounts of Chemical Research, 2005. 38(3): p. 202-207. DOI: 10.1021/ar040234d.

33. R.I. Martin, and P.W. Brown, Phase Equilibria Among Acid Calcium Phosphates. The American Ceramic Society. 1997. 80(5): p. 1263-1266. DOI: 10.1111/j.1151-2916.1997.tb02973.x.

34. E.R. Kreidler, and F.A. Hummel, Phase relations in the system SrO-P2O5 and the influence of water vapor on the formation of $Sr_4P_2O_9$. Inorganic Chemistry, 1967. 6(5): p. 884-891. DOI: 10.1021/ic50051a007.

35. A.F. Fourcroy, , A general system of chemical knowledge, and its application to the phenomena of nature and art. Vol. 2. 1804: London, Cadell and Davies [et al.].

36. J.C. Elliott, Structure and chemistry of the apatites and other calcium orthophosphates. 2013: Elsevier.

37. S.V. Dorozhkin, Calcium orthophosphates: occurrence, properties,biomineralization, pathological calcification and biomimetic applications. J Biomatter. 2011. 1(2): p. 121-164. DOI: 10.4161/biom.18790.

38. S.V. Dorozhkin, Calcium orthophosphates: applications in nature, biology, and medicine. 2012: CRC Press.

39. G.E. Moore, On brushite, a new mineral occurring in phosphatic guano. American Journal of Science. 1865. 2(115): p. 43-44. DOI: 10.2475/ajs.s2-39.115.43.

40. C.U. Shepard, and C. Shepard Jr, ART. XLVII.--On two New Minerals, Monetite and Monite, with a notice of Pyroclasite. American Journal of Science. 1882. 23(137): p. 400.

41. J. Percy, CXVIII. Notice of a new hydrated phosphate of lime. in Memoirs and Proceedings of the Chemical Society. Royal Society of Chemistry. 1843. p.222-223. DOI : 10.1039/MP8430200222.

42. O. Suzuki, Octacalcium phosphate: osteoconductivity and crystal chemistry. Acta Biomaterialia. 2010. 6(9): p. 3379-3387. DOI : 10.1016/j.actbio.2010.04.002.

43. M. Bredig, , H. Franch, and H. Füldner, Beiträge zur Kenntnis der Kalk Phosphorsäure-Verbindungen. 1932. 38(3): p. 158-164. DOI : 10.1002/bbpc.19320380310.

44. T. Kanazawa, T.Umegaki. N. Uchiyama, Thermal crystallisation of amorphous calcium phosphate to α-tricalcium phosphate. Chemical Technology and Biotechnology. 1982. 32(2): p. 399-406. DOI : 10.1002/jctb.5030320206.

45. M.I. Kay, R. Young, and A.S. Posner, Crystal structure of hydroxyapatite. Nature. 1964, 204(4963): p. 1050-1052. DOI : 10.1038/2041050a0.

46. A.S. Posner, and F. Betts, Synthetic amorphous calcium phosphate and its relation to bone mineral structure. Accounts of Chemical Research. 1975, 8(8): p. 273-281.

47. M. Sadat-Shojai, M-T. Khorasani, E. Dinpanah-Khoshdargi, A. Jamshidi, Synthesis methods for nanosized hydroxyapatite with diverse structures, Acta biomaterialia, 2013, 9(8): p. 7591-7621. DOI: 0.1016/j.actbio.2013.04.012.

48. W. Suchanek, and M. Yoshimura, Processing and properties of hydroxyapatite-based biomaterials for use as hard tissue replacement implants. Journal of Materials Research, 1998. 13(1): p. 94-117. DOI: 10.1557/JMR.1998.0015.

49. V. Dorozhkin, Sergey Calcium orthophosphate coatings, films and layers. Progress in Biomaterials, 1.1, 2012: 1-40. DOI: 10.1186/2194-0517-1-1.

50. T. Dobson, C. Macfarquhar, and G. Gleig, Encyclopædia: Or, A Dictionary of Arts, Sciences, and Miscellaneous Literature; Thomas Dobson, at the Stone house, no. 41, South Second street. Vol. 18. 1798.

51. D. McConnell, Apatite: its crystal chemistry, mineralogy, utilization, and geologic and biologic occurrences. Springer Science & Business Media. Vol. 5. 2012.

52. G. Hilgenstock, , Eine neue Verbindung von P_2O_5 und CaO. 1883. 3(498): p. 13.

53. C. Moseke, and U. Gbureck, Tetracalcium phosphate: Synthesis, properties and biomedical applications. Acta Biomaterialia. 2010. 6(10): p. 3815-3823.
DOI: 10.1016/j.actbio.2010.04.020.

54. S. Zhang, , Biological and Biomedical Coatings Handbook: Applications. 2016: CRC Press.

55. R.Z. LeGeros, and B. Ben-Nissan, Introduction to synthetic and biologic apatites, in Advances in calcium phosphate biomaterials. 2014, Springer. p. 1-17.

56. R. Ebrahimi-Kahrizsangi, B. Nasiri-Tabrizi, and A. Chami, Characterization of single-crystal fluorapatite nanoparticles synthesized via mechanochemical method. Particuology. 2011. 9(5): p. 537-544. DOI: 10.1016/j.partic.2011.07.001.

57. B. Ben-Nissan, Advances in Calcium Phosphate Biomaterials Preface. 2014. 2: p. Ix-Xi.

58. A. Moshaverinia, S. Ansari, M. Moshaverinia. N. Roohpour, J.A. Darr, I. Rehman, Effects of incorporation of hydroxyapatite and fluoroapatite nanobioceramics into conventional glass ionomer cements (GIC), Acta Biomaterialia. 2008. 4(2): p. 432-440. DOI: 10.1016/j.actbio.2007.07.011.

59. C. Baddiel, and E. Berry, Spectra structure correlations in hydroxy and fluorapatite. Spectrochimica Acta. 1966. 22(8): p. 1407-1416.

60. B.I. Bogdanov, P.S. Pashev, J.H. Hristov, I.G. Markovska, Bioactive fluorapatite-containing glass ceramics. Ceramics International, 2009. 35(4): p. 1651-1655. DOI: 10.1016/j.ceramint.2008.07.021.

61. H. Qu, and M. Wei. The effect of fluoride contents in fluoridated hydroxyapatite on osteoblast behavior. Acta biomaterialia 2.1 (2006): 113-119.
DOI: 10.1016/j.actbio.2005.09.003.

62. B.H. Yoon, HW. Kim, SH. Lee, CJ. Bae, YH. Koh, YM. Kong, Stability and cellular responses to fluorapatite–collagen composites. Biomaterials. 2005. 26(16): p. 2957-2963.

63. W. Zhang, , L. Wang, and Z. Liu, The influence of fluoride on the development of the osteoblast phenotype in rat calvarial osteoblasts: an in vitro study. Shanghai journal of stomatology .1998. 7(2): p. 88-93.

64. J. Elliott, Handbook of Structure and Chemistry of the Apatite and Other Calcium Orthophosphates. Vol. 18. 1994, Elsevier Science: BV.

65. S. Náray-Szabo, The structure of apatite (CaF) Ca_4 $(PO_4)_3$. Zeitschrift für Kristallographie 75, 1930. 75: p. 387-398.

66. C.A. Beevers, and D.B. de McIntyre. The atomic structure of fluor-apatite and its relation to that of tooth and bone material.(with plates XVI-XVIII.)." Mineralogical magazine and journal of the Mineralogical Society 27.194, 1946: 254-257.

67. R.A.Young, Biological apatite vs hydroxyapatite at the atomic level. Clinical orthopaedics and related research 113, 1975: 249-262.
DOI: 10.1097/00003086-197511000-00036.

68. K. Sudarsanan, P. Mackie, and R. Young, Comparison of synthetic and mineral fluorapatite, Ca_5 $(PO_4)_3F$, in crystallographic detail. Materials Research Bulletin. 1972. 7(11): p. 1331-1337.

69. H. Njema, et al., Structural, electronic and thermodynamic properties of britholites Ca_{10-} xLax $(PO_4)_{6-}$ x (SiO_4) xF_2 (0≤ x≤ 6): Experiment and theory. Materials Research Bulletin. 2014. 51: p. 210-216.

70. T.I. Ivanova, O.V. Frank-Kamenetskaya, V.L. Ugolkov. A.B. Kol'tsov, Crystal structure of calcium-deficient carbonated hydroxyapatite. Thermal decomposition. Journal of Solid State Chemistry.2001. 160(2): p. 340-349.
DOI: 10.1006/jssc.2000.9238.

71. J. Emsley, Nature's building blocks: an AZ guide to the elements. 2011: Oxford University Press.

72. P.J. Dunn, E.U. Petersen, and D. Peacor, Turneaureite, a new member of the apatite group from Franklin, New Jersey, Balmat, New York and Långban, Sweden. The Canadian Mineralogist. 1985. 23(2): p. 251-254.

73. F.S. Beudant, Traité élémentaire de minéralogie. Vol. 3. 1824: Verdière.

74. O. Nakade, H. Koyama, J. Arai, H. Ariji, J. Takada, and T. Kaku, Stimulation by low concentrations of fluoride of the proliferation and alkaline phosphatase activity of human dental pulp cells in vitro. Archives of oral biology. 1999. 44(1): p. 89-92.
DOI: 10.1016/S0003-9969(98)00099-5.

75. H.W. Kim, S.Y. Lee, C. J. Bae, Y.J. Noh, H.E. Kim, H.M. Kim, and J.S. Ko, Porous ZrO_2 bone scaffold coated with hydroxyapatite with fluorapatite intermediate layer. Biomaterials.2003. 24(19): p. 3277-3284. DOI: 10.1016/S0003-9969(98)00099-5.

76. J.F. Osborn, and H. Newesely. "The material science of calcium phosphate ceramics." Biomaterials 1.2 (1980): 108-111.

77. H. El Feki, J.M. Savariault, A.B. Salah, and M. Jemal, Sodium and carbonate distribution in substituted calcium hydroxyapatite. Solid State Sciences. 2000. 2(5): p. 577-586. DOI: 10.1016/S1293-2558(00)01059-1.

78. F.B. Ayed, J. Bouaziz, K. Bouzouita, Calcination and sintering of fluorapatite under argon atmosphere. Journal of alloys and compounds 2001. 322(1-2): p. 238-245.

79. K.O.A. Chin, and G.H. Nancollas, Dissolution of fluorapatite. A constant-composition kinetics study. Langmuir, 1991. 7(10): p. 2175-2179.

80. R.S. Gilmore, and J.L. Katz. Elastic properties of apatites. Journal of Materials Science 17.4 (1982): 1131-1141. DOI: DOI: 10.1007/BF00543533.

81. R. Mazelsky, R.H. Hopkins, and W.E. Kramer. Czochralski-growth of calcium fluorophosphate. Journal of Crystal Growth, 3, 1968: 260-264.
DOI: 10.1016/0022-0248(68)90145-0.

82. S. Amrah Bouali, Étude de la fluoruration gazeuse et aqueuse de l'hydroxyapatite, thèse de doctorat, INPT.Toulouse, 1993.

83. F. Freund, and R. Knobel, Distribution of fluorine in hydroxyapatite studied by infrared spectroscopy. Journal of the Chemical Society, Dalton Transactions .1977(11): p. 1136-1140.

84. G. Montel, , Contribution à l'étude des mécanismes de synthèse de la fluorapatite, thèse de doctorat, Université de Paris,1958.

85. Hamed, M, Contribution à l'étude d'un mécanisme réactionnel d'une synthèse de la fluorapatite, thèse de doctorat, I.N.P. TOULOUSE, 1980.

86. G.B. Loutts, and B.H.T. Chai, Growth of high-quality single crystals of FAP ($Ca_5(PO_4)_3F$) and its isomorphs. Growth, Characterization, and Applications of Laser Host and Nonlinear Crystals II. Vol. 1863. International Society for Optics and Photonics, 1993, p. 31-34.

87. P. Ptáček, Synthetic phase with the structure of apatite, in Chemistry: Apatites and Their Synthetic Analogues-Synthesis, Structure, Properties and Applications. 2016, p. 177-244.

88. J. Berak, Rownowagi fazowe w ukladzie CaO-P. II. uklad czastkowy. Roczniki Chemii .1961. 35: p. 69.

89. D. Schauries, Ion Tracks in Apatite and Quartz: And Their Behaviour with Temperature and Pressure. 2018: Springer.

90. J. Heaney, Peter Structure and chemistry of the low-pressure silica polymorphs. Silica (2018): 1-40.

91. S. B. Holmquist, Conversion of quartz to tridymite. Journal of the American Ceramic Society 44.2 ,1961 : 82-86.

92. B. Viswanathan, , CO oxidation and NO reduction on perovskite oxides. Catalysis Reviews.1992. 34(4): p. 337-354.

93. P. Boch, Matériaux et processus céramiques. Hermes Science, Paris, 2001: p. 109-139.

94. V.A.C. Haanappel, J.B. Rem, H.D.van Corbach, T. Fransen and P.J. Gellings, Properties of alumina films prepared by metal-organic chemical vapour deposition at atmospheric pressure in the presence of small amounts of water. Surface and Coatings Technology.1995. 72(1-2): p. 1-12.

95. J. Müller, and D. Neuschütz, Efficiency of α-alumina as diffusion barrier between bond coat and bulk material of gas turbine blades. Vacuum, 2003. 71(1-2): p. 247-251.

96. B. Lux, ,C. Colombier, H. Altena and K. Stjernberg , Preparation of alumina coatings by chemical vapour deposition. Thin Solid Films. 1986. 138(1): p. 49-64.

97. N.D. Hoivik, J.W. Elam, R.J. Linderman, V.M Bright. S.M. George and Y.C. Lee, Atomic layer deposited protective coatings for micro-electromechanical systems. Sensors and Actuators A: Physical. 2003. 103(1-2): p. 100-108.

98. P. Mohan, , B. Yao, T. Patterson and Y.H. Soh., Electrophoretically deposited alumina as protective overlay for thermal barrier coatings against CMAS degradation. Surface and Coatings Technology. 2009. 204(6-7): p. 797-801.

99. Q. Zhang, P.S. Wang, W.J. Zhao and L. Wang, Ion beam assisted deposition of Al_2O_3 optical waveguides on silicon. Surface and Coatings Technology. 2000. 128: p. 121-125.

100. L.L. Hench, Genetic design of bioactive glass. Journal of the European Ceramic Society, 2009. 29(7): p. 1257-1265. DOI: 10.1016/j.jeurceramsoc.2008.08.002.

101. L.L. Hench, and H.A. Paschall, Direct chemical bond of bioactive glass-ceramic materials to bone and muscle. Journal of Biomedical Materials Research. 1973. 7(3): p. 25-42.DOI: 10.1002/jbm.820070304.

102. C. Wu, and J. Chang, A review of bioactive silicate ceramics. Biomedical Materials, 2013. 8(3): p. 032001. DOI: 10.1088/1748-6041/8/3/032001.

103. T. Kokubo, H. Kushitani, S. Sakka, , T. Kitsugi and T. Yamamuro, Solutions able to reproduce in vivo surface-structure changes in bioactive glass-ceramic A-W3. Journal of biomedical materials research. 1990. 24(6): p. 721-734.
DOI: 10.1002/jbm.820240607.

104. A. Forster, An assessment of the relationship between the water vapour permeability and hydraulicity of lime based mortars with particular reference to building conservation material science, PhD Thesis. Heriot-Watt University.UK. 2002.

105. P. Saravanapavan, J.R. Jones, S. Verrier , R. Beilby, V.J. Shirtliff, , L.L. Hench and J. M. Polak, Binary $CaO–SiO_2$ gel-glasses for biomedical applications. Bio-Medical Materials and Engineering, 2004. 14: p. 467-486.

106. F.S. Shirazi, M. Mehrali, A.A. Oshkour , H.S.C. Metselaar , N.A. Kadri and N.A. Abu Osman, Mechanical and physical properties of calcium silicate/alumina composite for biomedical engineering applications. Journal of the Mechanical Behavior of Biomedical Materials, 2014. 30: p. 168-175. DOI: 10.1016/j.jmbbm.2013.10.024.

107. L. Long, , F. Zhang, L. Chen, L. Chen and J. Chang , Preparation and properties of β-$CaSiO_3/ZrO_2$ (3Y) nanocomposites. Journal of the European Ceramic Society, 2008. 28(15): p. 2883-2887. DOI: 10.1016/j.jeurceramsoc.2008.05.006.

108. W. Liu, and J. Chang, Setting properties and biocompatibility of dicalcium silicate with varying additions of tricalcium aluminate. Journal of Biomaterials Applications. 2012. 27(2): p. 171-178. DOI : 10.1177/0885328211398507.

109. W.N. Liu, J. Chang, Y.Q. Zhu and M. Zhang, Effect of tricalcium aluminate on the properties of tricalcium silicate–tricalcium aluminate mixtures: setting time, mechanical strength and biocompatibility. International endodontic journal. 2011. 44(1): p. 41-50. DOI: 10.1111/j.1365-2591.2010.01793.x.

110. Z. Huan, , J. Chang, and X.-H. Huang, Self-setting properties and in vitro bioactivity of $Ca_2SiO_4/CaSO_4 \cdot 1/2H_2O$ composite bone cement. Journal of Biomedical Materials Research.2008. 87B(2): p. 387-394. DOI: 10.1002/jbm.b.31116.

111. E. De Bilbao, J. Poirier, and M. Dombrowski, Corrosion of high alumina refractories by Al2O3-CaO slag: thermodynamic and kinetic approaches. Metallurgical Research & Technology. 2015. 112(6): p. 607.DOI: 10.1051/metal/2015042.

112. E. Haccuria, , T. Crivits, , P.C. Hayes and E. Jak, , Selected phase equilibria studies in the Al_2O_3-CaO-SiO_2 system. Journal of the American Ceramic Society, 2015. p. 691-704. DOI: 10.1111/jace.13991.

113. L.J. Fuh, Y.J. Huang, W.C. Chen, D.J. Lin., Preparation of micro-porous bioceramic containing silicon-substituted hydroxyapatite and beta-tricalcium phosphate. Materials Science and Engineering: C . 2017. **75**: p. 798-806. DOI: 10.1016/j.msec.2017.02.065.

114. C. Lin, , Z. Chen, D. Yi, J. Chang, Y. Xiao., Multidirectional effects of Sr^-, Mg^-, and Si^- containing bioceramic coatings with high bonding strength on inflammation, osteoclastogenesis, and osteogenesis. ACS Applied Materials & Interfaces Forums, 2019. 365: p. 129-133. DOI: 10.1021/am4060035

115. A.F. Khan, , M. Saleem, A. Afzal, A. Ali, A. Khan, AR. Khan., Bioactive behavior of silicon substituted calcium phosphate based bioceramics for bone regeneration. Materials Science and Engineering: C. 2014. 35: p. 245-252. DOI: 10.1016/j.msec.2013.11.013

116. S.K. Padmanabhan, F. Gervaso, M. Carrozzo, F. Scalera, A. Sannino, A. Licciulli., Wollastonite/hydroxyapatite scaffolds with improved mechanical, bioactive and biodegradable properties for bone tissue engineering. Materials Science and Engineering: C . 2013. 39(1): p. 619-627.

117. S. Sprio, A. Tampieri, E. Landi, GC. Celotti, DD. Fabbriche., Bioactive Hydroxyapatite/Calcium Silicate Composites Obtained by Fast Hot Pressing: Structure and Flexural Strength. Key Engineering Materials. 2008. (361-363)p. 423-426.

118. A. Kenzour, , H. Belhouchet, M. Kolli, S. Djouallah, D. Kherifi, S. Ramesh., Sintering behavior of anorthite-based composite ceramics produced from natural phosphate and kaolin. Ceramics International. 2019. 45(16): p. 20258-20265. DOI: 10.1016/j.ceramint.2019.06.299.

119. L. Borkowski, A. Przekora, A. Belcarz, K. Palka, G. Jozefaciuk, T. Lübek, M. Jojczuk, A. Nogalski, G. Ginalska., Fluorapatite ceramics for bone tissue regeneration:

Synthesis, characterization and assessment of biomedical potential. Materials Science and Engineering: C. 2020. (116): p. 111-211. DOI: 10.1016/j.msec.2020.111211.

120. N. Golafshan, et al., Combinatorial fluorapatite-based scaffolds substituted with strontium, magnesium and silicon ions for mending bone defects. Materials Science and Engineering: C. 2021. 120: p. 111611. DOI: 10.1016/j.msec.2020.111611.

121. S. Djouallah, , H. Belhouchet, A. Kenzour, D. Kherifi., Sintering behavior of fluorapatite-based composites produced from natural phosphate and alumina. Ceramics International. 2021. 47(3): p. 3553-3564. DOI: 10.1016/j.ceramint.2020.09.202.

122. R.A. Youness, M.A Taha, M. Ibrahim., Dense alumina-based carbonated fluorapatite nanobiocomposites for dental applications. Materials Chemistry and Physics. 2021. 257: p. 123264. DOI: 10.1016/j.matchemphys.2020.123264

123. F. Ben Ayed, J. Bouaziz, I. Khattech, K. Bouzouita., Produit de solubilité apparent de la fluorapatite frittée. Annales de Chimie Science des Matériaux, 2001. 26(6): p. 75-86. DOI: pii/S015191070180101X.

124. R. Ebrahimi-Kahrizsangi, B. Nasiri-Tabrizi, and A. Chami, Synthesis and characterization of fluorapatite–titania (FAp–TiO_2) nanocomposite via mechanochemical process. Solid State Sciences, 2010. 12(9): p. 1645-1651. DOI: 10.1016/j.solidstatesciences.2010.07.017.

125. N. Bouslama, Y. Chevalier, J. Bouaziz, FB. Ayed., Influence of the sintering temperature on Young's modulus and the shear modulus of tricalcium phosphate – fluorapatite composites evaluated by ultrasound techniques. Materials Chemistry and Physics, 2013. 141(1): p. 289-297. DOI: 10.1016/j.matchemphys.2013.05.013.

126. A. Guidara, K. Chaari, and J. Bouaziz, Effect of Titania Additive on Structural and Mechanical Properties of Alumina–Fluorapatite Composites. Journal of Materials Science & Technology, 2012. 28(12): p. 1130-1136. DOI: 10.1016/S1005-0302(12)60182-0.

127. R. Taktak, A. Elghazel, J. Bouaziz, S. Charfi, H. Keskes., Tricalcium phosphate-Fluorapatite as bone tissue engineering: Evaluation of bioactivity and biocompatibility. Materials Science and Engineering: C, 2018. 86: p. 121-128. DOI: 10.1016/j.msec.2017.11.011.

128. D. Kherifi, H. Belhouchet, S. Ramesh, K.Y. SaraLeee, A. Kenzour, S. Djoualah, M.K.G. Abbas, Y.H. Wong, S. Ramesh., Sintering behaviour of fluorapatite–silicate composites produced from natural fluorapatite and quartz. Ceramics International, 2021.DOI: 10.1016/j.ceramint.2021.02.216.

129. A. Guidara, K. Chaari, S. Fakhfakh, J. Bouaziz., The effects of MgO, ZrO_2 and TiO_2 as additives on microstructure and mechanical properties of Al_2O_3-Fap composite. Materials Chemistry and Physics, 2017. 202: p. 358-368. DOI: 10.1016/j.matchemphys.2017.09.039.

130. S.J. Kim, HG. Bang, JH. Song, and SY. Park., Effect of fluoride additive on the mechanical properties of hydroxyapatite/alumina composites. Ceramics International, 2009. 35(4): p. 1647-1650. DOI: 10.1016/j.ceramint.2008.07.016.

131. A. Yelten, S. Yilmaz, and F.N. Oktar, Sol–gel derived alumina–hydroxyapatite–tricalcium phosphate porous composite powders. Ceramics International, 2012. 38(4): p. 2659-2665.DOI: 10.1016/j.ceramint.2011.11.032.

132. T. Ikegami, , K. Kotani, and K. Eguchi, Some roles of MgO and TiO_2 in densification of a sinterable alumina. The American Ceramic Society. 1987. 70(12): p. 885-890. DOI: 10.1111/j.1151-2916.1987.tb04911.x.

Chapter 2

Materials and experimental techniques

This chapter is devoted to describing experimental materials and techniques for the powders and sintered samples used in this study. In this context, the bioceramic preparation processes, as well as the equipment used for the Physico-chemical characterization of the prepared samples, are described.

I.1. Materials used

In this study, we used two local materials: Natural phosphate and quartz and laboratory alumina and titanium oxide.

I.1.1. Natural Phosphate (Natural FAp) and natural quartz

Natural phosphate was obtained from the al-Onq Mountain mine, in Bled Elhadba, south of the city of Tebessa, southeast of Algeria. The Al-Onq Mountain, about 20 kilometers long, consists of a series of sedimentary layers and includes many sectors or phosphate formations found in the Sinon Cave [1, 2] (Fig. II.1).

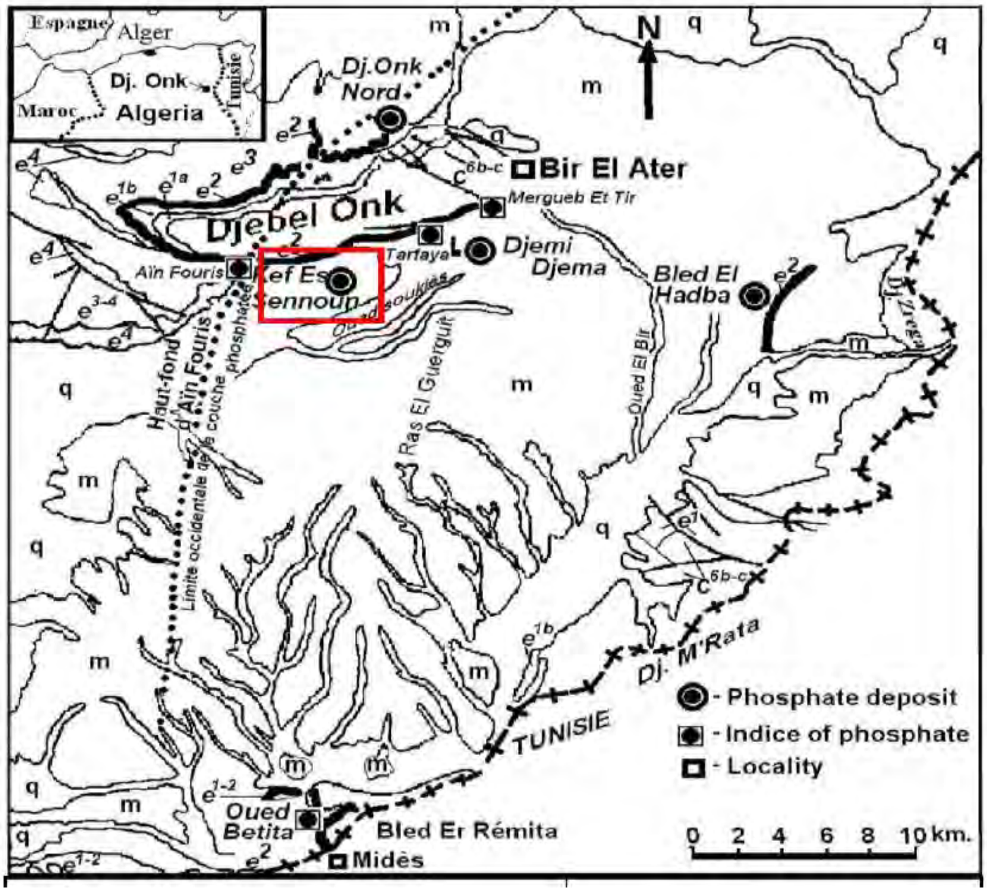

Fig. II.1: Geological map of phosphate deposits in Al-Onq Mountain[1].

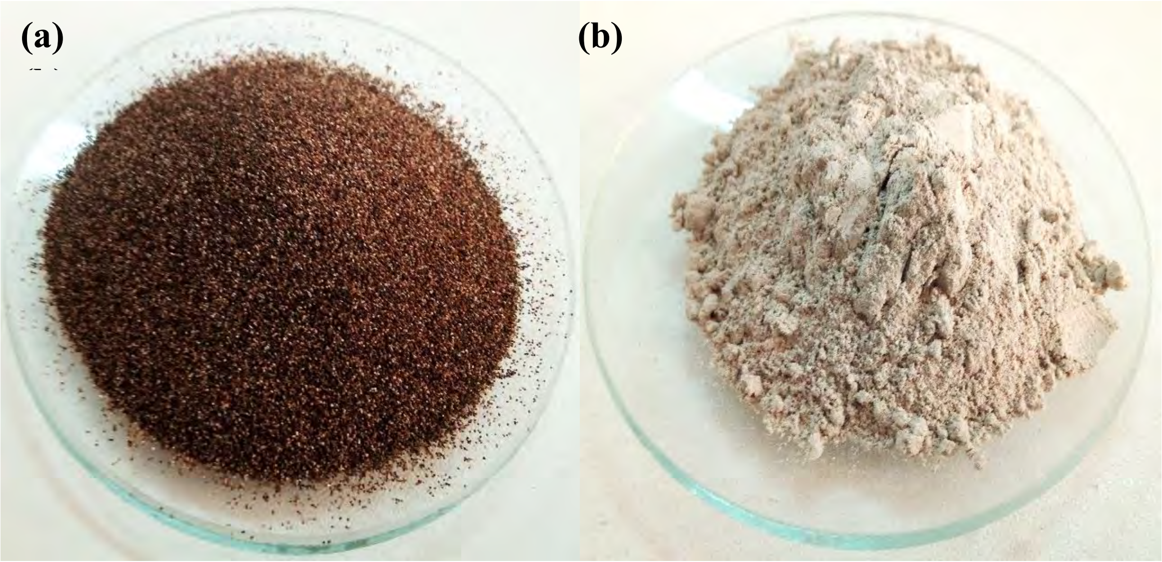

Fig. II.2: The phosphate used in this study: **(a)** before milling, **(b)** after milling.

Anhydrous silica comes in three crystalline forms: quartz, tridymite, cristobalite, and a non-crystallized form, silica glass.

Quartz is one of the most abundant of these species on earth's crust. Quartz is found in igneous rocks (granite and granulite) and sedimentary rocks (sands, sandstone, and quartzite), which can be extracted in their pure state by washing them with acids. In this work, we used natural quartz of southern Algerian origin (Tamanrasset) to develop bioceramics.

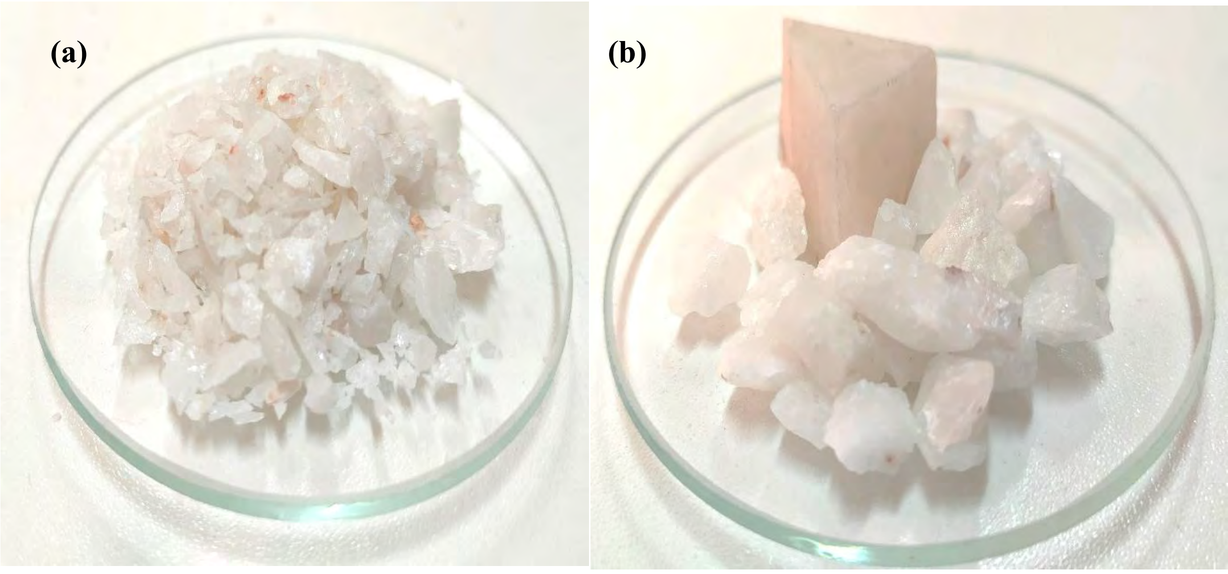

Fig. II.3: The Quartz used in this study.

I.1.2. Alumina (Al_2O_3)

Due to its numerous applications, alumina (Al_2O_3) is a well-known engineering material. The excellent properties of alumina, such as strength, refractoriness, chemical stability, and electrical insulation, make it used in most applications. Alumina is slightly soluble in heavy acids and alkalis. As a consequence, alumina is commonly used in surgical instruments. Because of its resistance to the chemical attack in the living environment (in vivo) and bioinertness, alumina was first used as part of prostheses in the 1970s. It is an excellent material for stability and long-term service in the body's environment.

In this study, we use pure Al_2O_3 from sigma-Aldrich.

I.1.3. Titanium dioxide (TiO_2)

Titanium dioxide (TiO_2), which is widely used in photocatalysis and photovoltaics, is increasingly finding applications in biomedical sciences. Its adaptable physicochemical properties and high compatibility with biological systems have prompted its use in tissue engineering, drug delivery, cancer therapy, and many other areas of research.

II. Methods and devices used to prepare powders and samples

The starting materials used in the first work were natural FAp and natural quartz (Q), varying amounts of quartz, such as 2.5, 5, 10, and 20 wt% were mixed with FAp, and samples were subsequently labeled as FA2.5Q, FA5Q, FA10Q, and FA20Q, respectively. The powder mixing was accomplished with a planetary ball mill (Fritsch P6) at a rotation speed of 350 rpm for 10 h with 15 min of rest for every route [3-10]. This grinding is designed for intensive grinding, homogenization, and reduction of the powder particle size (micronation). As the name implies, the jar rotates around its axis of revolution in one direction and around the grinding plate axis in the opposite direction (Fig. II.4).

Planetary milling is based on the intense impact and collision (ball-ball and ball-wall of the jar); these impacts cause the fragmentation of particles and consequently the reduction of their size (Fig. II.1) [11, 12]. In fact, in planetary milling, during the rotation of the jar (which generally rotates at twice the speed of the plate), the balls acquire a very high speed, and consequently, an extremely high kinetic energy. Since the plate rotates in the opposite direction, the resultant centrifugal forces oblige the balls to separate from the jar wall and cross the jar diagonally with speed acquired, hitting other balls in their path or reaching the opposite wall of the jar [11, 12].

In a typical powder preparation, the required amounts of quartz and FAp powders were measured and placed inside a 250 ml zirconia jar containing zirconia balls (10 mm diameter) as the milling media and distilled water as the milling medium. The resulting mixture was dried at 120 °C for 24 h and sieved through a 160 µm mesh sieve after milling was completed. The resulting powder was calcined at 900 °C for 2 h at a heating rate of 10 °C/min to remove any residual organic (univ of M'sila).

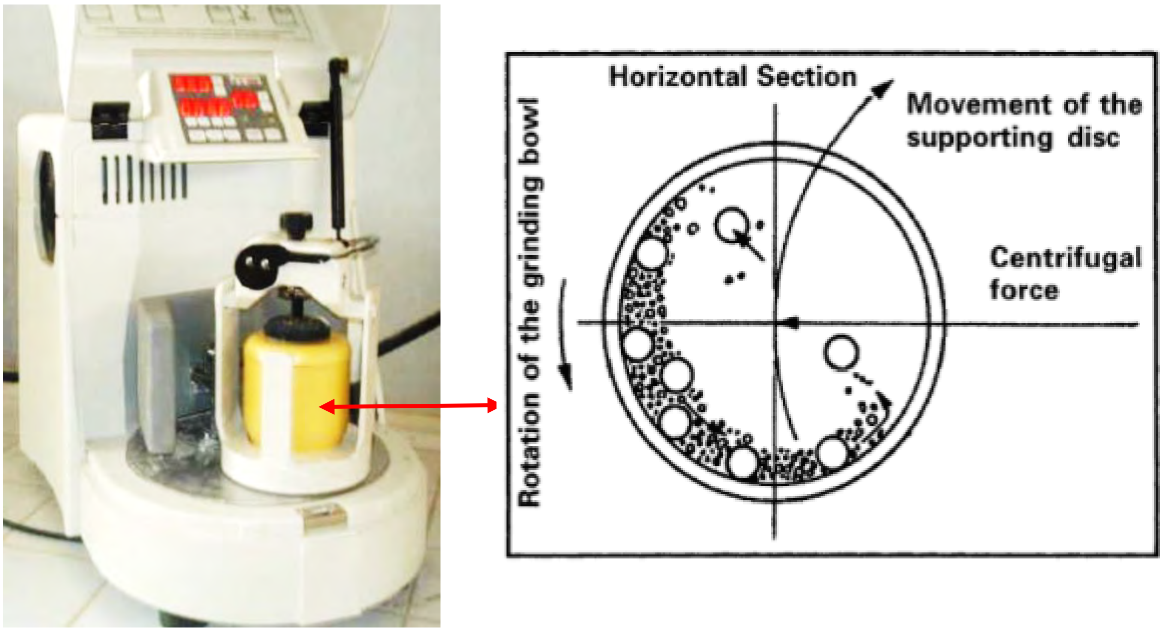

Fig. II.4: Planetary Ball Mill (Fritsch P6) and Schematic depicting the ball motion inside the planetary ball mill.

Shaping powders is a necessary step in the production of ceramics, with the aim of moving from a pulverized to a solid-state and giving the finished piece the shape of the mold in which the procedure is carried out. Pressure can be applied to shape powders in a variety of ways. The simplest of these methods is uniaxial pressure, in which the powder is placed into a metal mold and then compacted by pushing a punch (or by a hydraulic press) into the die. Since only one punch moves (the application of force in one direction), this technique is known as uniaxial pressing [13].

In our study, the powders were uniaxially pressed at 100 MPa to produce disc samples (13 mm diameter). The green samples were then pressureless sintered in air at various temperatures between 1000°C and 1350°C for 2 h at a heating rate of 10°C/min using Nabertherm electric furnace reaches a maximum temperature of 1750°C (univ of M'sila).

In the second investigation, we prepared alumina-fluorapatite composites from powders of two raw materials: pure laboratory aluminum oxide (Al_2O_3) and natural phosphate (N-P) was used as a starting material.

The initial composite was prepared by blending 25 Wt% of natural phosphate with 75 Wt% of alumina powders using an attrition milling. The attritor is also known as a "stirred ball mill" since it often refers to quick and fast processing. The attrition ball-milling process is a straightforward and efficient method. The content is comminuted in attrition by free-moving beads that are set in motion by a stirrer[12].

This mill, also known as the Szegvari attritor grinding mill, is represented in Fig. II.5. The starting materials are loaded into a stationary tank with the milling media in this mill (balls). Milling tools (vials and balls) fabricated from Carbon steel, stainless steel, chrome steel, tungsten carbide, and ceramic (zirconia) are all options. The milling operation is carried out by the agitation action of an agitator, which consists of a vertical revolving central shaft with horizontal arms known as impellers (Fig. II.5). It rotates at speeds of up to 500 rpm. Some high-speed attrition mills can spin at speeds ranging from 400 to 2000 rpm [12].

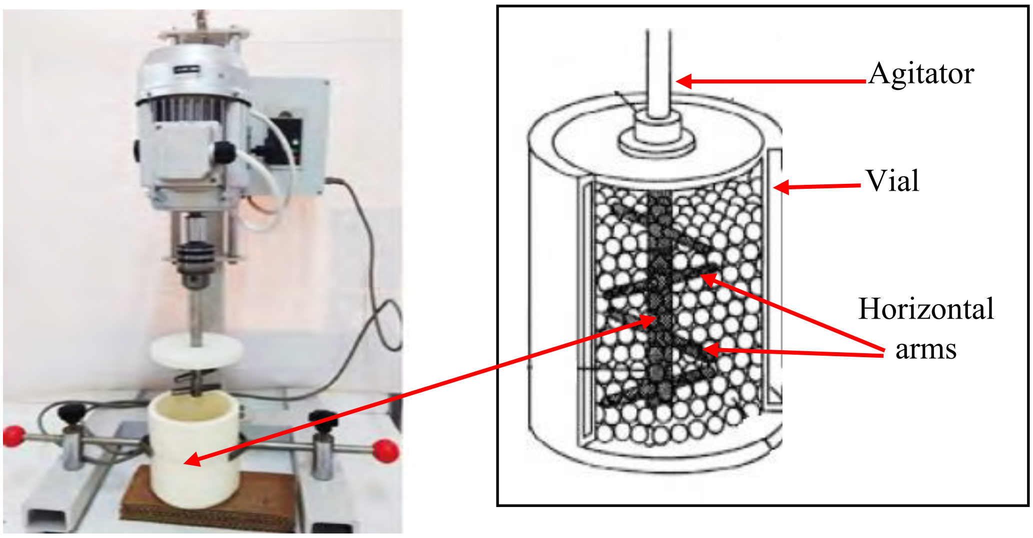

Fig. II.5: Attritor Ball Mill and Schematic depicting the ball motion inside the attritor ball mill.

Each mixture was loaded into an attritor milling in the presence of distilled water (100ml:100g). To improve the reaction and homogeneity of the mixture, the mass of the powder is 1/10 of the mass of the zirconia balls with diameters ranging from (1 to 3mm); the powder is stirred by a fixed rotation axis, at a rotation speed of 700 rpm for an hour. The additive used in this study was a high-purity titanium oxide powder, and different amounts of TiO_2 (1, 3, 5, and 10Wt%) were mixed to the alumina-fluorapatite composite using the same procedure mentioned previously and subsequently labeled as PHA0T, PHA1T, PHA3T, PHA5T, and PHA10T, respectively.

The slurry was dried at 120°C in a Memmert oven (UNB400) for 24 h, then crushed manually and sieved through a 160 µm mesh sieve. The powders were then compacted under a pressure of 100 MPa using a uniaxial press to produce cylindrical samples with a diameter of 13 mm. Green samples were sintered in air at different temperatures between 1000 and 1600°C for 2h using a standard heating and cooling ramp rate of 10°C/min.

III. Characterization techniques

III.1. X-ray fluorescence

The objective of XRF spectroscopy is to identify the elemental composition by detecting the fluorescent X-rays that the sample emits when irradiated with a primary X-ray beam. When the primary X-ray beam strikes this sample, three different interaction processes can be performed [14]:

The first type of interaction process is elastic scattering, called Rayleigh scattering. The incident X-ray beam is elastically scattered by electrons in the sample atom. The scattered x-ray photon has the same energy as an incident x-ray photon, but it changes direction [15, 16].

In the second type of interaction, the incident X-ray beam is inelastically scattered by the electrons of the sample atom. The total energy of the incident x-ray photon is split between the electron and the scattered x-ray photon. The energy and direction of the scattered x-ray photon change. This type of inelastic scattering is called Compton scattering (Fig. II.6). Compton scattering gives a continuous spectrum due to the many possible energy distributions between the electron and the scattered X-ray photon [16].

The third and most important interaction process is the photoelectric effect. This effect can be explained by the Bohr atomic model. The incident X-ray beam interacts with the atom by transferring all the energy to an electron on one of the inner layers. This energy is sufficient to remove the electron from the layer, creating a vacuum in that layer.

Subsequently, this gap is filled by an electronic transition from an outer orbit, which can result in either the emission of an X-ray photon (XRF emission) with an energy corresponding to the difference between the binding energies of two orbitals or the emission of an Auger electron.

The X-ray emitted during this return to steady-state (so-called fluorescence X-ray) is characteristic of the chemical elements constituting the sample being analyzed, and consequently, the detection and analysis of the sample sequences can be carried out.

In this work a ZSX Primus IV XRF was used (Fig. II.7)(univ setif 1).

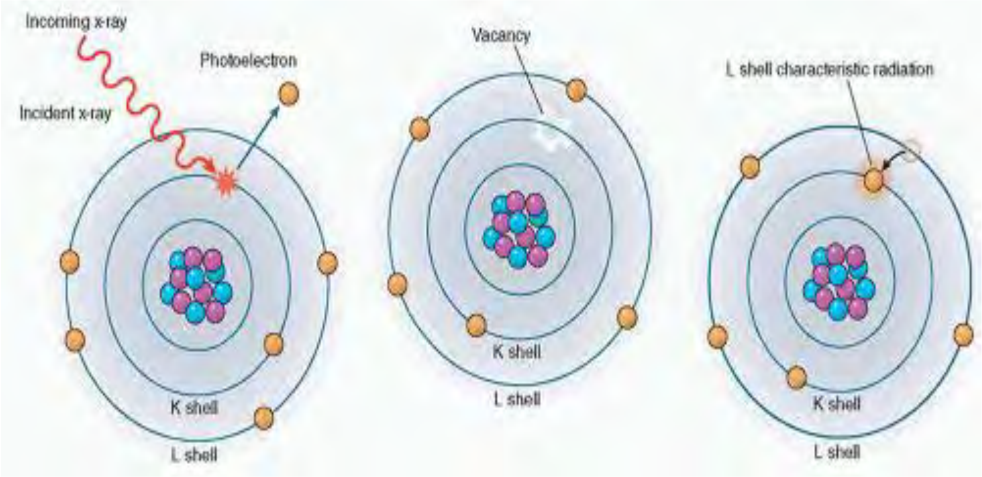

Fig. II.6: The principle photoelectric effect of XRF [7].

Fig. II.7: XRF ZSX Primus IV.

III.2. Granulometric analysis by laser

The central idea of light scattering to measure the particle size distribution of powders by laser diffraction is the inverse proportion between particle size and diffraction angle. Indeed, a series of particles will produce a light scattering spectrum defined by intensity and angle that can be transformed into a result of the particle size distribution [17].

Granulometry by laser diffraction consists at least of a high-intensity monochromatic light source, a sample handling system to control the interactions between particles and incident light, and a set of high-quality photodiodes to detect light scattered over a wide range of angles [14]. Furthermore, the process of laser granulometry is based on the theory of Gustav Mie, who developed his model taking into account, in addition to the diffracted beam, other beams: refracted, absorbed, and reflected, resulting from the interaction of the laser with a homogeneous series of spherical particles[17, 18].

In this study, a Horiba LA-960 laser particle sizer was used (Fig. II.8), where measurements were made dry, under ultrasonic vibration, with an air pressure of 0.39MPa. The particle size distribution is measured in relation to the volume. The refractive index (calculated) of the powders ranges between 1,6 and 1,65 (univ setif 1).

Fig. II.8: Horiba LA-960 laser granulometry.

III.3. Thermal analysis (TGA/DTA)

The TGA technique is based on measuring the mass of the model continuously whenever the temperature and time change. The change in mass, whether increase or decrease, is recorded by a high-sensitivity electromagnetic balance, and these measurements are recorded in a computer connected to the scale that will be studied later in the form of a curve representing the evolution of mass as a function of temperature and time.

The technique for differential thermal analysis (DTA) is similar to that of TGA, except that it measures the temperature difference between the sample and the reference material and then records this difference as a function of temperature, time, and mass.

We performed differential thermal analysis experiments on the prepared powders using the LABSYS Evo DSC Setaram 1600°C, which could perform both TG, DTA, and DSC, to determine the phase transitions, crystalline and amorphous, during the heat treatment in the case of phase formation (univ of M'sila).

III.4. X-ray diffraction (XRD)

The X-ray diffraction technique is a non-destructive analytical tool for characterizing crystalline or semi-crystalline materials; it can also be used to identify the phases present in samples, it can commonly differentiate between phases that have the same chemical composition but different crystal structures (polymorphs). X-ray powder diffraction (XRPD), as it is called, is the most widely used method for identifying unknown substances by comparing diffraction data with a database of powder diffraction files (PDF) maintained by the International Centre for Diffraction Data (ICDD). It can also be used to characterize heterogeneous solid mixtures to determine the relative abundance of crystalline compounds and when coupled with lattice refinement techniques [16, 17]. In XRD, when X-rays hit an atom, they move the electron cloud like any electromagnetic wave. The wavefields re-emitted by the atoms interfere with each other constructively or destructively, producing a diffraction pattern on a detector or film. The resulting wave interference spectrum is the basis for the diffraction analysis [19].

The interference is constructive when the phase shift is a multiple of λ; this condition can be expressed by Bragg's law:

$$2d.\sin\theta = n\lambda$$

Where **θ**: is the angle between the incident ray and the scattering planes,

d: is the spacing between the planes in the atomic lattice,

n: is an integer determined by the diffraction order and λ is the X-ray wavelength [19].

Powder diffraction data are usually presented as a diffractogram in which the diffracted intensity **I**; is shown as a function of the scattering angle 2θ [16].

The phases present in the powders and sintered composites were identified through X-ray diffraction (XRD, X'Pert Pro, Panalytical) with CuKα radiation at 40 kV and 30 mA. The scan was conducted at a speed of 4°/min and step scan of 0.026°, over the 2θ from 20° to 55°. The phase identification was accomplished by comparing the XRD signatures of the sample with the database provided by the Joint Committee on Powered Diffraction Standards (JCPDS) (univ of M'sila).

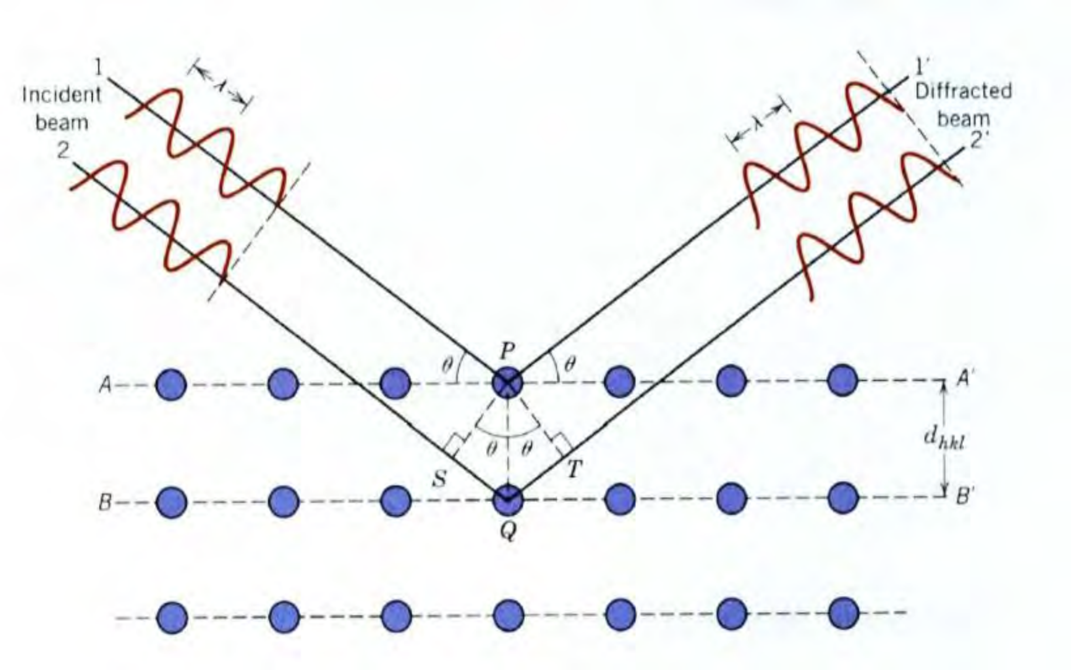

Fig. II.9: X-ray diffraction phenomenon[15].

Fig. II.10: Panalytical X'pert Pro, X-ray Diffractometer.

III.5. Fourier transform infrared spectroscopy (FT-IR)

Infrared spectroscopy is a useful technique for characterizing materials and providing information about the molecular structure, dynamics, and environment of a compound [16].

The electromagnetic spectrum's infrared part is divided into three regions: the near, mid, and far-infrared. The mid-infrared, about 4000-400 cm^{-1} (30-1.4 µm), can be used to study vibrations and the associated rotational-vibrational structure [20].

The infrared spectrum of the sample is collected by passing a beam of infrared light through the sample. Infrared spectroscopy exploits the fact that molecules have specific frequencies at which they rotate or vibrate according to discrete energy levels.

There are two types of vibration (Fig. II.11):

- **Elongation:** also called valence vibration or "stretching" (like a spring), this mode concerns symmetric and asymmetric vibrations (νs, νas) of the molecule along with the bonds,

- **Deformations Inside and outside the plane:** In addition to the valence vibration, the bond angle. In addition to the valence vibration, the bonds' angle can change; this is called bending or deforming. These symmetrical and asymmetrical deformations (δ_p, δ_{hp}) can occur in the plane of the two bonds concerned or out of the plane.

This technique allows the characterization of molecular groups, gives information on the arrangement of these groups over greater distances, and distinguishes different phases of the same compound.

The resulting chemical functional groups were determined in the samples from the Fourier transform infrared spectroscopy (FTIR) spectra taken over the wavelength range of 2000 cm^{-1} to 400 cm^{-1} by using a Shimadzu IRAffinity-1S spectrophotometer. For this purpose, 2 mg of powder was mixed with 98 mg of potassium bromide for the FTIR study (univ Setif 1).

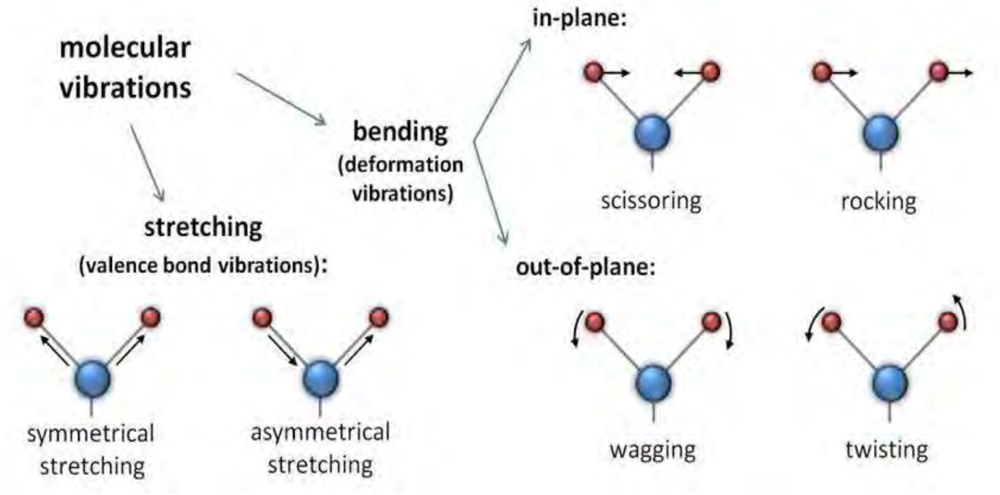

Fig. II.11: Vibrational modes of molecules[16].

Fig. II.12: SHIMADZU IRAffinity-1S FT-IR spectrometer.

III.6. Microstructural evolution

III.6.1. Field Emission Scanning Electron Microscope (FESEM)

The morphology, microstructure, and distribution of the sintered samples particles were examined by the Field Emission Scanning Electron Microscope (FESEM, the AURIGA, Zeiss). FESEM provides microstructural information at high magnification from 20 to 2000kx with nearly infinite field depth as it combines the advantages of optical and focal microscopy. FESEM results in clearer and less electrostatic-distorted images, with a spatial resolution of 1 1/2 nm, improved three to six times, compared to traditional Scanning Electron Microscope SEM[21].

Prior to FESEM observation, thermal etching was achieved by exposing the polished samples to a temperature at 50s°C below their respective sintering temperature for 30min at a ramp rate of 10°C/min to form grooves at grain boundaries. The thermal etched samples were placed on carbon tape and pinned on the microscope chamber. An electronic beam was released on the samples, and secondary electrons were used to capture images with a voltage of 10.0 kV and magnification ranging from 1.0 XK to 50.0 XK at different spots. One of the striking

Fig. II.13: AURIGA, Zeiss FESEM.

features of FESEM is that insulating materials do not need to be coated with conducting materials[21] (univ of Malaya, Malaysia).

III.6.2. Scanning Electron Microscopy (SEM)

The scanning electron microscope (SEM) is a type of microscope that creates various images by focusing a high-energy electron beam on the surface of a sample and detecting signals from the interaction of the incident electrons with the sample surfaces. The type of signals collected in an SEM varies and can include: secondary electrons, characteristic X-rays, and backscattered electrons[16]. In an SEM, the signals not only come from the primary beam striking the sample, but also from other interactions within the sample near the surface. SEM is capable of producing high-resolution images of the surface of a sample in its secondary electron imaging mode[16].

The large depth of field and wide range of magnifications make SEM the best known and widely used imaging technology. Backscattered electrons emitted by the sample can be used alone to form an image (an image with chemical contrast) or in conjunction with characteristic X-rays for the determination of the elemental composition of the sample [16, 22].

In our study, the SEM used is a QUANTA 250 scanning electron microscope (ENSMM Annaba) .

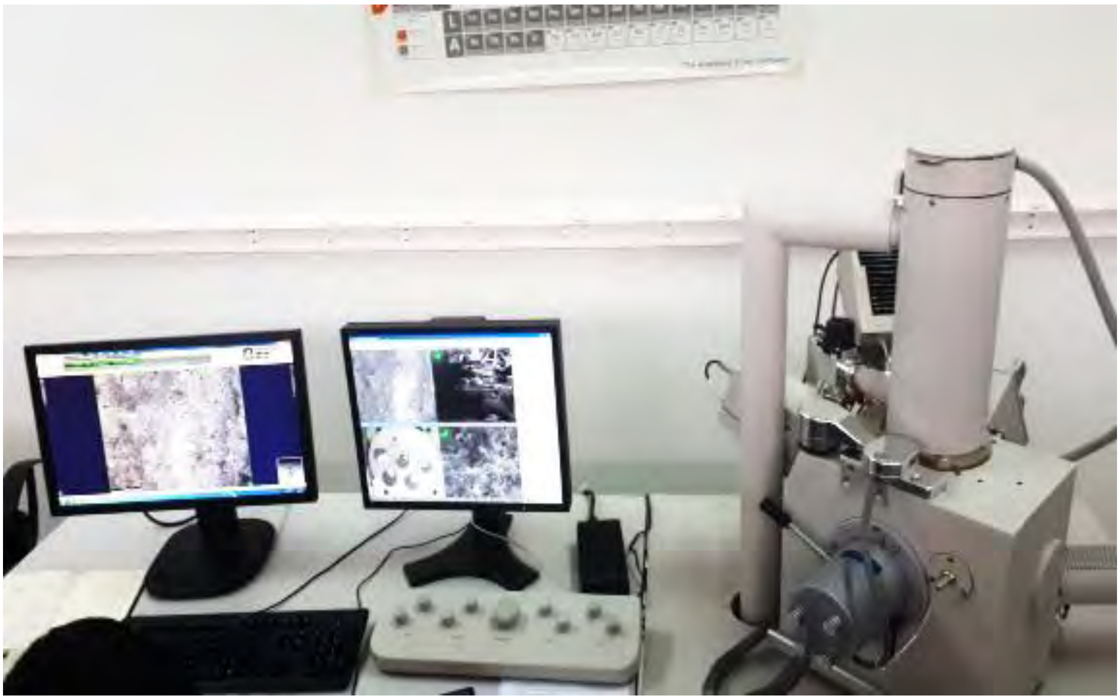

Fig. II.14: QUANTA 250 SEM.

III.7. Energy-Dispersive X-ray spectroscopy (EDX)

EDS (or EDX) is an analytical technique coupled with SEM equipment, mainly used for the elemental analysis or chemical characterization of a specimen. Being a type of spectroscopy, it is based on the study of a sample through the interactions between electromagnetic radiation (electron) and matters, analyzing the X-rays emitted by the matter in this particular case. The characteristic X-rays are emitted when the primary beam causes the ejection of electrons from the inner layer of the sample and uses to determine the elemental composition of the sample. Its capabilities for characterizations are largely due to the fundamental principle that every element on the periodic table has a unique atomic structure, allowing the characteristic X-rays of an element's atomic structure to be uniquely distinguished [16].At rest, an atom in the sample contains ground state (or unexcited) electrons located in discrete energy levels or electron shells bound to the nucleus. The incident beam can excite an electron in an inner layer, causing it to be ejected, which results in the formation of an electron-hole in the electron layer of the structure atom. An electron from the outermost layer of energy occupies the hole, and the energy difference between the upper and lower energy layers is released in the form of x-rays. The X-ray released by the electron is then detected and analyzed by the energy dispersion spectroscopy spectrometer. These X-rays are characteristic of the energy difference between the two layers and of the atomic structure of the element form they were emitted. A detector is used to convert the energy of the X-rays into voltage signals; this information is sent to a pulse processor, which measures the signals and passes them to an analyzer for viewing and analyzing the data [14, 16].

III.8. Micro-hardness HV

The microhardness test is a common test method for determining the hardness of various materials. The micro indentation test is a reliable and proven method for determining the hardness of small precision parts, materials or thin layers, and coatings. With the exception of test forces below 200 g, Vickers values are generally considered to be independent of the test force.

In other words, if the material under test is homogeneous, then the Vickers values would be the same if the test performed with a force of 500 g or 50 kg. Therefore, caution should be exercised below 200 g when attempting to compare results. Vickers test methods are defined in terms of the force used in ASTM E384 for micro-force ranges (10g-1kg) and ASTM E92 for macro-force ranges (1kg-100kg).

According to the standards, the Vickers micro-hardness test consists of the following steps:

- The indenter is driven into the surface of the sample by a controlled test force.
- The force is held for a specific dwell time, normally 10-15 s.
- Once the holding time has elapsed, the indenter is drawn out, leaving a dashed line in the sample surface.
- The size of the indentation is visually determined by measuring the two diagonals of the indentation squared.
- The Vickers hardness number is a function of the test force divided by the dash area. The mean of the two diagonals is used in the following formula to calculate the Vickers hardness:

$$H_V = 1.8544 \times \frac{P}{d}$$

Where: **Hv** is the microhardness value.

P is the applied load.

d is average diagonal lengths = $(\frac{d_1+d_2}{2})$.

The Vickers microhardness testing machine (Zwick Roell Indentec) was used to measure the hardness of the sintered samples under an indentation load of 300 g and a loading time of 10 s. Prior to the hardness test, the samples were well polished. Five to ten measurements were taken on each sample to determine the average hardness (univ of M’sila).

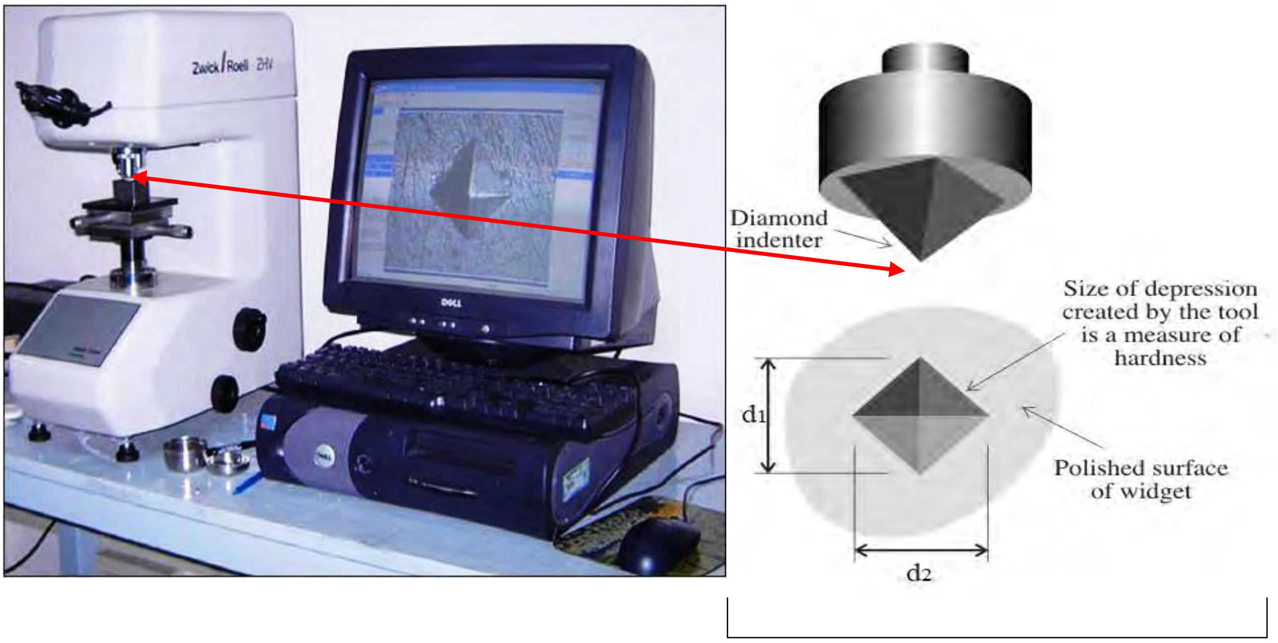

Fig. II.15: Zwick Roell Indentec machine and schematic showing the principle of functioning of hardness Vickers.

III.9. Measurement of bulk density and porosity

We used the Arthur principle in our measurements to determine the bulk density and percentage of open porosity for sintered samples at various temperatures. First, we measured the mass of the sample in the air using an electromechanical balance with a sensitivity of about 10^{-4} g; following that, we used a vacuum pump to extract the air from the sample under low pressure and replace it with xylene, after which the new mass was measured in the air and then in water. The bulk density and the ratio of open porosity to the total volume were determined using the equations below:

$$D_{bulk}\ (g/cm^3) = \frac{m_1 de}{(m_2 - m_3) - (m_2 - m_1) de/dx} \ldots \ldots . . (1)$$

$$O.P\ (\%) = 100 \frac{m_2 - m_1}{m_2 - m_3} \ldots\ldots\ldots . (2)$$

Where: **D_{bulk}:** the bulk density.

O.P: percentage of open porosity.

m_1: the mass of the sample in the air.

m_2: the mass of the sample filled with xylene in air.

m_3: the mass of the sample filled with xylene in water.

de: the density of water (0.9989 g/cm^3).

dx: density of xylene (0.88 g/cm3).

III.11. Measurement of Shrinkage

The linear shrinkage (L.S.%) was determined by the equation (ASTM C326) [23]:

$$L.S\ \% = \frac{D_1 - D_2}{D_1} * 100 \text{........(2)}$$

Where: **L.S.%:** Linear Shrinkage.

D_1 and **D_2** represent the diameters of the samples before and after sintering, respectively.

III.12. Mechanical tests

III.12.1. Tensile strength: indirect tensile (Brazilian test)

In 1978, the Brazilian test was formally introduced by the International Society for Rock Mechanics as a proposed method for determining the tensile strength of rock materials. The American Society subsequently used it for Testing and Materials (ASTM) to identify the tensile strength of concrete [24, 25].

This technics consists of applying a compressive force on two opposite generatrixes of a cylinder. The applied force induces tensile and compressive stresses within the specimen, particularly in the plane containing the cylinder's axis and the generatrix, thus mode I of rupture. Claussen proves that the diametral plane linking the contact between the sample and the two plates is uniformly in tension, assuming the elastic behaviour of the sample [26]. If the thickness of the specimen is less than its diameter, an increasing load creates a stress distribution that gradually increases until failure [27].

The test has been used to calculate the tensile strength of concrete [28], ceramics and cemented carbides [29], pharmaceutical materials in dosage forms[30], and other brittle materials.

Frochet shows that the maximum stress at rupture σ_r is obtained from the equation [31]:

$$\sigma_r = \frac{\mathrm{F}}{\mathrm{S}} = \frac{2\mathrm{F}}{\pi \mathrm{De}} \text{......(3)}$$

Where: **F** is the maximum load applied upon failure, **D** is the diameter of the sample, and **e** is its thickness.

This test has the benefit of being easy to perform (Fig. II.16). In fact, if one is only interested in determining tensile strength, only the material of the simple compression test is needed for its results. In the case that one desires to determine additional stiffness moduli and other parameters, various additional displacement measurements are required [32].

Tests are performed at a constant speed (1mm/min) and at room temperature on an Instron 3369 universal testing machine (univ of Malaya, Malaysia)..

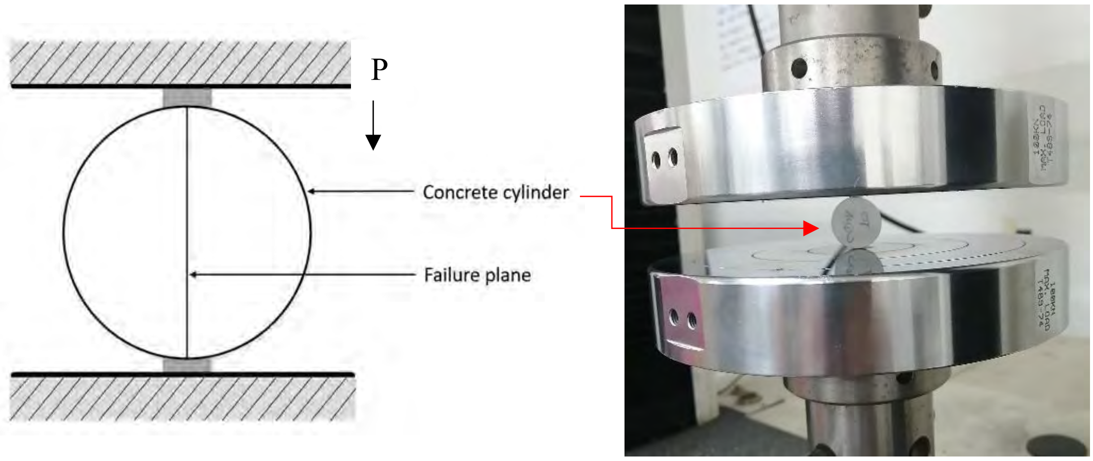

Fig. II.16: Indirect tensile strength test apparatus (Brazilian test).

III.13. In-vitro bioactivity test 'immersion in simulated body fluid (SBF).'

In this test, We examined the biological response (bioactivity) of samples prepared in vitro. In vitro culture (immersion in SBF) allows chemical elements to be incorporated into the material, influencing cellular physiology and changing the biomaterial's biological properties.

These in vitro experiments are the first step toward understanding the behaviour of our biomaterial.

In this study, SBF was used as a soaking solution ionic concentrations close to those found in human blood plasma (H-BP, table II.1) to evaluate the kinetic reactivity of the prepared samples. SBF was prepared by dissolving reagent grade CaC_{l2}, NaCl, KCl, $MgC_{l2}.6H_2O$, $K_2HPO_4.3H_2O$, and $NaHCO_3$ (Table II.2) in deionized water, according to Kokubo's protocol [33, 34].

Tris – hydroxymethyl aminomethane $(HOCH_2)_3CNH_2$ and hydrochloric acid (HCl, 1M) were used to buffer it at pH 7,4.

The samples were immersed in SBF for 1, 3, and 16 weeks at 37°C. After soaking, the samples were separated from the buffered SBF solution and dried after being washed with ethanol. We then performed observations by Field Emission Scanning Electron Microscope (FESEM, the AURIGA, Zeiss) and XRD (X'Pert Pro, Panalytical) in order to analyze and followed the appearance of the apatite phase on the surface of the material during the immersion time (univ of Malaya, Malaysia)..

Table II.1: The ion concentration of SBF and human blood plasma [33, 34].

	Ion concentration (mmol/l)							
	Na+	K+	Mg2+	Ca2+	Cl^-	HCO3-	HPO_4^{2-}	SO_4^{2-}
SBF	142,0	5,0	1,5	2,5	147,8	4,2	1,0	0,5
H-BP	142,0	5,0	1,5	2,5	103	4,2	1,0	0,5

Table II.2: Order, reagents and quantity for the preparation of one liter of SBF, HCl(ml).

Order	**1**	**2**	**3**	**4**	**5**	**6**	**7**	**8**	**9**	**10**
Reactive	NaCl	NaHCO3	KCl	$K_2HPO_43H_2O$	$MgCl_26H_2O$	HCl	$CaCl_2$	Na2SO4	TRIS	HCl
Quantity(g)	8,035	0,335	0,225	0,231	0,311	39	0,292	0,072	6,118	1,5

References

1. A. Boudries, Etude geologique et geostatique de l'uranium (U) dans le gisement de phosphate de kef es-sennoun (algerie orientale). thèse de doctotat, Université Badji Mokhtar, Annaba. 2008.
2. H. Belhouchet , F. Sahnoune and M. Heraiz., Elaboration and Characterization of Bioceramics from Natural Phosphate, ACTA PHYSICA POLONICA A (APMAS2016), 2017, p. 117. DOI: 10.12693/APhysPolA.131.117
3. F. Sahnoune, H. Belhouchet, N. Saheb, M. Heraiz, M. Chegaar & P. Goeuriot, Phase transformation and sintering behaviour of mullite and mullite–zirconia composite materials, Advances in Applied Ceramics, 2011, 110:3, 175-180, DOI: 10.1179/1743676111Y.0000000004.
4. H. Belhouchet, M. Hamidouche, N. Bouaouadja, V. Garnier, G. Fantozzi Elaboration and characterization of mullite-zirconia composites from gibbsite, boehmite and zircon, Ceram. –Silik, 53, 2009, pp. 205-210.
5. H. Belhouchet, M. Hamidouche, R. Torrecillas, G. Fantozzi, The non-isothermal kinetics of mullite formation in boehmite–zircon mixtures, J. Therm. Anal. Calorim., 116 (2014), pp. 795-803. DOI: 10.1007/s10973-013-3601-6.
6. H. Belhouchet, H. Makri, M. Hamidouche, N. Bouaouadja, V. Garnier, G. Fantozzi Elaboration and characterization of multiphase composites obtained by reaction sintering of boehmite and zircon, J. Australas. Ceram. Soc., 50 (2014), pp. 135-146
7. F. Chouia, H. Belhouchet, F. Sahnoune, F. Bouzrara, Reaction sintering of kaolin-natural phosphate mixtures, Ceram. Int., 41 (2015), pp. 8064-8069. DOI: 10.1016/j.ceramint.2015.03.003.
8. M. Heraiz, F. Sahnoune,b, H. Belhouchet, N. Saheb, Synthesis of Al_2O_3 containing mullite from Algerian Kaolin and Boehmite, Journal of Optoelectronics and Advanced Materials, 2013. 15, pp. 1263-1267.
9. A. Mokhtari, H. Belhouchet and F. Sahnoune, The Effects of B_2O_3 Addition on the Properties of Anorthite Prepared from Algerian Kaolin, ACTA PHYSICA POLONICA A (APMAS2016), 134, 2018, p. 460. DOI: 10.12693/APhysPolA.134.460.

10. H. Belhouchet, T. Sahraoui, K. Belhouchet, and & M. Romero. Influence of heating rate and mechanical activation on the reaction between kaolin and aluminium powder. J Aust Ceram Soc 55, 2019, p. 135–144. DOI: 10.1007/s41779-018-0219-y.
11. C. Burmeister, L. Titscher, S. Breitung-Faes, A. Kwade., Dry grinding in planetary ball mills: Evaluation of a stressing model. Advanced Powder Technology, 2018. **29**(1): p. 191-201.DOI: 10.1016/j.apt.2017.11.001.
12. M.S. El-Eskandarany, The history and necessity of mechanical alloying, in Mechanical Alloying (Second Edition), M.S. El-Eskandarany, Editor. 2015, William Andrew Publishing: Oxford. p. 13-47.DOI: 10.1016/B978-1-4557-7752-5.00002-4.
13. S. Laasri, Étude comparative des caractéristiques physicochimiques et mécaniques des biomatériaux à base de phosphate de calcium, d'alumine et de zircone: Caractérisation et modélisation. thèse de doctorat, Université Ibnou Zohr, Agadir, MAROC, 2013.
14. R. Whan, Metals handbook, Vol. 10, Materials characterization. 1988. **27**(6): p. 1002.
15. R. Fosbinder, and D. Orth, Essentials of radiologic science. 2011: Lippincott Williams & Wilkins.
16. J.E. Penner-Hahn, , Handbook of X-ray Spectrometry, Revised and Expanded Edited by René E. Van Grieken (University of Antwerp) and Andrzej A. Markowicz (Vienna, Austria). Marcel Dekker, Inc: New York and Basel. 2002. xvi+ 984 pp. ISBN 0-8247-0600-5. 2002, ACS Publications.
17. M.A. Cyr, A. Tagnit-Hamou, Particle size distribution of fine powders by LASER diffraction spectrometry. Case of cementitious materials. Materials and Structures. 2001. **34**(6): p. 342-350.
18. A. Boualem, , Estimation de distribution de tailles de particules par techniques d'inférence bayésienne, thèse de doctorat, Université Université d'Orléans, France, 2016.
19. S.Amelinckx, , M. Rodewald, V. Buschmann., Handbook of Microscopy: Applications in Materials Science, Solid-State Physics, and Chemistry, Methods II. 2008: John Wiley & Sons.
20. K. Nakamoto, Infrared and Raman Spectra of Inorganic and Coordination ompounds, Part A: Theory and Applications in Inorganic Chemistry, 6th Edition. 2006.
21. A. Mayeen, L. Shaji, L. ShajiAnju, K. Nair, AK. Nair, N. Kalarikkal., Chapter 12 - Morphological Characterization of Nanomaterials, in Characterization of Nanomaterials, 2018, Woodhead Publishing. p. 335-364. DOI: 10.1016/B978-0-08-101973-3.00012-2.

22. C. Suryanarayana, Microstructure: An Introduction, in Aerospace Materials and Material Technologies : Volume 2: Aerospace Material Technologies, N.E. Prasad and R.J.H. Wanhill, Editors. 2017, Springer Singapore: Singapore. p. 105-123. DOI: 10.1007/978-981-10-2143-5_6.

23. K.Belhouchet, A. Bayadi, H. Belhouchet, M. Romero., Improvement of mechanical and dielectric properties of porcelain insulators using economic raw materials. Boletín de la Sociedad Española de Cerámica y Vidrio, 2019. **58**(1): p. 28-37.DOI: 10.1016/j.bsecv.2018.05.004.

24. M.N.J. AlAwad, Modification of the Brazilian indirect tensile strength formula for better estimation of the tensile strength of rocks and rock-like geomaterials. Journal of King Saud University - Engineering Sciences, 2020. DOI: 10.1016/j.jksues.2020.08.003.

25. E. Sgambitterra, C. Lamuta, S. Candamano and L. Pagnotta., Brazilian disk test and digital image correlation: a methodology for the mechanical characterization of brittle materials. Materials and Structures, 2018. **51**(1): p. 19. DOI: 10.1617/s11527-018-1145-8.

26. N. Claussen, and J. Jahn, Green strength of metal and ceramic compacts as determined by the indirect tensile test. Powder met int. 1970. **2**(3): p. 87-90.

27. M. Riera, J. Prado, and A. Larsson. Determination of the green Strength of Powder Metallurgical Compacts by means of the Brazilian test. in Powder Metallurgy World Congress. PM’00. 2000.

28. G.Hondros, The evaluation of Poisson's ratio and the modulus of materials of low tensile resistance by the Brazilian (Indirect tensile) test with particular reference to concrete. Australian J. Appl. Sci., 1959. **10** (3): p. 243-268.

29. M.C. García-Leiva, I. Ocaña, A. Martín-Meizoso, J.M. Martínez-Esnaola., Fracture mechanics of Sigma SM1140+ fibre. Engineering Fracture Mechanics, 2002. **69**(9): p. 1007-1013. DOI:10.1016/S0013-7944(01)00117-5.

30. J.T. Fell, and J.M. Newton, Determination of Tablet Strength by the Diametral-Compression Test. Journal of Pharmaceutical Sciences, 1970. **59**(5): p. 688-691. DOI: 10.1002/jps.2600590523.

31. M. Frocht, Photoelasticity. Vol. 2. 1946: J. Wiley.

32. Q.Z. Wang, XM. Jia, SQ. Kou, ZX. Zhang, PA. Lindqvist., The flattened Brazilian disc specimen used for testing elastic modulus, tensile strength and fracture toughness of

brittle rocks: analytical and numerical results. International Journal of Rock Mechanics and Mining Sciences, 2004. **41**(2): p. 245-253.
DOI: 10.1016/S1365-1609(03)00093-5.

33. T. Kokubo, and H. Takadama, How useful is SBF in predicting in vivo bone bioactivity? . Biomaterials, 2006. **27**(15): p. 2907-2915.
DOI: 10.1016/j.biomaterials.2006.01.017.

34. F-Z. Mezahi, Caractérisations physico-chimiques et Cinétique de bioactivité des biomatériaux: Hydroxyapatite & Verre bioactif 52S4 élaboré par fusion et par voie sol-gel, thèse de doctorat, Université Mentouri, Constantine , 2009.

Chapter 3

Results & Discussions

Part I: *Sintering behaviour of fluorapatite–silicate composites produced from natural fluorapatite and quartz.*

In this part, silicate-doped FAp composites were prepared for the first time by mixing natural FAp and quartz. This work aimed to investigate the effects of quartz addition up to 20 wt% on the phases and densification behavior of FAp when subjected to pressureless sintering.

I.1. Physicochemical and morphological analyses of the initial materials

I.1.1. Chemical analysis of natural phosphate and quartz

The chemical compositions of FAp and quartz as determined from the XRF are presented in Table III.1. The FAp in its natural form is composed mainly of CaO (59.9%) and P2O5 (28.2%), whereas the quartz comprises predominantly 99.9% SiO2 with high purity.

Table III.1: Chemical composition (wt%) of natural FAp and natural quartz used in this study.

Elements	**F**	**Na_2O**	**MgO**	**Al_2O_3**	**SiO_2**	**P_2O_5**	**SO_3**
FAp	3.65	1.13	0.89	0.87	1.79	28.2	2.55
Q	-	0.85	0.75	0.027	99.9	0.001	-
	K_2O	**CaO**	**Fe_2O_3**	**ZnO**	**SrO**	**Y_2O_3**	**L.O.I.**
	0.138	59.9	0.455	0.038	0.345	0.044	-
	0.002	0.001	0.005	-	-	-	0.01

I.1.2. XRD analysis of natural phosphate and quartz

The XRD spectrum of the starting FAp (Fig. III.1) showed that fluorapatite (JCPDS No. 15-876) and francolite (JCPDS No. 31-267) are the major phases, whereas dolomite (JCPDS No. 83-1530) and calcite (JCPDS No. 47-1743) represent the minor phases. For the natural quartz, silica (JCPDS No. 46-1045) was identified as the main phase (Fig. III.2).

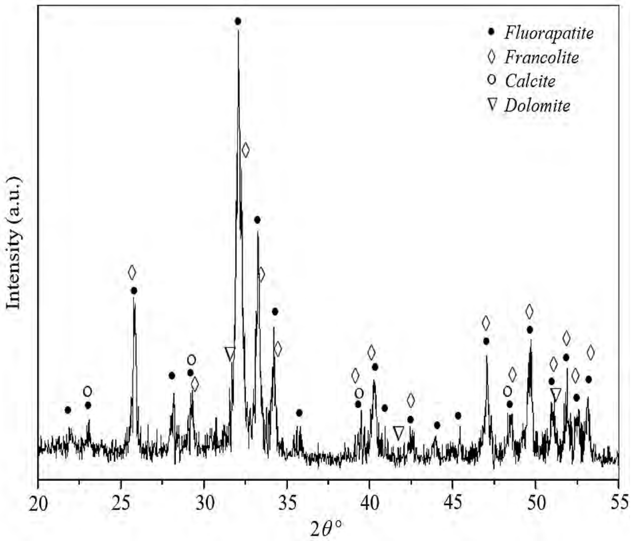

Fig. III.1: XRD analysis of the as-received natural FAp powder showing a mix phase was present.

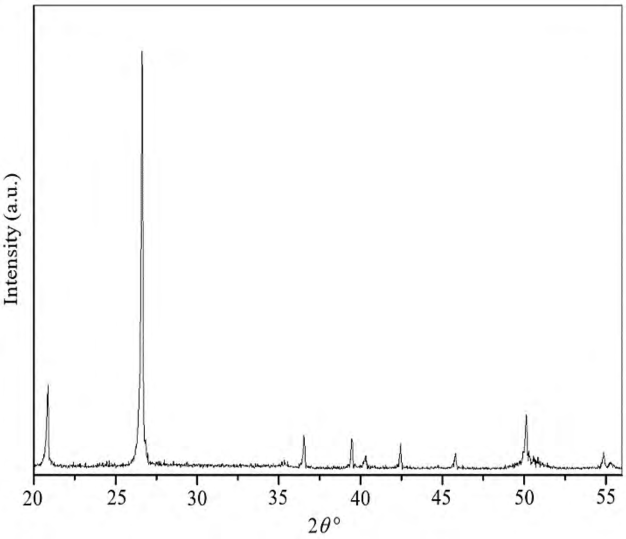

Fig. III.2: XRD pattern of the as-received natural quartz. All the peaks belongs to the SiO_2 phase.

I.1.3. Morphological observation of natural phosphate

SEM micrographs of a particle of the unground rock phosphate powder used in this study are shown in Figure III.3.a. Both images display an aggregate morphology, or in other words, the phosphate powder particles are made up of micrometric grains of any form, which are made up of very fine nanometric particles agglomerated together. The similar observations are illustrated in Bachoua et al. research on Tunisian rock phosphate [1].

Figure III.3.b indicates the particle size of milled phosphate powder. After 1 hour of milling, both photos show homogenate morphology, or in other words, the phosphate powder particles are made up of nanometric grains.

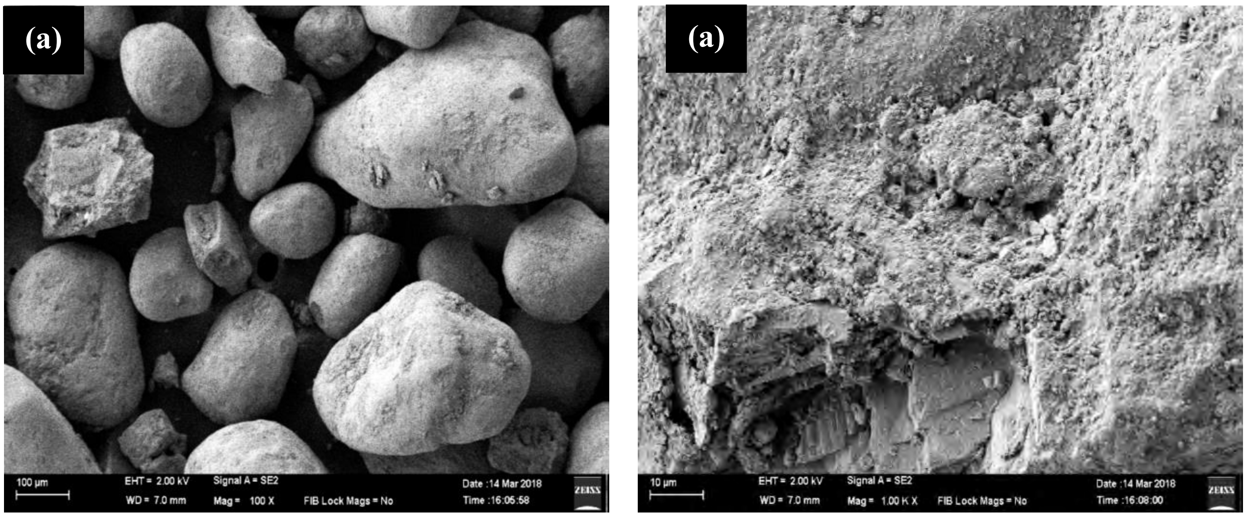

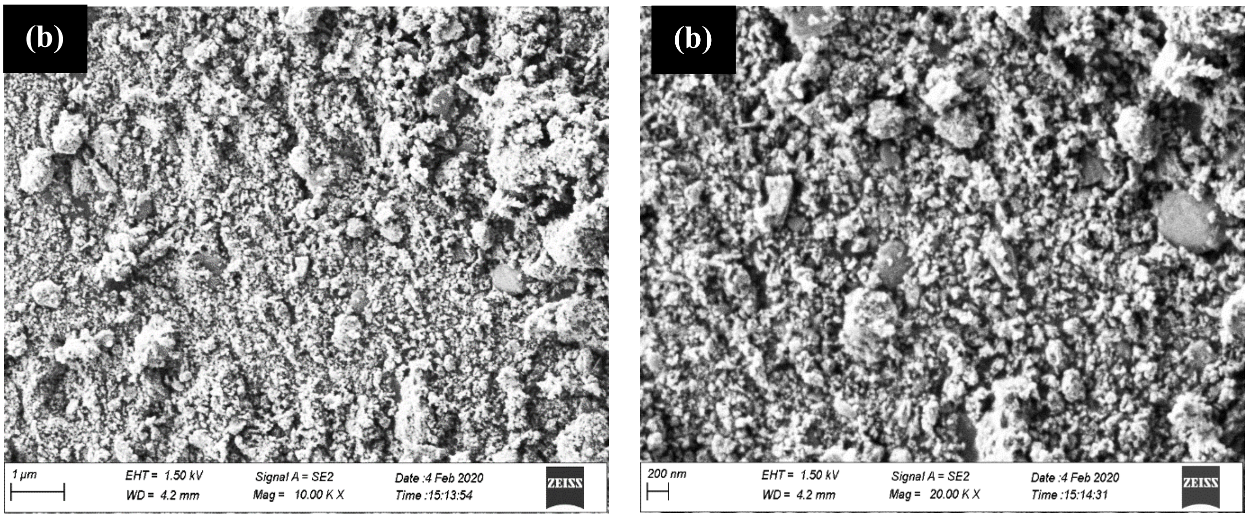

Fig. III.3: SEM observations of Natural Phosphate, a; before milling, b; after 1h millig.

I.2. DTA analysis of mixtures

The differential thermal analysis (DTA) of all mixtures is shown in Figure III.4. (under argon). These curves display a single exothermic peak between 743 and 794°C, which is attributed to fluorapatite recrystallization [2, 3].

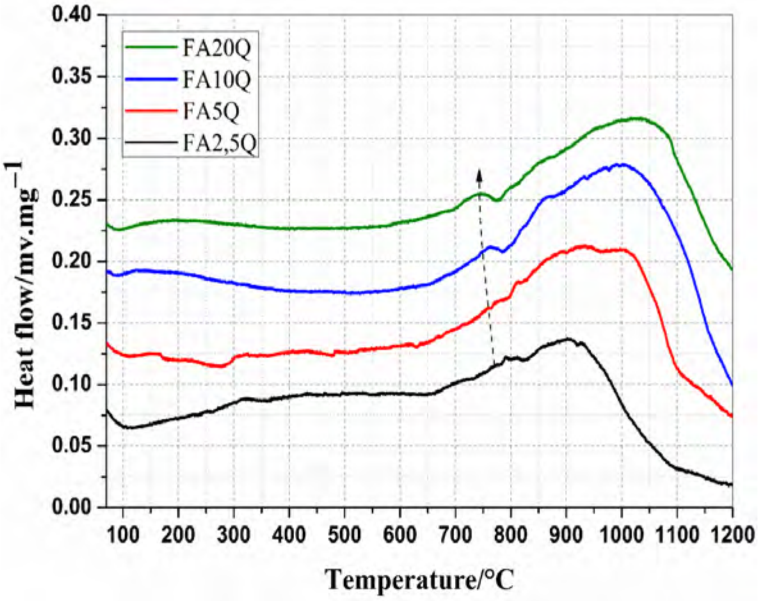

Fig. III.4: DTA curves of the mixture powders (FAp/Q: FA2.5Q, FA5Q, FA10Q and FA20Q).

I.3. Particle size analysis of mixtures

The results of the particle size distribution measurements of the powders after grinding are presented in Fig. III.5. The analyses show a bimodal distribution of all ground powders. The first type belongs to FAp; it is almost nanometric, as the average particle diameter of D50 is approximately the same for all powders (about 260 nm). On the other hand, a second type belongs to quartz with an increase (from 11 to 26 μm) was observed towards the right the higher the quartz content.

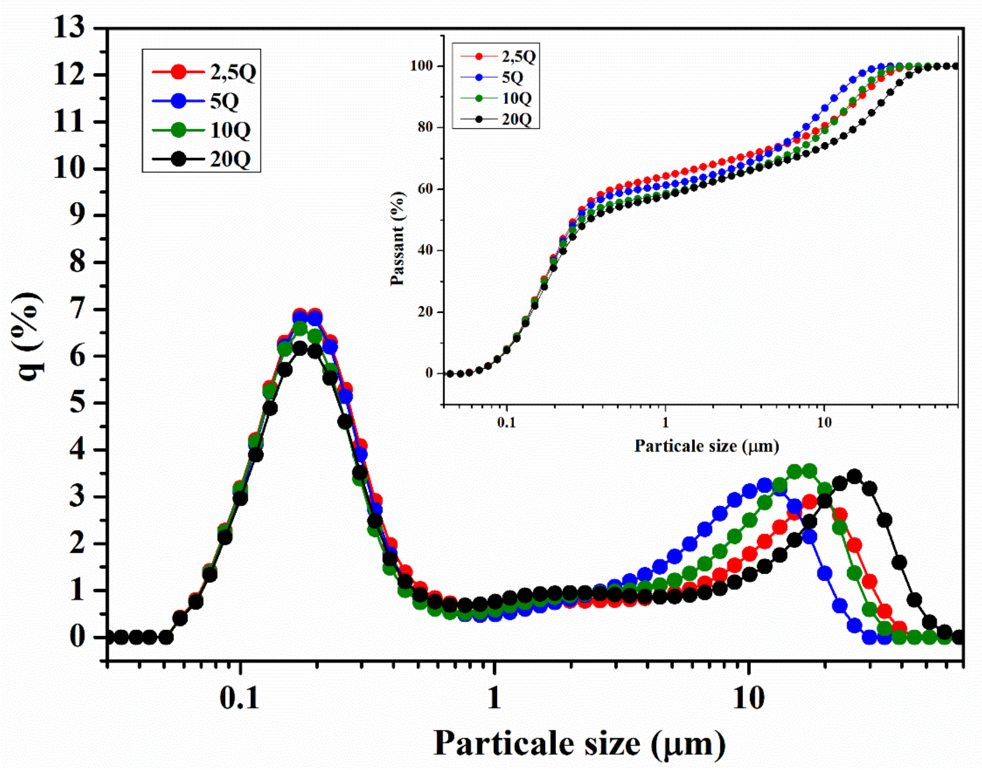

Fig. III.5: Particle size distribution of milled powders.

I.4. Physicochemical analysis of milled powders before and after calcination

The XRD patterns of the composite powders before calcination are shown in Fig. III.6. Regardless of the quartz content, all mixtures exhibited the major crystalline phases of FAp and quartz, with small amounts of calcite and dolomite. The intensity of quartz, which is noticeable at $2\theta = 26.5$ °, increases with the increased in quartz content in the mixture powder.

The FTIR spectra of the composite powders before calcination are presented in Fig. III.7. The strong bands detected at 870 and 1385 cm^{-1} and the weak bands at 1424 and 1457 cm^{-1} are related to the presence of CO_3^{2-} group [4, 5]. With the increase in the quartz content in FAp, the intensity of these bands decreases. Another strong band at 966 cm^{-1} is related to the mode ν_1 of PO_4^{3-} group, and the band at 1094 and 1043 cm^{-1} corresponds to the mode ν_3 of PO_4^{3-} group [5, 6]. Two distinctive bands at 603 and 570 cm^{-1} are associated with the ν_4 of PO_4^{3-}

group [5]. The intensity of the bands related to the PO_4^{3-} group does not change with the addition of quartz. The bands at 823, 800, 779, 670, 515, and 463 cm^{-1} are associated with the silicate Si–O–Si network vibrations [4, 7, 8]. As expected, the intensity at 823 cm^{-1} strengthens with the increase in quartz content [2, 3]. The effects of calcination on the phases present in the composite powders are shown in Fig. III.8.

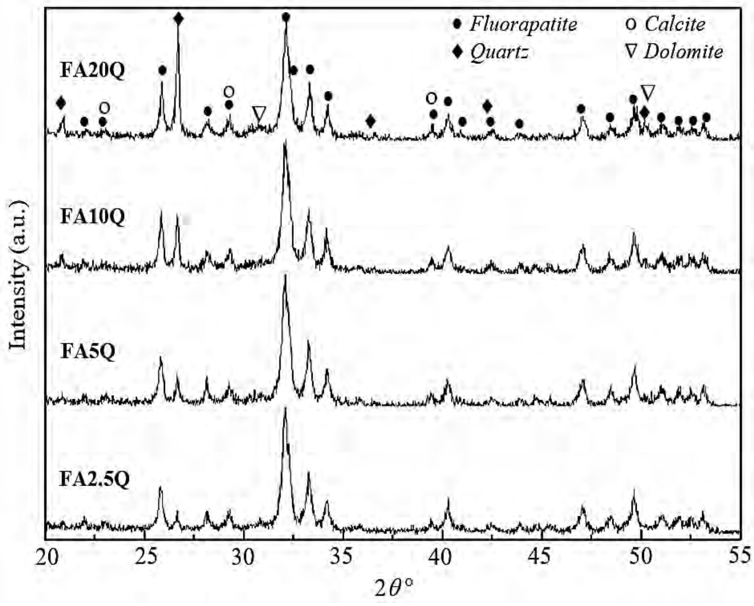

Fig. III.6: Comparison of XRD signatures of the composite powders before calcination.

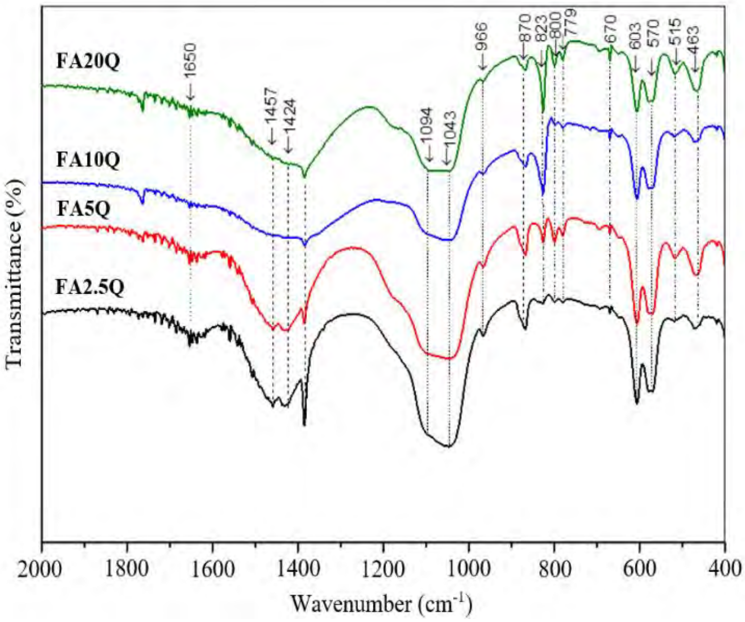

Fig. III.7: FTIR spectra of composites before calcination.

All composites consist of the major crystalline phases of FAp regardless of the quartz addition. The peak corresponding to that of quartz, particularly at $2\theta \sim 26.5°$, is clearly visible for the FA20Q sample when compared with the undoped powder (FA0Q). The phases that appeared in the composites after calcination include cristobalite (JCPDS No. 39-1425), wollastonite (JCPDS No. 43-1460), and whitlockite (JCPDS No. 09-0169). A strong peak of cristobalite is evident for the composite with 20 wt% quartz addition. Quartz starts to transform into cristobalite at approximately 1190 °C and above [9]. However, in this work, the transformation from quartz to cristobalite occurred at a low temperature of 900 °C. A reaction between the FAp and excess quartz contributed to the reduction in quartz–cristobalite transformation temperature. The wollastonite peak started to appear when the composition of quartz was increased to 10 wt%. Free calcium oxide (CaO) decomposed from calcite ($CaCO_3$) and dolomite $CaMg(CO_3)_2$ due to the calcination at 900 °C [10]. The formation of wollastonite ($CaSiO_3$) as observed for FA10Q and FA20Q samples was due to the reaction between the free CaO and cristobalite (SiO_2) based on reaction [11]. In accordance with Eq. (1).

$$CaO+SiO_2 \rightarrow CaSiO_3 \qquad (1)$$

The formation of wollastonite was also due to the reaction between the calcite and excess SiO_2 present in the composites (FA10Q and FA20Q) in accordance with Eq. (2).

$$CaCO_3 + SiO_2 \rightarrow CaSiO_3 + CO_2 \qquad (2)$$

In this work, the presence of whitlockite (tricalcium phosphate) in FA5Q can be associated with the decomposition of FAp at the calcination temperature to form tricalcium phosphate and CaF_2 [12]. In accordance with Eq. (3).

$$Ca_{10}(PO_4)_6F_2 \rightarrow 3Ca_3(PO_4)_2 + CaF_2 \qquad (3)$$

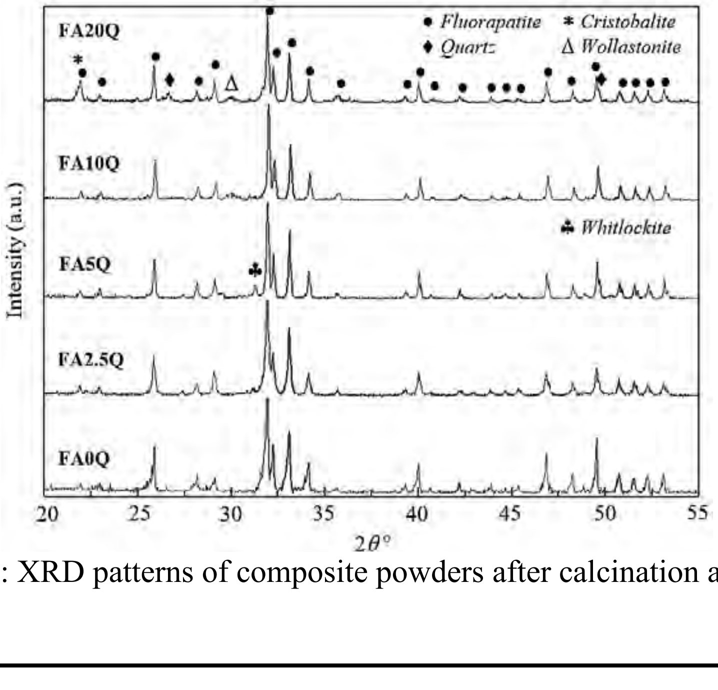

Fig. III.8: XRD patterns of composite powders after calcination at 900 °C.

I.5. Analysis of shaped and sintered samples

I.5.1. X-ray analysis of samples after sintering

The XRD patterns of the composites containing different amounts of quartz and sintered at varying temperatures are shown in Figs. III.9 (a–d). The presence of FAp is clearly visible in all the composites regardless of the sintering temperatures and quartz content. The intensity of FAp is low in FA20Q (Fig. I.9,d) when sintered at 1300 °C and 1350°C. This condition can be due to the partial fusion of FAp with quartz. For samples containing 5 wt% quartz and above, a trace of whitlockite was detected at $2\theta \sim 31.5°$ when sintered from 1000°C to 1300°C. However, this phase diminished when sintered at 1350 °C. The whitlockite was not detected in sample FA20Q throughout the sintering regime. A distinctive peak of wollastonite at $2\theta \sim 30°$ was observed for sample FA5Q when sintered from 1200°C to 1350°C. The presence of wollastonite was noticed for sample FA10Q at all sintering temperatures. The intensity of wollastonite peaks started to decrease in sample FA20Q when sintered from 1000°C to 1100°C, and this phase was not detected when sintered at 1200°C and above. A strong peak of cristobalite at $2\theta \sim 22°$ was detected when the quartz content was increased to 20 wt%. The cristobalite peak intensity decreases when the sintering temperature increases from 1000°C to 1350°C. The formation of dicalcium silicate (JCPDS No. 20-0237) in this composite can be associated with the reaction between wollastonite ($CaSiO_3$) and CaO when sintered at high temperatures above 1200°C based on the reaction given in Eq. (4) [13].

$$CaSiO_3 + CaO \rightarrow Ca_2SiO_4 \qquad (4)$$

I.5.2. FTIR analysis of samples after sintering

The FTIR spectra for the composites sintered at 1000°C, 1300 °C, and 1350°C are shown in Figs. III.10 (a–d). Regardless of quartz content, the absorption bands at 1098 and 1038 cm^{-1} corresponding to the v_3 antisymmetric vibration (stretching) mode of PO_4^{3-} group of FAp were present. Other bands corresponding to v_1 and v_4 vibration modes of PO_4^{3-} were observed at 962, 604, and 574 cm^{-1}. However, the characteristic bands of carbonate at 870, 1424, and 1457 cm^{-1} (initially observed in Fig. III.7) disappeared after sintering up to 1350 °C. The bands detected between 430 and 600 cm^{-1}, with a sharp peak around 520 cm^{-1}, are attributed to the bending vibrations generated by the Si–O–Si group [14]. The bands existing at around 930 and 475 cm^{-1} are associated with the symmetric stretching mode of the SiO_4^{4-} group [15, 16].

These bands' appearance can be due to the formation of calcium silicate phases, such as wollastonite and dicalcium silicate, during sintering.

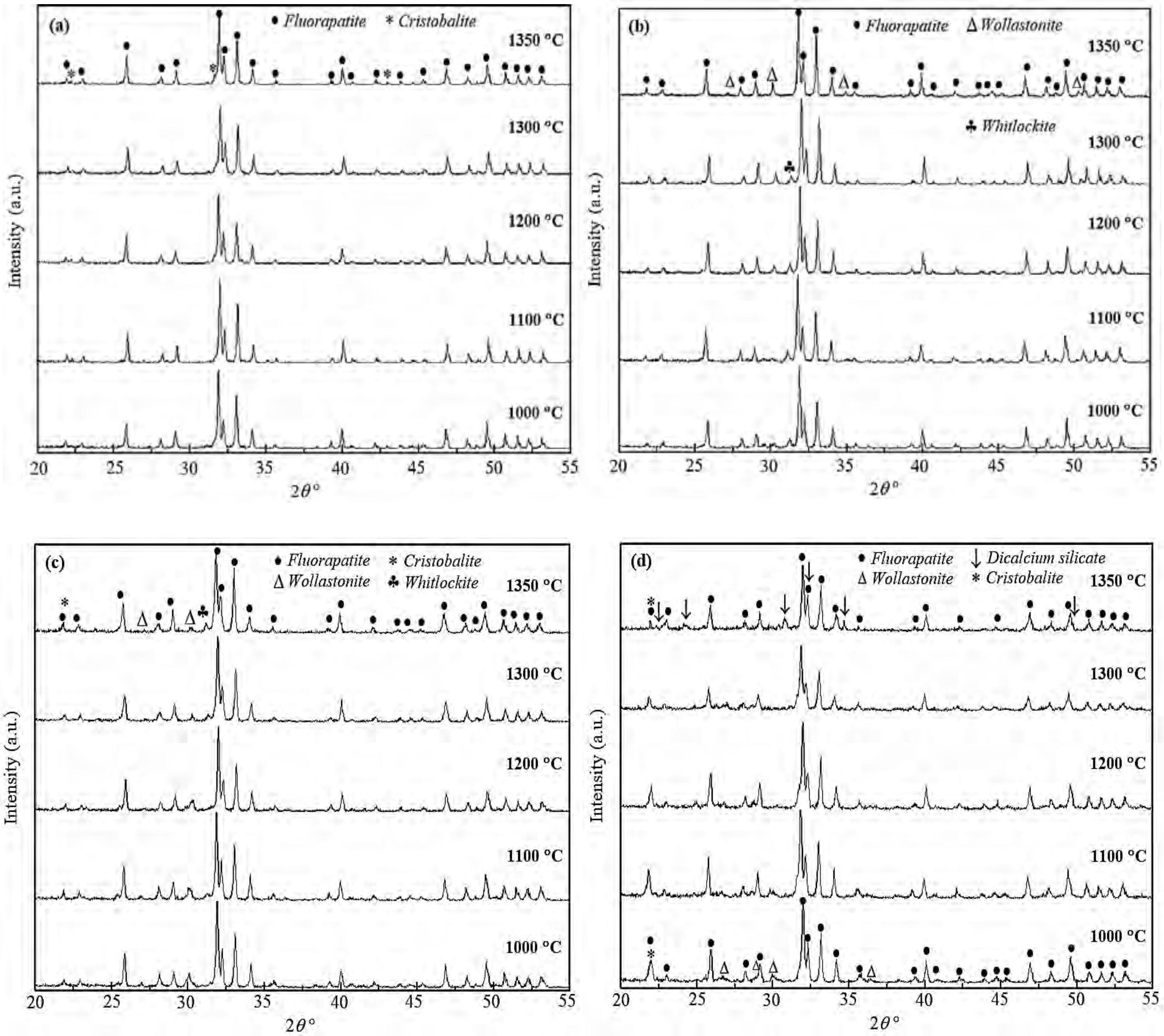

Fig. III.9: XRD patterns for the various fluorapatite composites sintered at various temperatures: (a) FA2.5Q, (b) FA5Q, (c) FA10Q and (d) FA20Q.

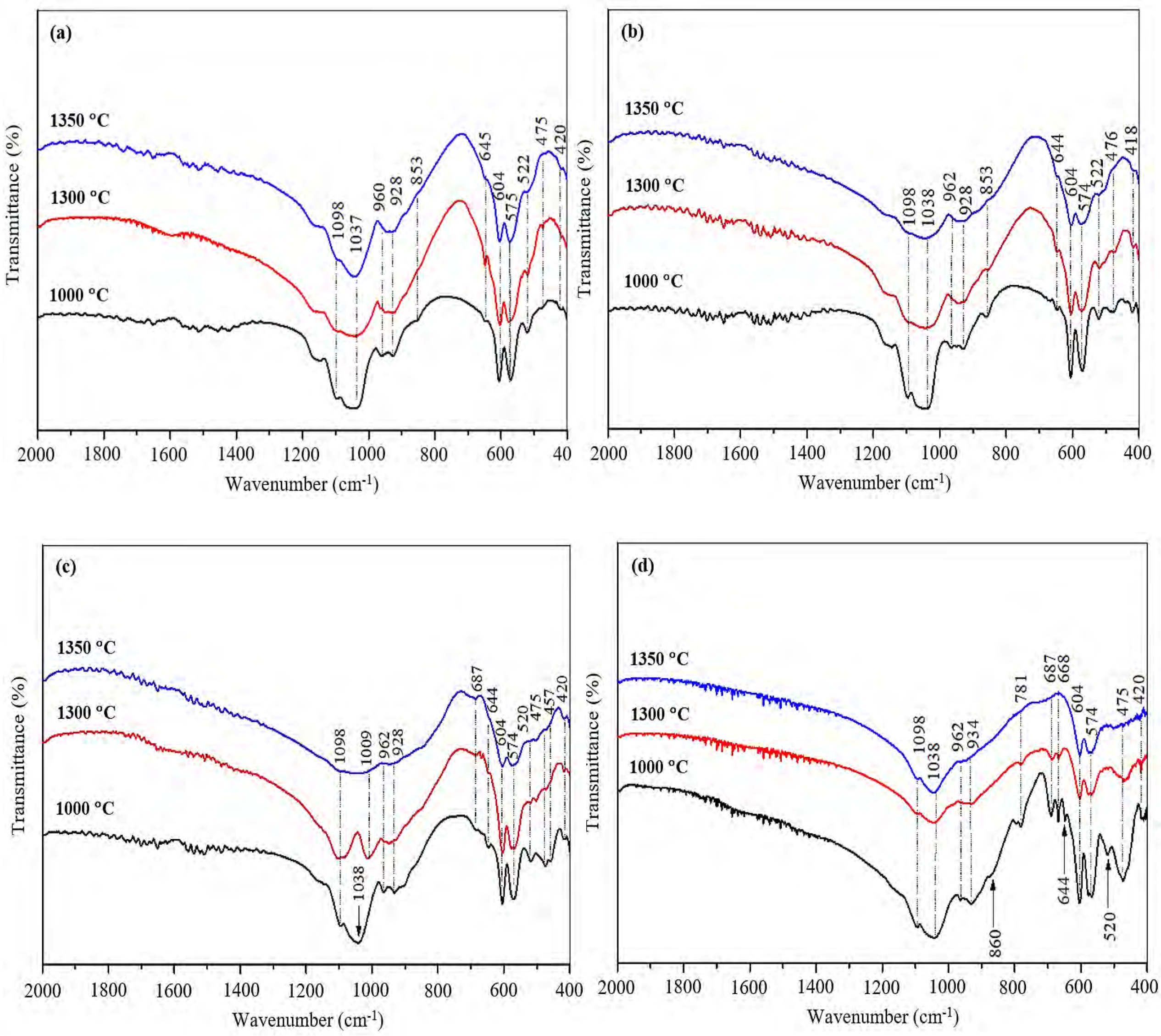

Fig. III.10 : FTIR analysis of composites sintered at various temperatures (a) FA2.5Q, (b) FA5Q, (c) FA10Q and (d) FA20Q.

I.5.3. Measurement of bulk density and open porosity of sintered samples

The variation in open porosity/bulk density of samples with different quartz contents sintered at various temperatures is shown in Fig. III.11. According to the curves plotted in fig. III.11.a, between 1000 °C and 1100°C, all mixtures show an increase in open porosity, and its curves have the same shape. Besides, this variation of open porosity is followed by a significant increase in density in this range of sintering temperature. By combining XRD patterns, practically there are no changes in crystalline phases in the same temperature range, which means that the increase in bulk density is related directly and mainly to the reduction of open porosity rate.

However, the open porosity curves slopes become smaller with the increase of quartz in initial mixtures. The increase of quartz content in the mixtures leads to the precipitation of additional amounts of cristobalite due to the allotropic transformation of the quartz to cristobalite at high temperatures [17]. This last phase will lead to the formation of a liquid phase of high viscosity, which will make the densification more and more difficult [7, 18, 19].

With the increase in sintering temperature above 1100°C, the sample with a low SiO_2 content shows a slight decrease in open porosity of about 1% at 1150°C. It rises to 5% at 1200°C to resume this descent and reach the minimum value of around 0.5% open porosity at 1300°C. This evolution is accompanied by a significant decrease in bulk density, from 3g.cm^{-3} to 2.59 g.cm^{-3}, between 1100°C and 1250°C, and then it stabilizes at around 2.58 g.cm^{-3}. Seeing that there is no change in the crystalline phases, the small variation in open porosity compared to the high decrease in apparent density of the PH2,5Q samples is may be due to the increase in closed porosity in size and/or in number due to the expansion of the trapped gases inside the closed pores [16].

Concerning the samples from mixtures PH5Q, It can be seen that the open porosity remains practically constant between 1100°C and 1250°C at about 6.7%. With the increasing of the sintering temperature, the open porosity increase dramatically to reach 20% at 1350 °C. On the outer side, the bulk density at the same sintering temperature range shows an exponential decrease from about 2.63 g.cm^{-3} to 1.96 g.cm^{-3} between 1100 °C and 1250 °C, followed by a small fluctuation between 1.95 g.cm^{-3} and 2.05 g.cm^{-3} at the higher sintering temperatures. The anomalies variation of bulk density between 1100 °C and 1250 °C perhaps due to the bloating which engenders the increase of pores size and number [16, 18], whereas the evolution of open porosity above 1250 °C maybe the result of the interconnection of the surface pores and the close pores which are very near to the surface of samples.

In the case of the sample with a high amount of silica, namely PH10Q and PH20Q, both samples show a decrease in the open porosity when the sintering temperature is raised from 1100 °C to 1150 °C, but the variation of porosity in the case of PH10Q is seven times slower than in the case of PH20Q. Moreover, in the opposite of the sample PH10Q that demonstrates a significant reduction in bulk density compared to the variation in open porosity, the sample PH20Q shows an increase in bulk density. Consequently, this reduction in density in the case of PH10Q is the results of bloating [18], whereas the raising in bulk density of sample PH20Q perhaps because the reduction in open porosity is more intense and has a more powerful impact than bloating due to trapped gases, which are two antagonistic phenomena in terms of densification. By the increase of sintering temperature until 1250°C, both samples show the same variation direction and practically with the same rhythm when the open porosity increases and bulk density decreases.

During the last sintering range between 1250 °C and 1350 °C and in the case of mixture PH10Q, the open porosity fluctuates in the range between 20% and 22.5%, whereas it decreases from 18.6% to 11.3% in the case of mixture PH20Q.

Besides, there is a correlation between the open porosity and bulk density in terms of speed of variation, between 1150 °C and 1350 °C, which means that this variation in bulk density is related, directly and mainly, to the variation in open porosity.

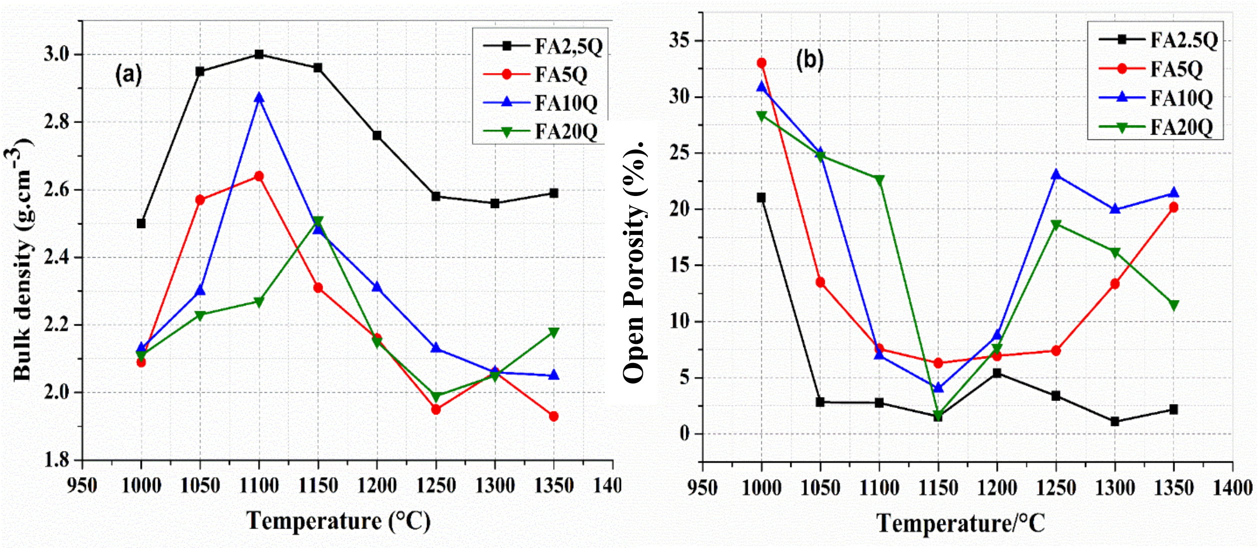

Fig. III.11: Effect of sintering temperatures on the bulk density of fluorapatite composites.

I.5.4. Micro-hardness measurement of sintered samples

The variation of the Vickers microhardness of sintered samples, for mixtures with the lowest and highest quartz content, as a function of sintering temperature, between 1100 °C and 1350 °C are presented in Fig III.12.

According to this figure, the hardness value is almost the same for both samples sintered at 1100 °C, at 4.4 GPa. However, as the sintering temperature increases up to 1250 °C, the mixture's hardness with 20% SiO_2 becomes greater than that of the mixture with 2.5% SiO_2, and the difference in hardness between the two samples increases.

At higher sintering temperatures, the sample with 2.5% SiO2 shows a constant and monotonous decrease in microhardness. However, the sample with 20% shows a decrease from 6.4 GPa to 5.73 GPa as the temperature rises from 1250 °C to 1300 °C, and then the hardness shows a jump from 5.73 GPa to 7.1 GPa as the temperature rises from 1300 °C to 1350 °C. This last increase in hardness is due to the formation of the new C2S phase, which is known for its high hardness [20].

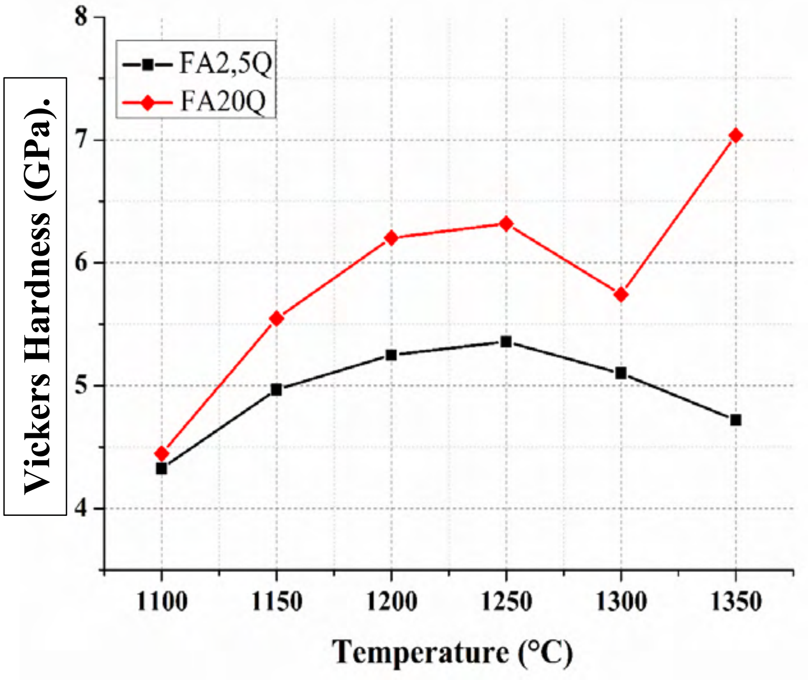

Fig III.12: Microhardness (HV) curves of FA2.5Q and FA20Q samples as a function of sintering temperature.

I.5.5. Morphological analysis by FESEM micrographic observation

The FESEM images of composites sintered at 1000 °C and 1350 °C are shown in Figs .III.13 and 14, respectively. The morphology of composites evolved from rod-like structure to equiaxed grain morphology when the sintering temperatures increased from 1100 °C to 1350 °C. The composites with high quartz content (i.e., 10 wt% and 20 wt%) and when sintered at 1350 °C exhibited a wetted and smooth appearance of rounded grains. This condition is believed to be due to the excessive liquid phase present during sintering and rapidly cooled to room temperature (Fig. III.14d). The SEM analysis of samples sintered at low temperature (Fig. III.13) revealed a less dense structure, as clearly shown in the inset picture. This condition is in good agreement with the density measurement. However, as the sintering temperature was increased, this was accompanied by a denser microstructure, as shown in Fig. III.14.

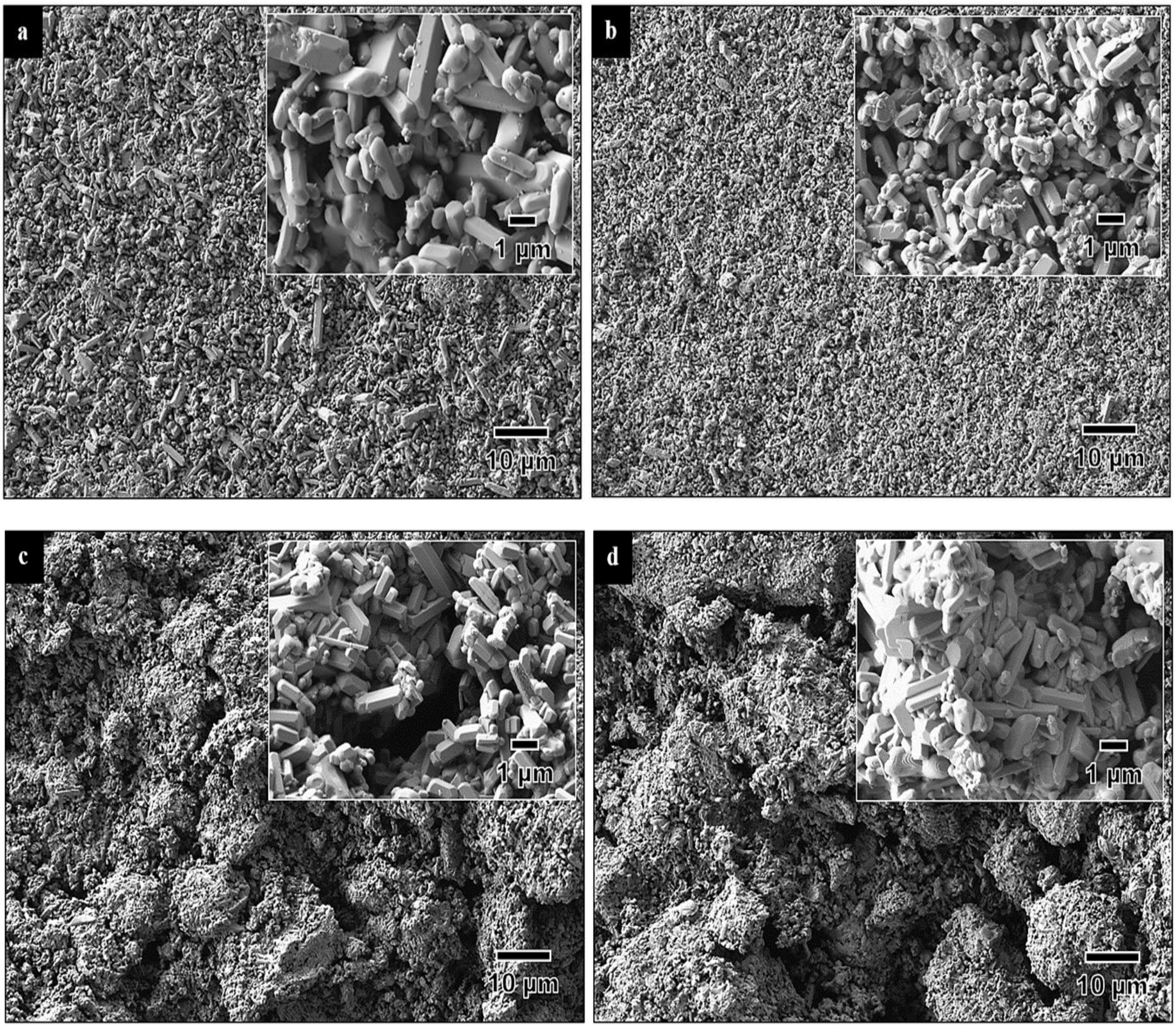

Fig. III.13: SEM pictures of composites sintered at 1100°C: (a) FA2.5Q, (b) FA5Q, (c) FA10Q and (d) FA20Q.

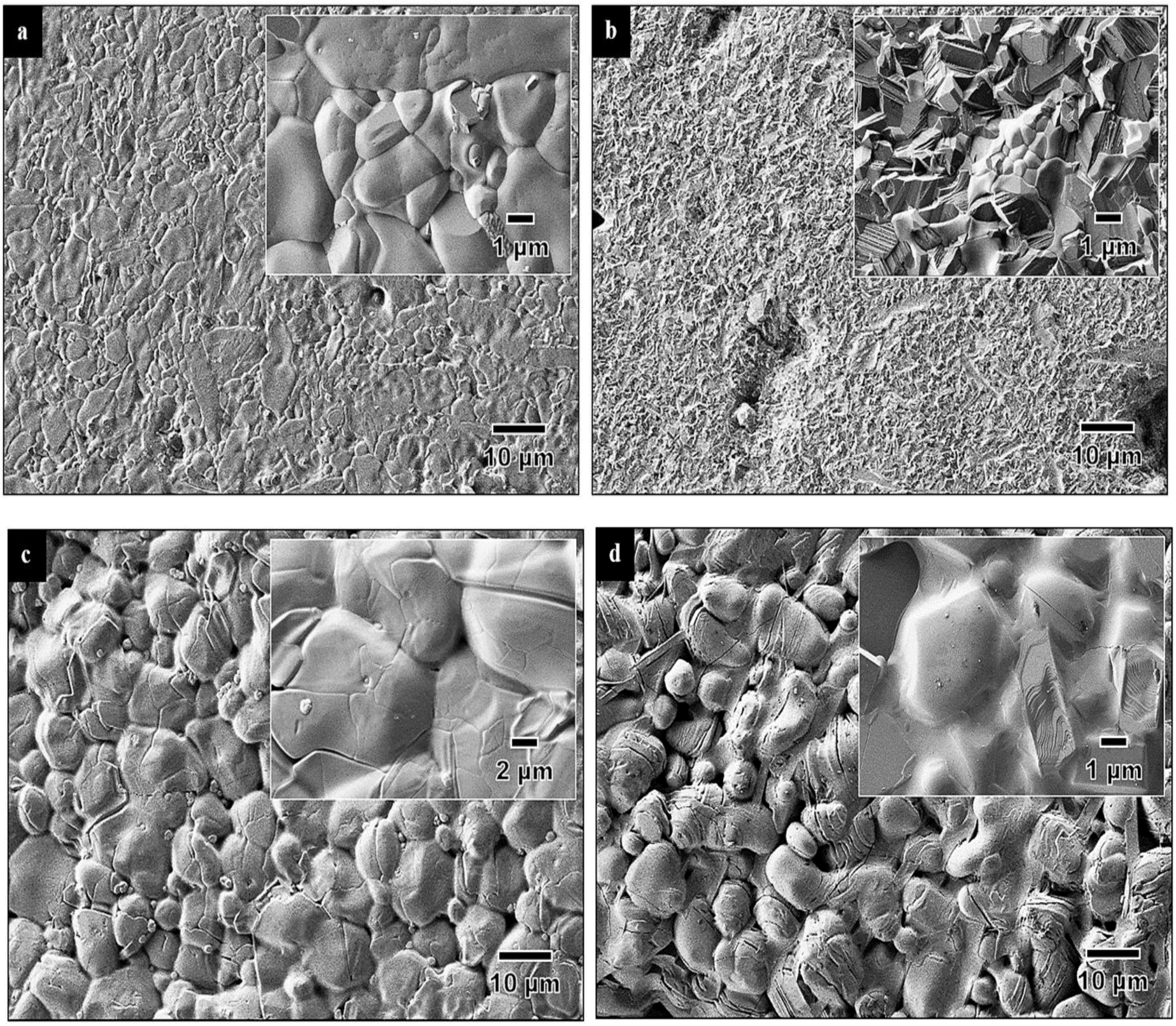

Fig. III.14: Comparison of the SEM pictures of composites sintered at 1350°C: (a) FA2.5Q, (b) FA5Q, (c) FA10Q. and (d) FA20Q.

I.5.6. FESEM observations and EDX analyses after immersion in SBF

Micrographs of the surface of the samples after immersion in the SBF solution for 1, 3, and 16 weeks are presented in Fig III.15 and 16.

After immersion of the FA2,5Q samples, which was treated at 1100°C in SBF for several periods, we observe the presence of a uniform layer of spherical particles linked together and constituting a network of small crystallites after only one week of immersion (Fig I.15). This morphology is characteristic of that of a nanocrystalline apatite similar to the bone mineral. The longer the immersion time in SBF, the higher the process, and the more clearly the apatite emerges.

While the FA2.5Q samples after different immersion times in SBF, 1 and 3 weeks and processed at 1350°C, we observe a slight surface modification (Slight formation of apatite "This can be traced to the emergence of the cristoballite phase"). However, after 16 weeks of immersion in SBF, the surface is covered by apatite crystals forming a phosphocalcic layer.

The observations on the surface of the FA20Q samples, which were treated at 1100 and 1350°C (Fig III.16), after 1 week of immersion, a layer of apatite starts to form from spherical particles in all the samples. The coating is homogeneous over the whole surface after 16 weeks of immersion in SBF. Cracks and fissures, which probably occur during the drying of the samples when they leave the bath, can be observed. These cracks become wider as the immersion time increases, which could also be indicative of the formation and thickening of a neoformed layer. "This can be traced to the emergence of phases such as wollastonite and dicalcium silicate (known for its bioactivity " See last part of chapter 1"), and that by increasing the quartz content.

Quantitative and qualitative EDX analysis was carried out on the surface of the samples after their immersion in the SBF solution for 16 weeks. The values obtained are detailed in fig III.17 and 18. The formation of carbonated hydroxyapatite confirmed the FESEM results.

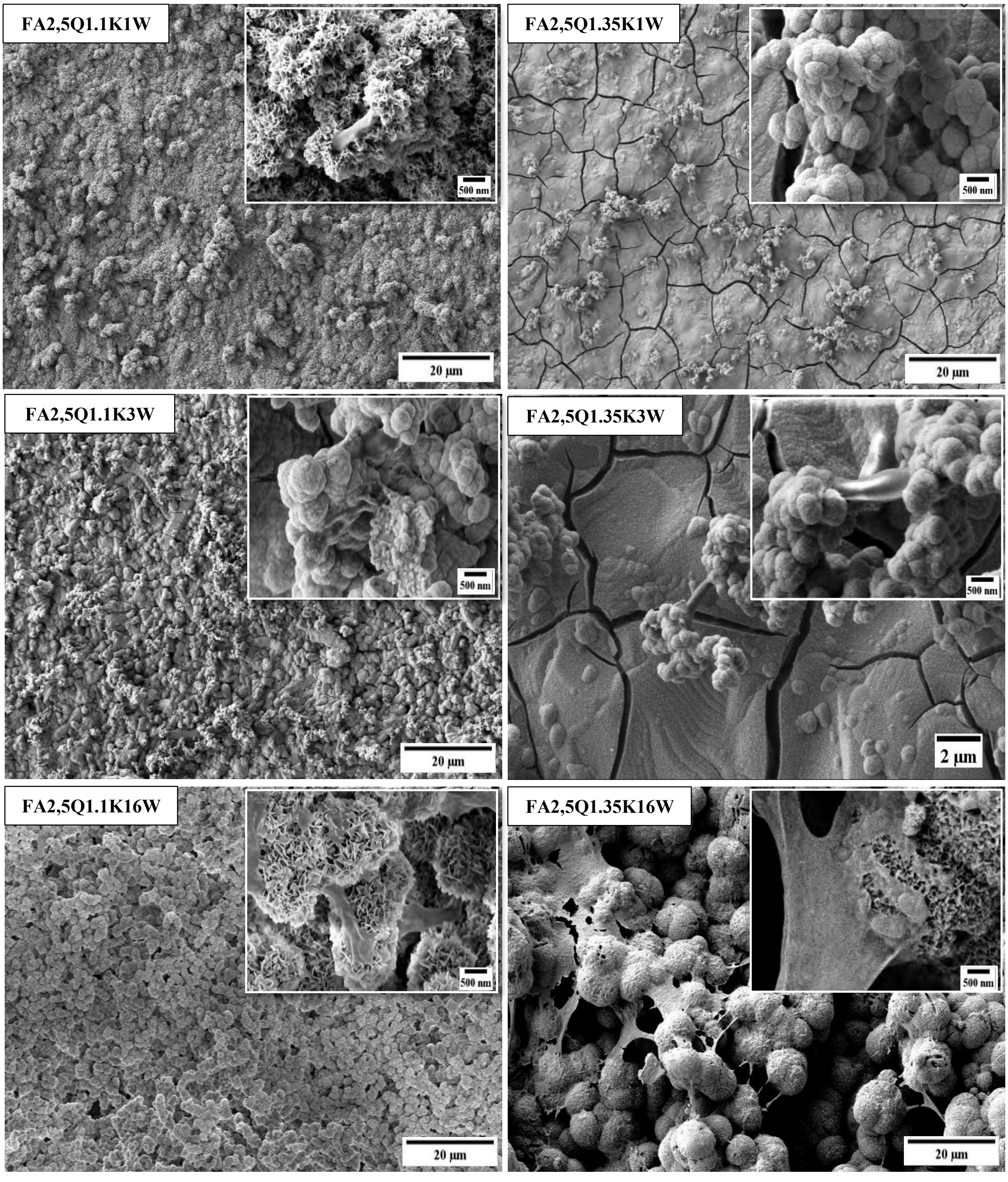

Fig III.15: FESEM observations of the surface of sample **FA2.5Q** at different immersion periods in SBF(1W, 3W and 16W: W:Week) at 1100 and 1350°C:(1.1k and 1.35K).

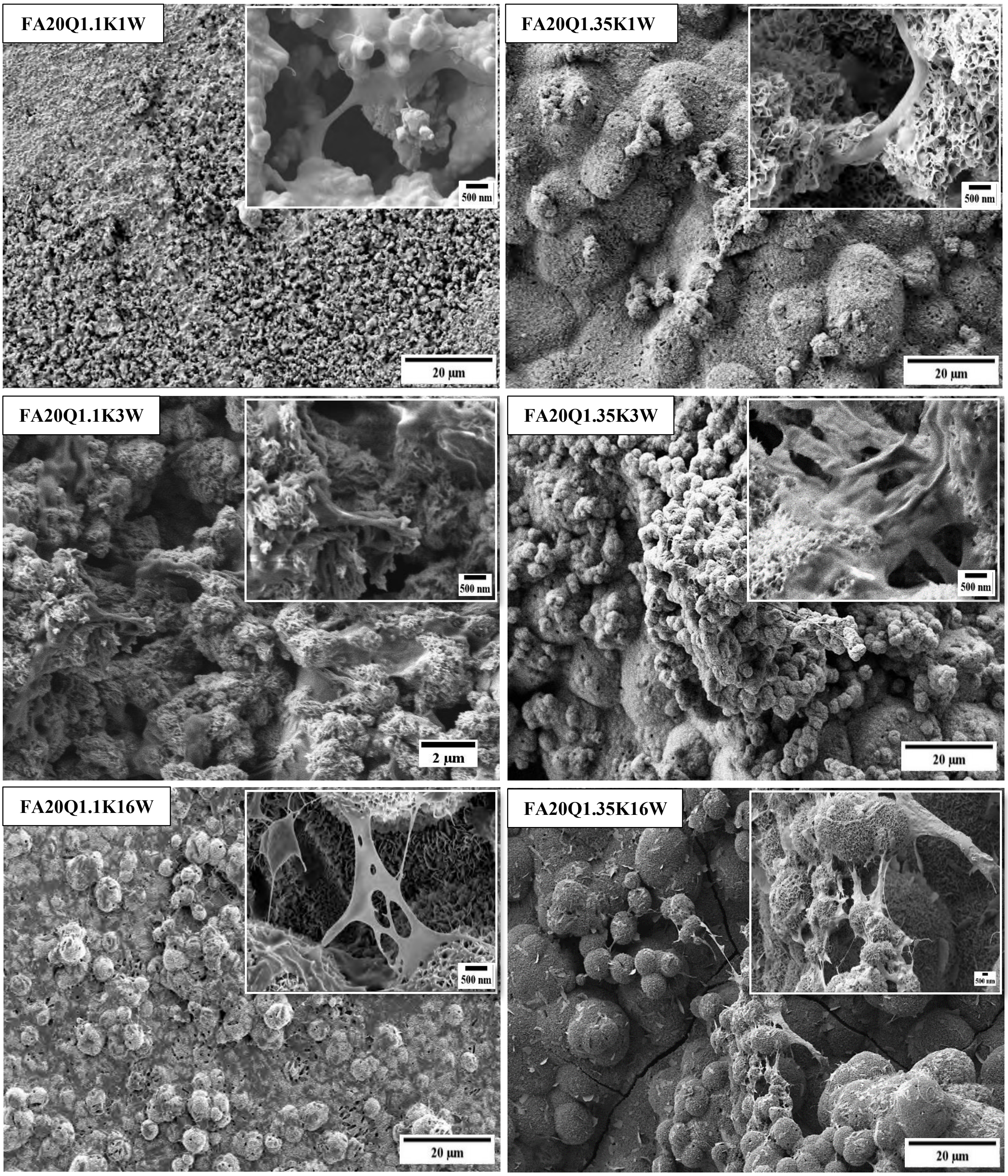

Fig III.16: FESEM observations of the surface of sample **FA20Q** at different immersion periods in SBF(1W, 3W and 16W: W:Week) at 1100 and 1350°C:(1.1k and 1.35K).

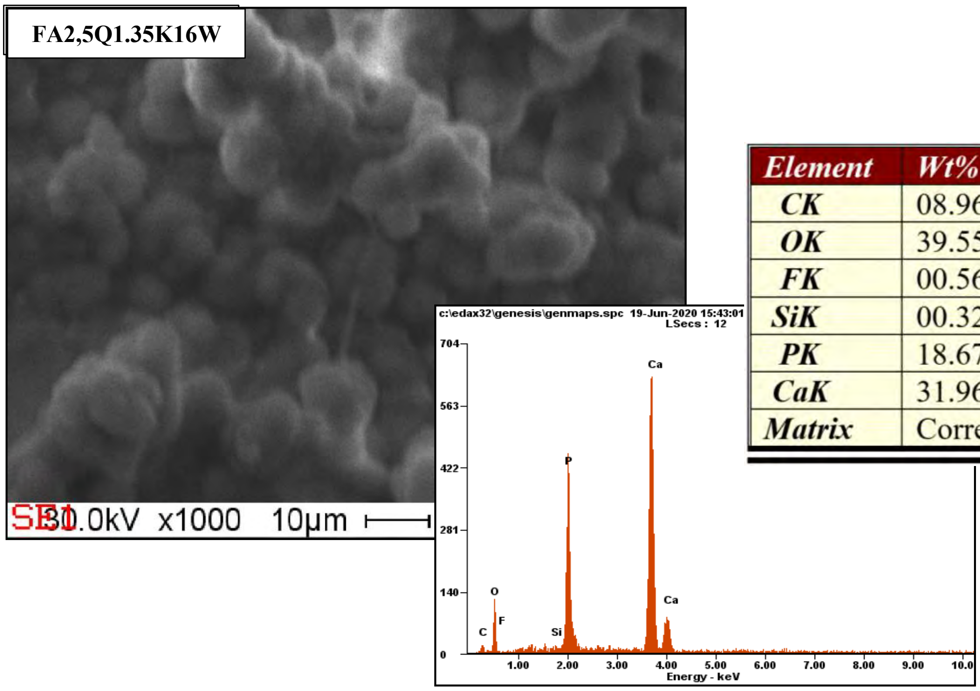

Element	Wt%	At%
CK	08.96	16.01
OK	39.55	53.07
FK	00.56	00.63
SiK	00.32	00.24
PK	18.67	12.94
CaK	31.96	17.12
Matrix	Correction	ZAF

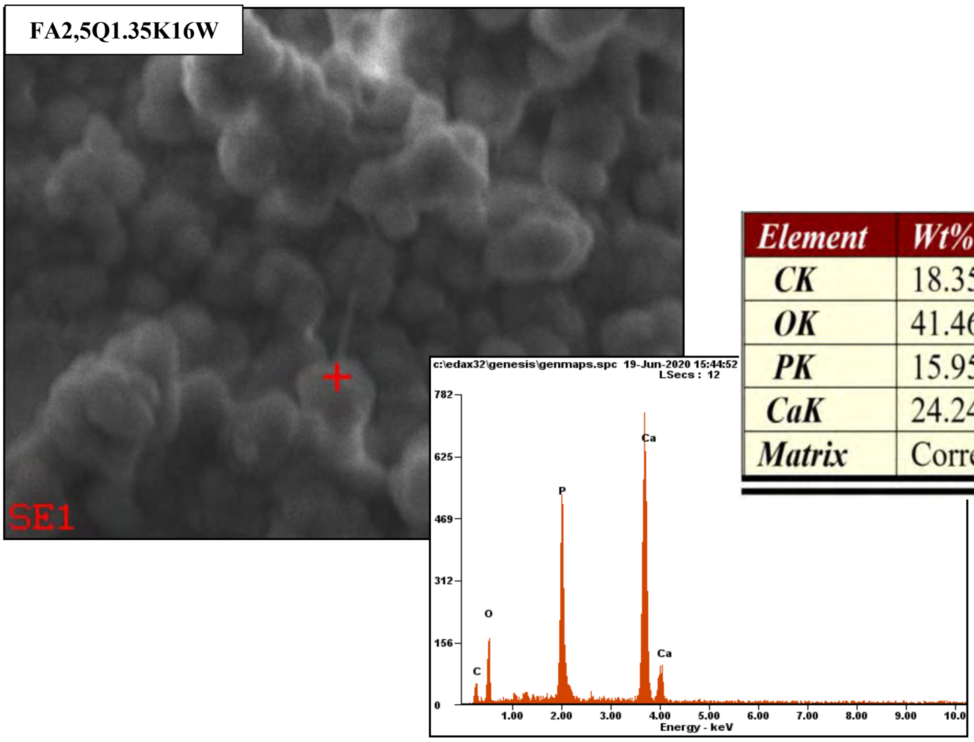

Element	Wt%	At%
CK	18.35	29.16
OK	41.46	49.47
PK	15.95	09.83
CaK	24.24	11.54
Matrix	Correction	ZAF

Fig III.17: EDX analyses of the surface of **FA2.5Q** samples after 16 weeks of immersion in SBF.

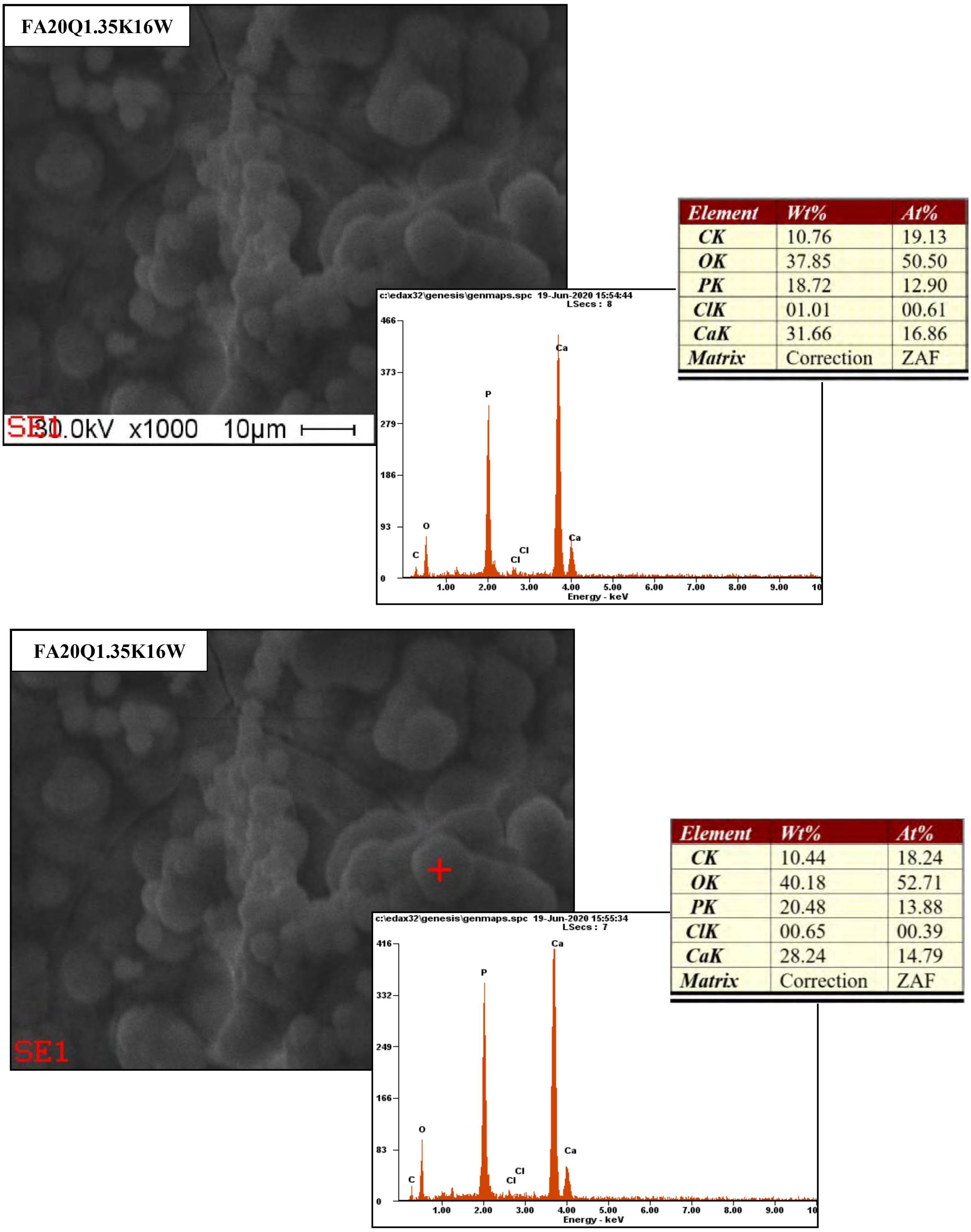

Element	*Wt%*	*At%*
CK	10.76	19.13
OK	37.85	50.50
PK	18.72	12.90
ClK	01.01	00.61
CaK	31.66	16.86
Matrix	Correction	ZAF

Element	*Wt%*	*At%*
CK	10.44	18.24
OK	40.18	52.71
PK	20.48	13.88
ClK	00.65	00.39
CaK	28.24	14.79
Matrix	Correction	ZAF

Fig III.18: EDX analyses of the surface of **FA20Q** samples after 16 weeks of immersion in SBF.

Part II: *Sintering behavior of alumina-fluorapatite composite produced from pure alumina and natural phosphate with TiO2 addition.*

In the current part, the alumina-fluorapatite-based composites were prepared from natural phosphate and pure laboratory alumina. Thus, this study investigates the effect of titania addition up to 10wt% on the Physico-chemical proprieties of the composite.

II.1. Physicochemical and morphological analyses of the initial materials

II.1.1. Chemical analysis of natural phosphate and quartz

The chemical composition of the natural phosphate determined by the XRF method is presented in Table III.2. The findings showed that primarily calcium oxide (CaO) and Pentoxide diphosphorus (P_2O_5) were the principal components of the natural phosphate used in this study. The XRD pattern of the raw phosphate (Fig. III.19.a) and titanium (Fig. III.19.b) oxide powders showed that fluorapatite (ICDD#015-0876) and francolite (ICDD#002-0833) are the main mineral components. At the same time, dolomite represents the minor phase of the natural phosphate powder, as shown in Fig. III.19.a, while the anatase (ICDD#01-084-1286) was the major phase of the titanium oxide (Fig. III.19.b).

Table III.2: Chemical composition (Wt%) of FAp (natural phosphate) and quartz in mass%

Elements	**F**	**Na_2O**	**MgO**	**Al_2O_3**	**SiO_2**	**P_2O_5**	**SO_3**
N-P	3.65	1.13	0.89	0.87	1.79	28.2	2.55

K_2O	**CaO**	**Fe_2O_3**	**ZnO**	**SrO**	**Y_2O_3**	**L.O.I.**
0.138	59.9	0.455	0.038	0.345	0.044	/

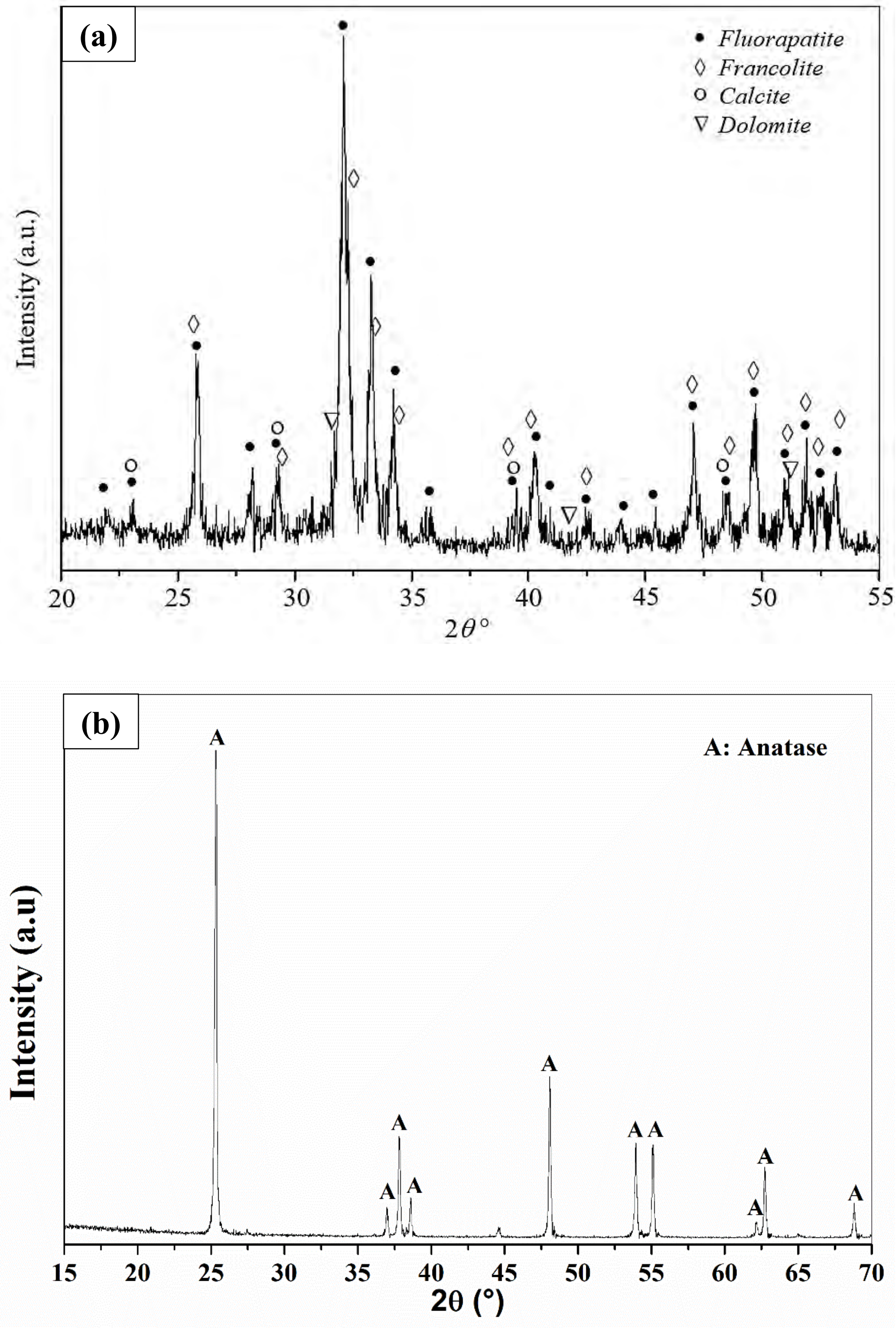

Fig. III.19: X-ray diffraction spectrum of (a) natural phosphate powder (b) titanium oxide powder.

II.2. Analysis of shaped and sintered samples

II.2.1. X-ray analysis of samples after sintering

The XRD patterns of the sintered samples when sintered between 1000 to 1600 are shown in Fig.III.20. The diffraction peaks observed for samples that do not contain titanium oxide (PHA0T) when sintered at 1000°Care referred to calcium aluminate (calcium aluminate, ICDD # 1.70.134, $CaAl_2O_4$) phases. Both phases of alumina (Corundum, ICDD # 05-0712) and fluorapatite (FA, ICDD # 015-0876) appeared. By increasing the sintering temperature to 1400 °C, it noticed the disappearance of the calcium aluminate phase and the emergence of new diffraction peaks due to the hibonite phase (Hibonite, CA6, ICDD # 038-0470), which is formed according to the following chemical reaction equations[21-23]:

- $Al_2O_3 + CaO \longrightarrow CaAl_2O_4$ (CA) (1)
- $CA + Al_2O_3 \longrightarrow CaAl_4O_7$)CA_2((2)
- $CA + 5Al_2O_3 \longrightarrow CaAl_{12}O_{19}$)CA_6((3)
- $CA_2 + 4Al_2O_3 \longrightarrow CaAl_{12}O_{19}$)CA_6((4)

It also noted the emergence of diffraction peaks due to (α-TCP, ICDD # 09-0348) α-TCP resulting from partial dissociation of fluorapatite. With an increase in the sintering temperature to 1500 °C and 1600 °C, it observed a significant α-TCP phase formation (total dissociation of fluorapatite) and an increase in the intensity of the diffraction peaks of the hibonite phase with the alumina phase remaining essential.

For the (PHA1T) sample (Fig.III.21), the diffraction peaks at 1000 °C were shown due to the phases of Alumine Titanium Oxide, #PDF: 39-052, Al_2-Ti_7O_{15}, alumina, and fluorapatite. At a temperature of 1200°C, the formation of the calcium aluminate phase and the disappearance of the aluminate titanate phase and oxide were observed, while the diffraction peaks of fluorapatite and alumina remained. By increasing the sintering temperature to 1400 °C, it notices the emergence of diffraction peaks due to the phases of fluorapatite, hibonite, and alumina, and it also notices the emergence of diffraction peaks due to α-TCP resulting from partial dissociation of fluorapatite and the disappearance of the calcium aluminate phase. At a sintering temperature of 1600 °C, increased diffraction peaks of the α-TCP phase can be observed due to the total dissociation of fluorapatite with the remaining alumina and hibonite phases. The same phase transitions can also be observed in both PHA3T and PHA5T samples (Fig.III.21), with little change in the hibonite phase intensity of the PHA5T samples at 1600 °C.

By looking at the samples containing 10 Wt% of titanium oxide addition (PHA10T), the diffraction peaks can be observed due to the phases of alumina, fluorapatite, and alumina titanate oxide, which increased in intensity with increasing the percentage of addition and both anatase (Anatase, #PDF: 96- 500-224), and rutile (Rutile, #PDF: 1-86-147) when sintered at 1000 °C (Fig.III.22). With increasing the sintering temperature to 1400 °C, diffraction peaks of the following phases appeared: fluorapatite, hibonite, alumina titanate oxide, rutile, and α-TCP. At 1600 °C, diffraction peaks are observed for the phase of alumina, hibonite, α-TCP, and rutile.

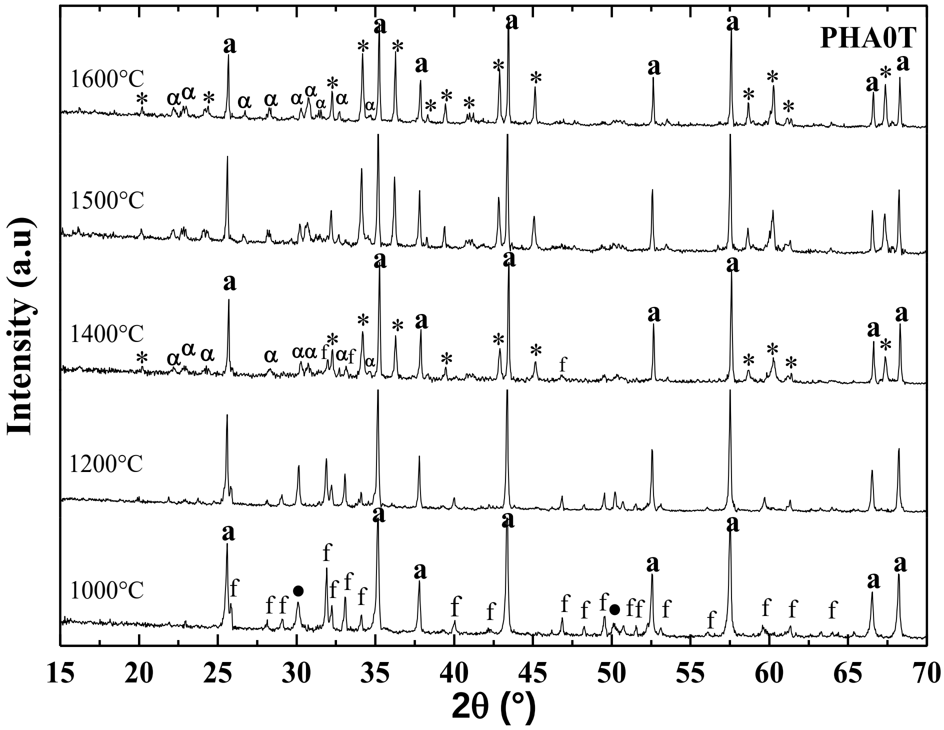

Fig.III.20 (PHA0T) : XRD spectrum of the samples with 0 W.% of TiO2, and sintered at various temperatures (f: Fluoroapatite, a: Alumine, •: calcium Aluminate,

*: Hibonite (CA6), α: α-TCP.

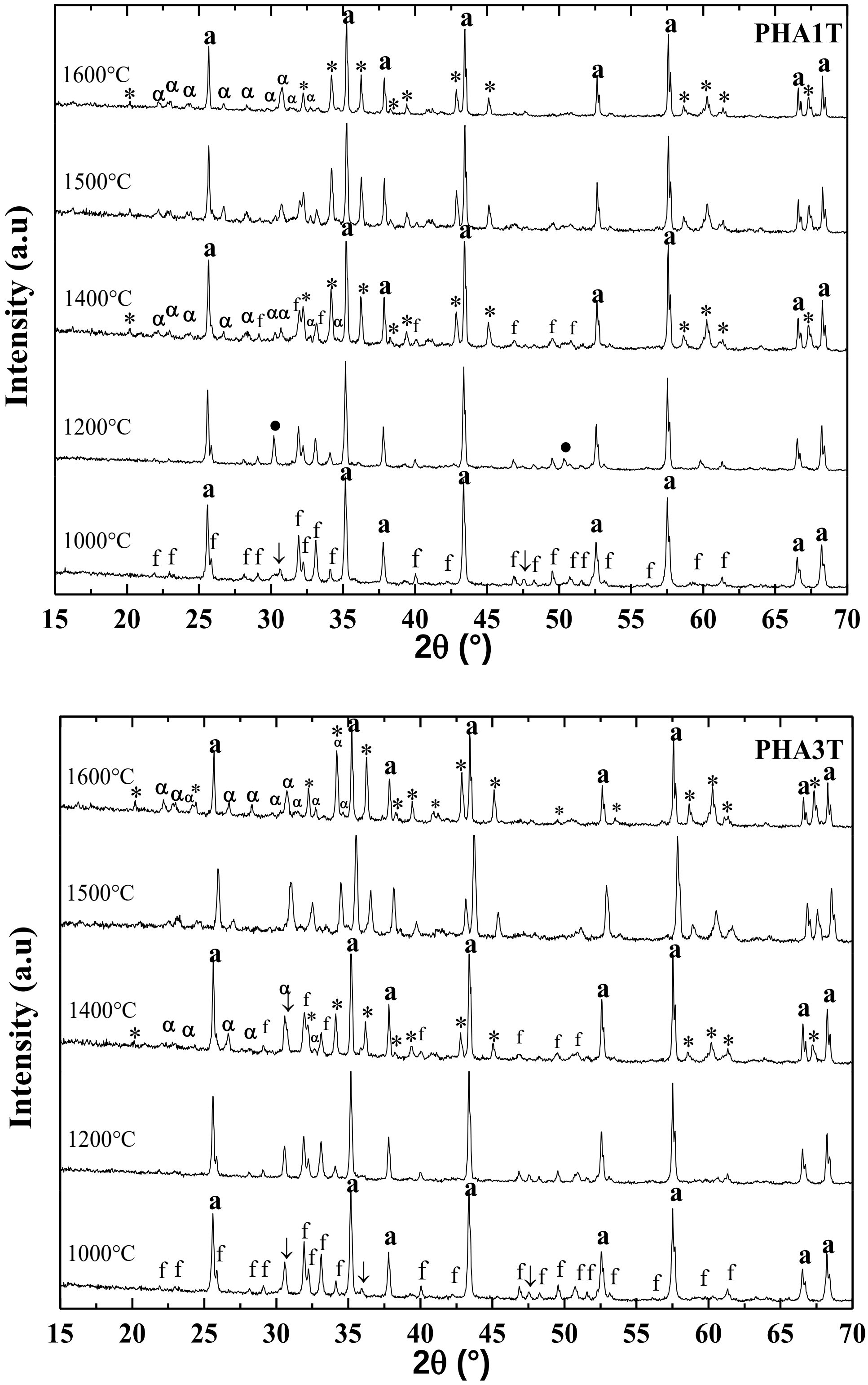

Fig.III.21 (PHA1T and PHA3T) : XRD spectrum of the samples1and 3W.% of TiO2 respectively, and sintered at various temperatures (f: Fluoroapatite, a: Alumine, •: Aluminate de calcium, *: Hibonite (CA$_6$(, α: α-TCP. ↓: Alumin Titanium Oxid Al$_2$-Ti$_7$O$_{15}$.

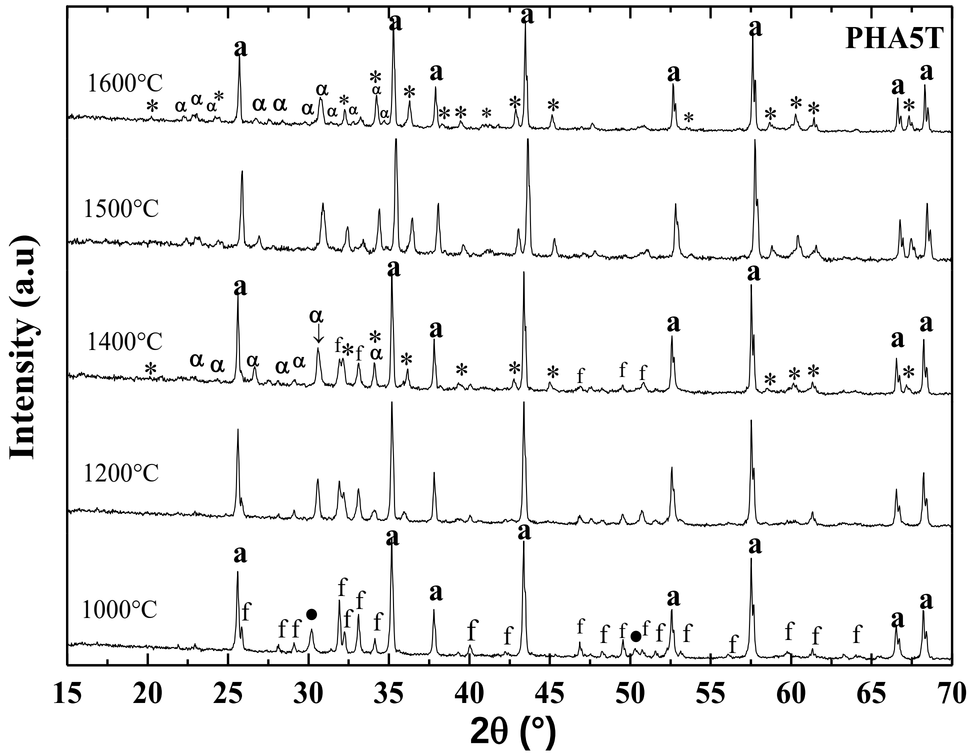

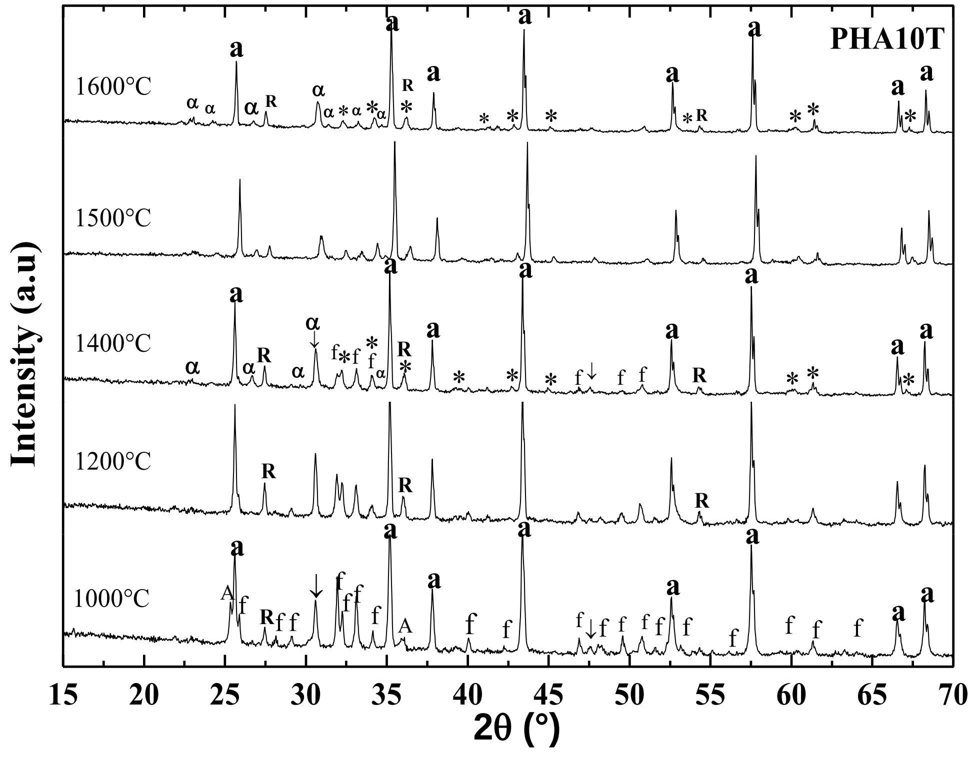

Fig.III.22 (PHA5T and PHA10T): XRD spectrum of the samples with 5 and 10 W.% of TiO2 respectively, and sintered at various temperatures (f: Fluoroapatite, a: Alumine, .: Aluminate de calcium, *: Hibonite (CA6), α: α-TCP, ↓: Alumin Titanium Oxid, A: Anatase, R: Rutile).

II.2.2. Measurement of bulk density, open porosity, and linear shrinkage of sintered samples

- **linear shrinkage of sintered samples**

Fig.III.23 represents the variation of the shrinkage of sintered samples PHA0T, PHA1T, PHA3T, PHA5T, and PHA10T as a function of temperature.

At sintering temperature between 1000 to 1200°C: it can be observed that there is a constant increase in the shrinkage rate for the two samples, PHA0T and PHA1T, with a slight increase for the two samples PHA3T and PHA10T. At sintering temperature ranging from 1200 to 1500 °C, it can be seen that there is a significant increase in the shrinkage rate for all samples, reaching 16.69% for the PHA0T sample and 22.38% for the PHA10T sample, due to the occurrence of different phenomena simultaneously, including the release of different gases from natural phosphate (SO_3, CO_2 ...), the interaction between the basic components of alumina and natural phosphate [24], as well as the excellent effect of processing temperature and addition of titanium oxide [25], which helped in the good sintering process of the alumina-fluorapatite composite. With increasing the temperature to 1600 ° C, an almost constant shrinkage rate was recorded for all samples, indicating the sintering process's completion. As for the sample PHA5T, a linear increase in shrinkage rate was recorded when sintered from 1000 to 1500 °C and reached a target of 18.76%. As for the sample PHA5T, a linear increase in contraction rate was recorded at the thermal field from 1000 to 1500 ° C, reaching a target of 18.76%. Then, the approximate stability of this sample was observed in the range 1500 to 1600 °C, possibly due to sintering.

It can be said that the addition of titanium oxide has significantly contributed to the sintering process as the shrinkage rate increases with the increase of titanium oxide content, where the shrinkage percentage is large in the sample that contains high titanium oxide ratios (10wt%), as the largest rate reached about 22.38% at a temperature of 1500 °C, while it is relatively low in samples that contain low levels of titanium oxide 0 and 1wt%.

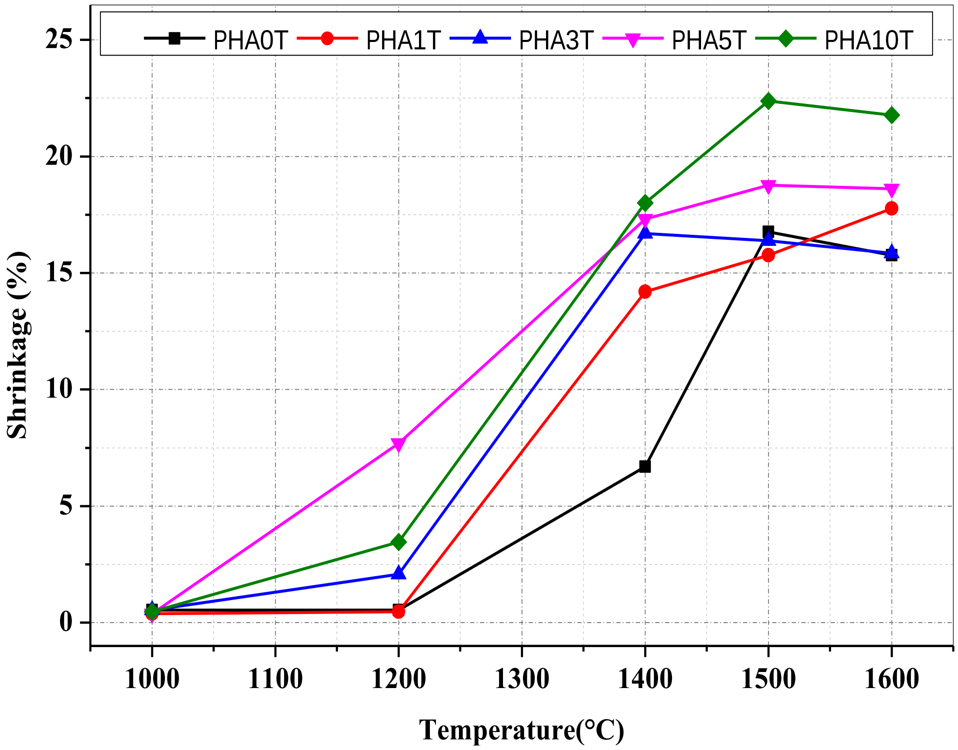

Fig.III.23: Shrinkage of the samples as a function of the temperature.

- **bulk density, open porosity of sintered samples**

Fig.III.24.a represents the change in bulk density as a function of temperature for the alumina-fluorapatite composite samples with and without the addition of TiO_2. It can be said that there is an inverse relationship between the bulk density and the open porosity of the samples with the increase in the sintering temperature, as the higher the bulk density, the lower the porosity. At the sintering temperature of 1000 °C to 1200 °C: the bulk density values appear practically constant for the samples PHA0T and PHA1T. The bulk density increases linearly with an increase in the temperature from 1200 °C to 1500 °C. The PHA0T samples reached their peak when sintered at 1600°C with a recorded value of 3.55 $g.cm^{-3}$. As for the sample PHA1T, a significant increase of bulk density value can be observed from 1200 to 1500 ° C, where it reaches its highest value of 3.56 $g.cm^{-3}$ due to an increase in sintering and a decrease in the open porosity [7, 22], as well as the effective effect of adding titanium oxide[26, 27], as it decreases slightly at 1600 ° C due to re-formation of open porosity.

Regarding the samples (PHA3T, PHA5T, and PHA10T), it can be observed that there is an increase in the bulk density when sintered between 1000 - 1400 °C, where the bulk density at 1400 °C reached its maximum value in both samples PHA3T and PHA5T with a recorded value of about 3.65 $g.cm^{-3}$.

This may be due to the formation of the alumina titanate oxide phase resulting from the interaction of alumina with titanium, shown in the diffraction spectrum of Fig.III.21, which was confirmed by Saka et al. [27]. A slight decrease in the volumetric mass was also observed at sintering temperature of 1500 °C caused by an initial swelling of the samples, followed by another rather large decrease at 1600 °C for both PHA5T and PHA10T samples.

This can be attributed to the relative increase in the open porosity that may have formed from the exit gases resulting from fluorapatite's total dissociation.

The open porosity is one of the most important parameters that must be taken into account in ceramics' characterization [22]. As shown in Fig.III.24b, It can be observed that the percentage of open porosity is practically constant (about 44%) at the sintering temperature range from 1000 to 1200 ° C for samples PHA0T, PHA1T, and PHA3T; Then, it decreases linearly with increasing sintering temperature (1600 °C), reaching very low levels between 0.2 and 1.6%. At the sintering temperature ranging from 1000 to 1400 ° C: It can be seen that there is a gradual and steady decrease in the open porosity ratio for both PHA5T and PHA10T samples from 44% to a minimum value of about 0.1% and 0.6%, respectively when sintered at 1400 °C.

This indicates the positive effect of adding titanium oxide to eliminate open porosity due to the emergence of the alumina titanate oxide phase. In the temperature ranging from 1400 to 1600 °C, a slight increase in the open pore values can be observed, which corresponds to a decrease in the bulk density, possibly due to the large proportions of titanium treated at high temperatures[26].

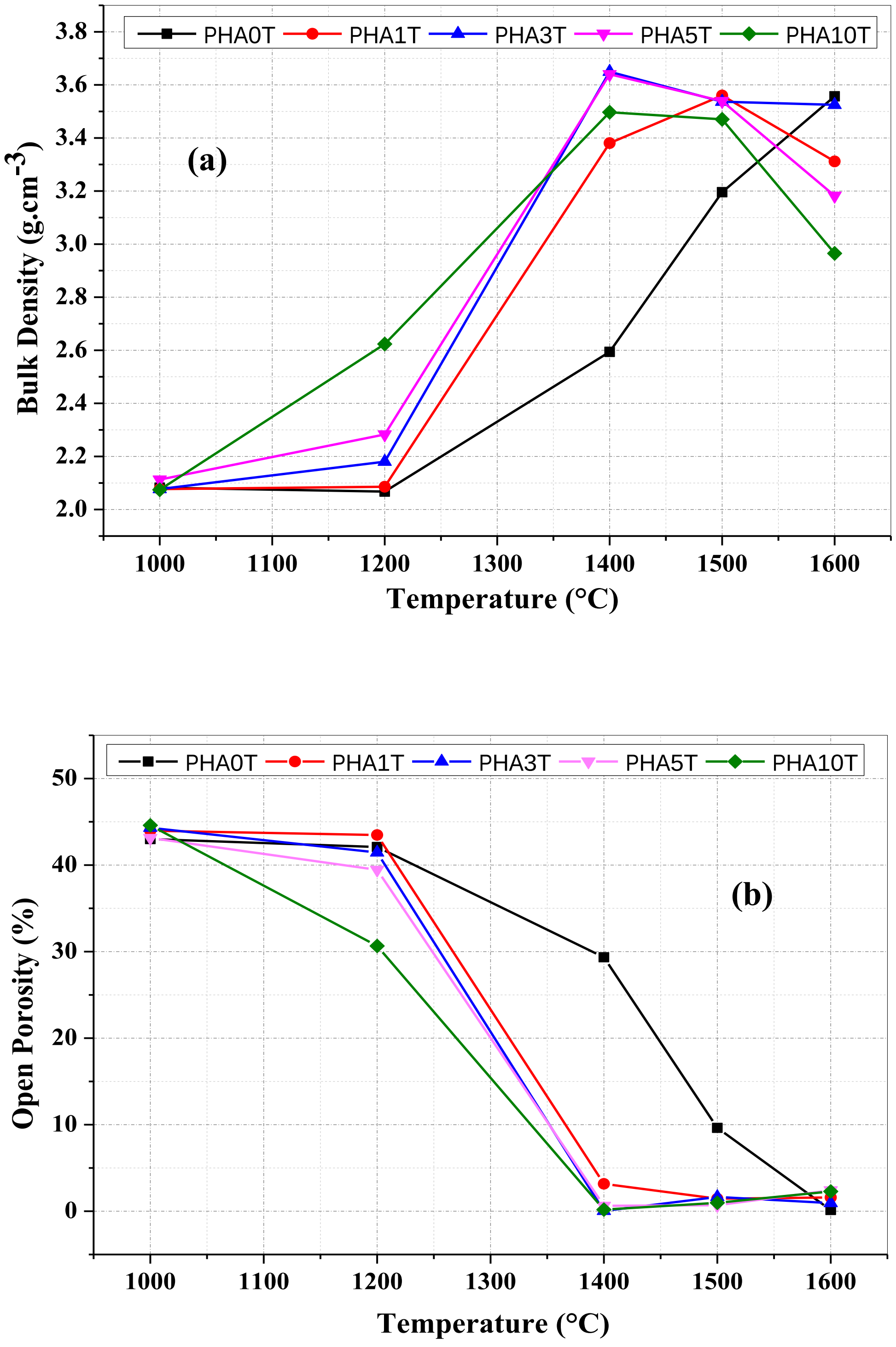

Fig.III.24: Effect of sintering temperatures on (a) the bulk density (b) the open porosity of the alumina-fluorapatite composites.

II.2.3. Vickers hardness of sintered samples

The micro-hardness variations for the alumina-fluorapatite composite samples as a function of titanium oxide addition when sintered at 1400 and 1500°C are represented in Fig.III.25.

It can be seen that the micro-hardness values increased linearly with increasing TiO_2 concentration between 0 Wt% and 5Wt%, where its value reached about 12.85 GPa at 1400° C and about 13.29 GPa at 1500°C for samples containing 5 Wt% TiO_2. It is also noticeable that sintering at higher temperatures enhanced the hardness, reaching a maximum value of 13.65 GPa for samples containing 10 Wt% at a sintering temperature of 1500 °C. The hardness difference in this study could be due to the increase in titanium oxide, which led to the formation of the alumina titanate oxide phase[27, 28] as indicated in the XRD; likewise, the appearance of the CA_6 phase increased [22], which led to increased condensation and micro-hardness. While the hardness value decreases for the sample containing 10 Wt% when sintered at 1400°C to a value of 10.6 GPa, this can be attributed to the decrease in the phase ratio of CA_6.

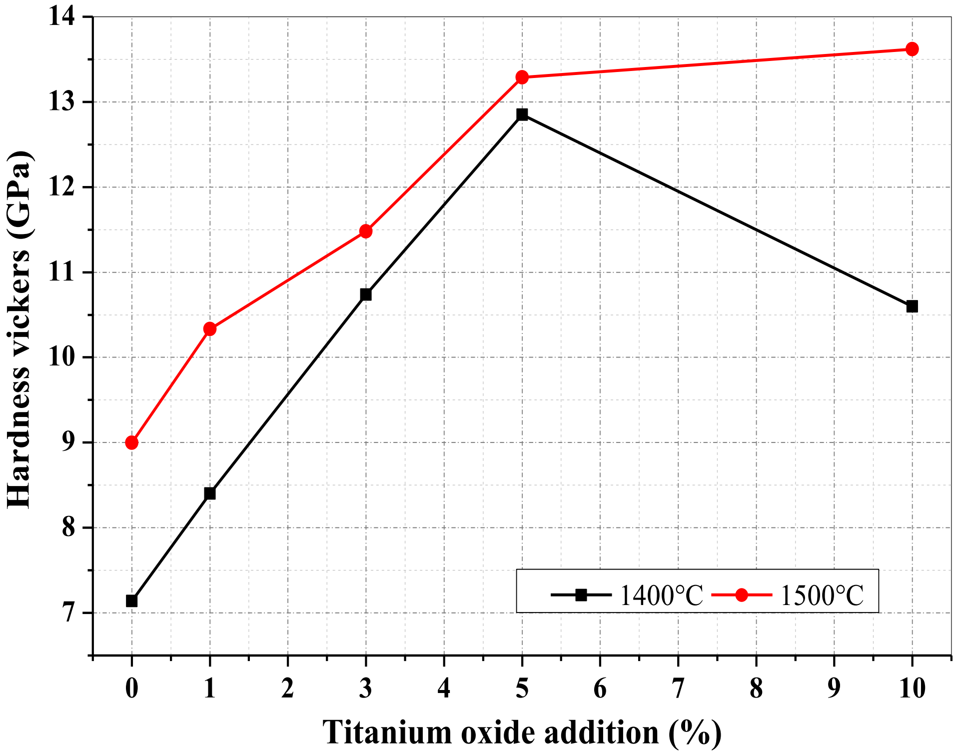

Fig.III.25: Micro-hardness of the Alumina-Fluorapatite sintered samples at 1400 and 1500°C sintering temperatures.

II.2.4. Determination of the fracture strength

PHA-T samples prepared with different percentages of TiO_2 : 0, 1, 3, 5, and 10 %Wt, are sintered under the same operating conditions (1400 and 1500°C for 2 h). The strength and elongation data are then processed to obtain the maximum breaking strength for each step. “Strength of each sample.” Fig. III.26 shows the evolution of the stress at break of the PHA-T composite.

The fracture toughness of the composites was remarkably improved by the addition of TiO_2 (Fig. III.26). A maximum value of about 140 MPa was obtained for the samples sintered at 1500°C with 3 wt% TiO_2 and 113 MPa for the samples sintered at 1400°C with 5 wt% TiO_2. Above this amount, the strength decreased with the addition of TiO_2 . The opposite phenomena of decrease in mechanical properties (Fig. III.25) and grain growth observed when increasing the weight content of TiO_2 were added to the composite may be related to the presence of the secondary phase of Al_2TiO_5 formed. At 5 wt% TiO_2, a fracture strength of approximately 67 MPa was observed. A reasonable explanation for this decrease would be related to the exaggerated grain growth (Fig. III.27), the formation of open porosity (Fig. III.24), and the generation of a secondary phase caused by the addition of TiO_2.

This result agrees with Awatef Guidara et al.'s work on alumina-based ceramics containing TiO_2, where the mechanical properties reached a maximum value for a TiO_2 content close to the solubility limit and then suddenly decreased beyond this amount [23].

We find that TiO_2 (maximally 5%) addition to the PHA-T matrix plays a significant role in fracture strength.

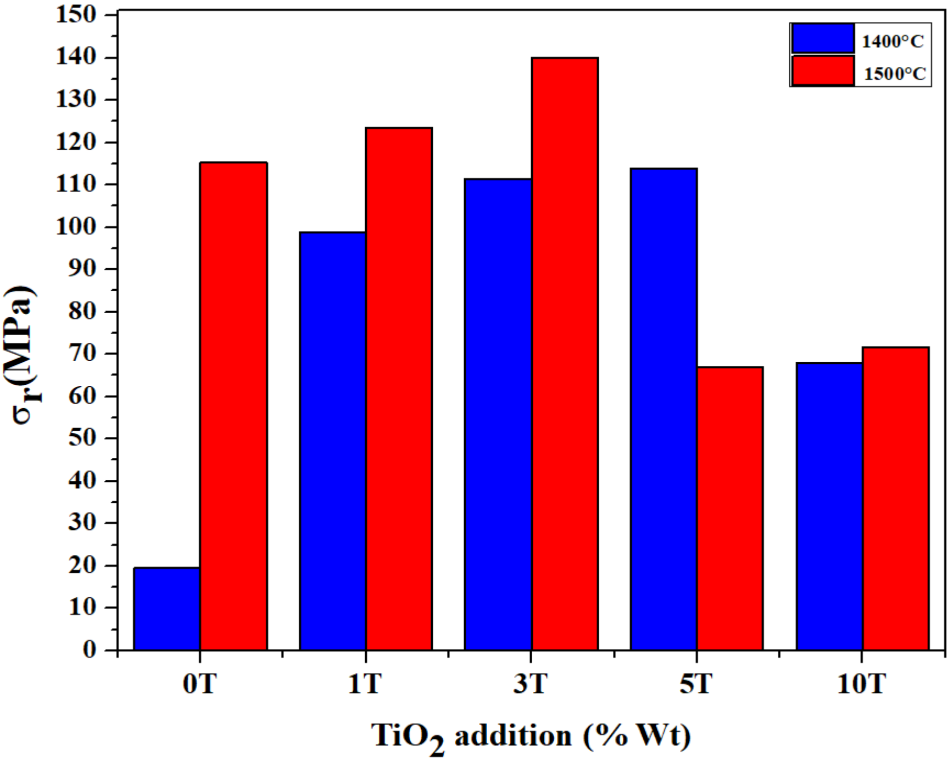

Fig. II.6 : Rupture strength behaviour of Al2O3-Fap composites sintered at 1400 and 1500°C for 2 h with TiO_2 additives.

II.2.5. Morphological analysis by SEM micrographic observation

SEM observations and elementary analysis on polished and heat-etched surfaces show the effect of composition and the effect of temperature on the morphological observations taken from sintered composites, as shown in Fig.III.27. The microstructure reveals that the porosity gradually increased with the increase of TiO_2 in the initial mixtures. Moreover, the grain size increased and became more distinguishable (elongated grains and large grain with almost hexagonal cross-sections) due to the intergranular porosity formed along with the gradual decrease in the amount of liquid phase, which occurred with the increase in the amount of TiO_2.

On the other hand, with increasing sintering temperature from 1400°C to 1600°C, (Fig.III.27), samples of both mixtures containing 0% (PHA0T 1600°C) and 10% (PHA10T 1600°C) TiO_2 showed better densification. They exaggerated grain growth, while the grains were elongated when the mixture contained a higher amount of TiO_2. The hexagonal lamellae were superimposed in the case of sintered samples without titania (Fig.III.8). These results are in good agreement with those previously obtained with open porosity and hardness, as observed in Fig.III.24 and Fig.III.25, respectively.

The previous works of Guidara and her partners[23, 26] were well consistent with the results obtained in the present work. They studied the effect of titania and other oxides on the structural and mechanical properties of fluorapatite and alumina composite. They found that adding more than 2wt% titania resulted in the formation of porosity between the grains and excessive grain growth. Besides, Mollazadeh et al.[29] studied the effect of titania and other oxides on the mechanical proprieties and crystallization behaviour of fluorapatite-mullite glass-ceramics, when they found that the addition of 3wt% of TiO_2 led to the precipitation of like-rode crystalline particles in the glass-ceramic [29]. Furthermore, Leite et al. [30] prepared the hibonite pigments from the industrial sludges. They reported the formation of hexagonal particles, which were referred to as the hibonite phase [30], just as the hexagonal grains in the case of sintered samples with a low content of titania. Whereas the XRD in Fig. 6 showed that the intensity of the formed hibonite decreased as the titania increased in the samples (it almost vanished in the sample containing 10wt% TiO_2). Thus, the results obtained from XRD are strongly in line with to the SEM observations, as the number of hexagonal grains also decreases with the increase in TiO_2 amount. Therefore, it can be note that the hexagonal grains are correspond to the hibonite phase.

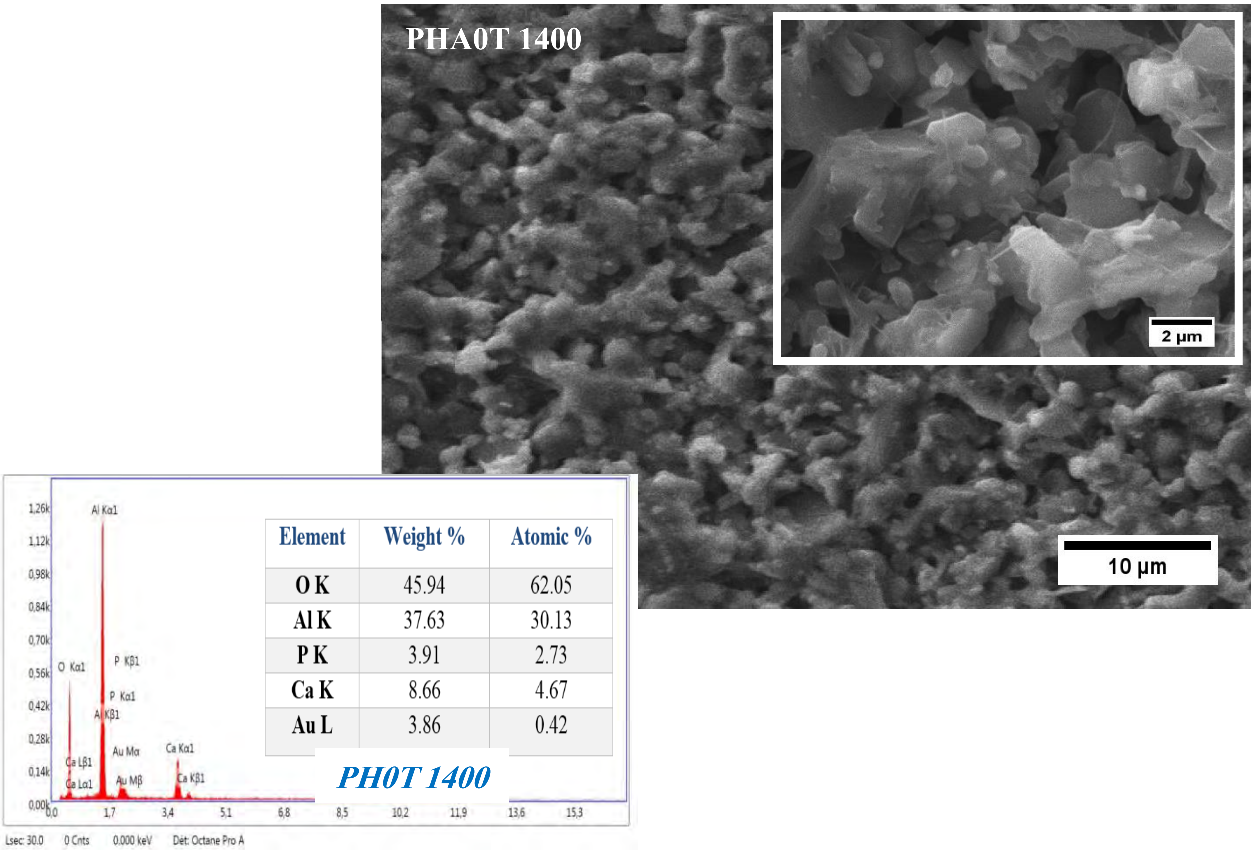

Element	Weight %	Atomic %
O K	45.94	62.05
Al K	37.63	30.13
P K	3.91	2.73
Ca K	8.66	4.67
Au L	3.86	0.42

PH0T 1400

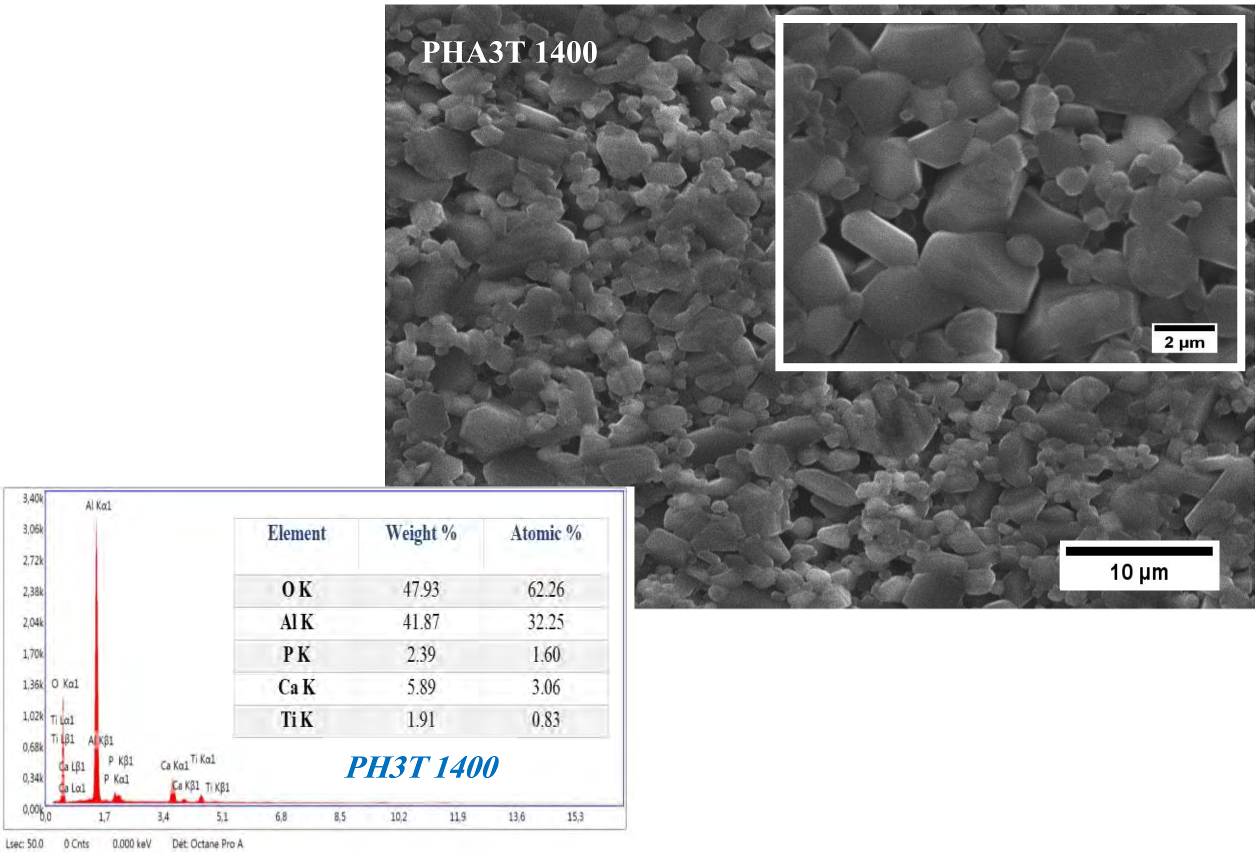

Element	Weight %	Atomic %
O K	47.93	62.26
Al K	41.87	32.25
P K	2.39	1.60
Ca K	5.89	3.06
Ti K	1.91	0.83

PH3T 1400

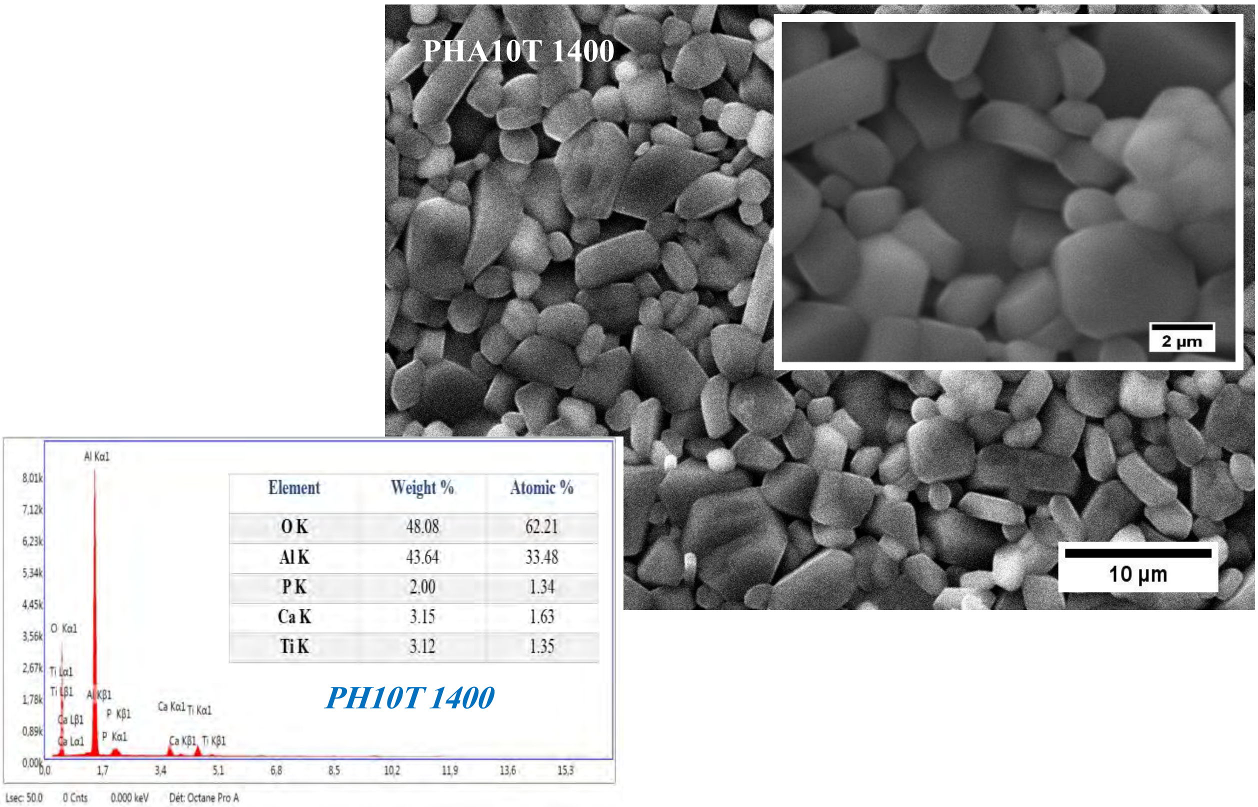

Element	Weight %	Atomic %
O K	48.08	62.21
Al K	43.64	33.48
P K	2.00	1.34
Ca K	3.15	1.63
Ti K	3.12	1.35

PH10T 1400

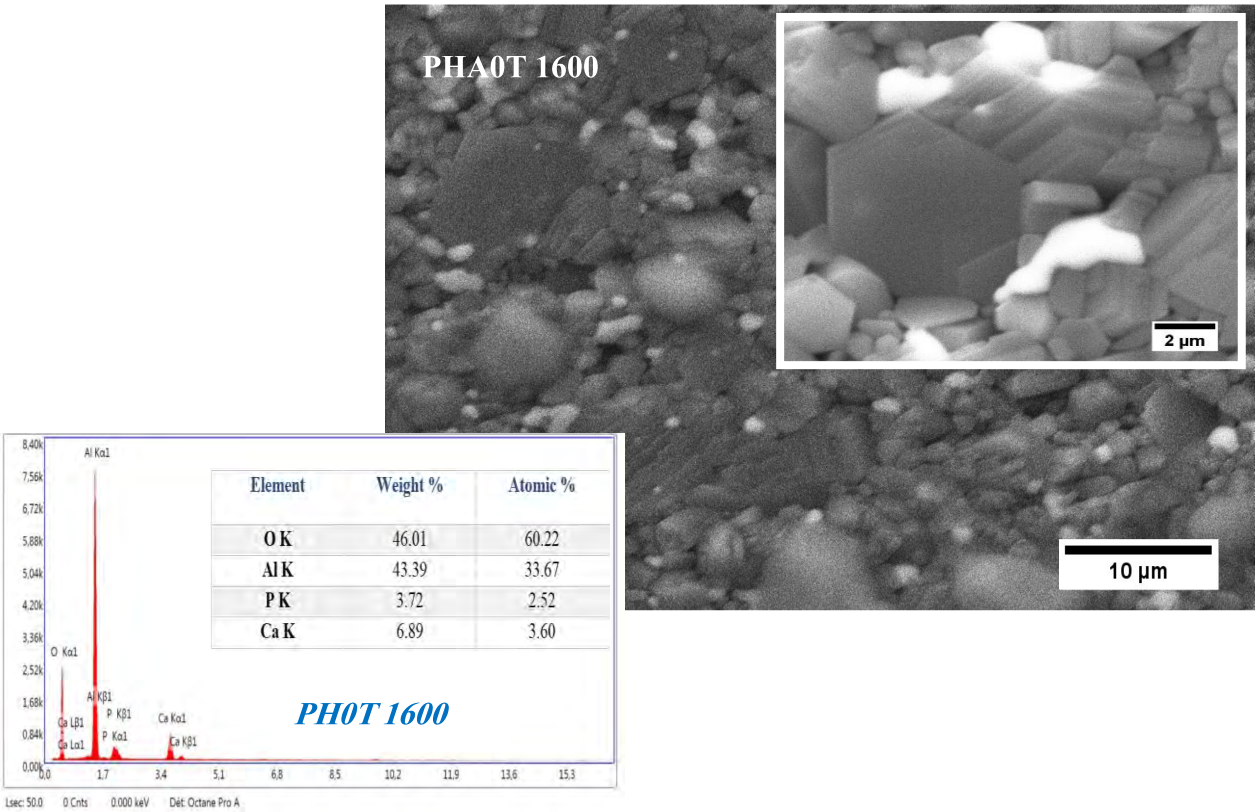

Element	Weight %	Atomic %
O K	46.01	60.22
Al K	43.39	33.67
P K	3.72	2.52
Ca K	6.89	3.60

PH0T 1600

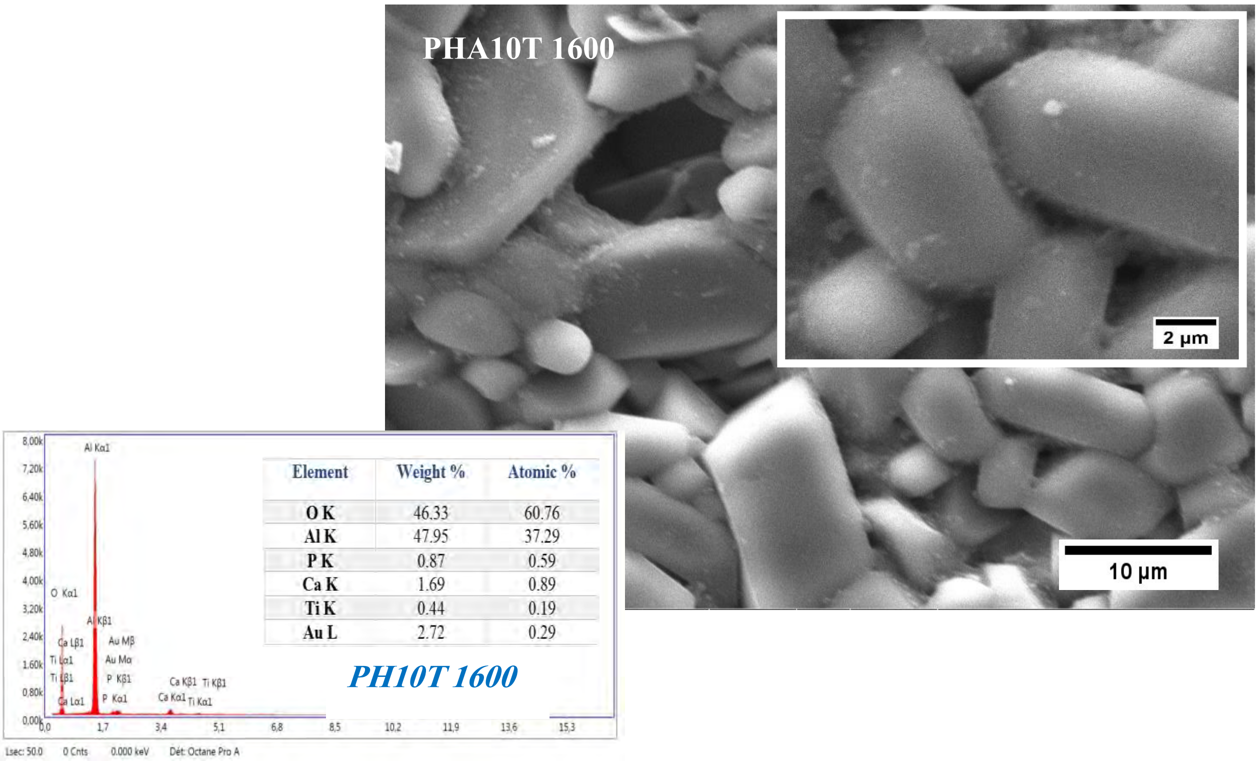

Element	Weight %	Atomic %
O K	46.33	60.76
Al K	47.95	37.29
P K	0.87	0.59
Ca K	1.69	0.89
Ti K	0.44	0.19
Au L	2.72	0.29

Fig.III.27: SEM observations of samples surface sintered at 1400°C with 0, 3 and 10 w.% of TiO2 (PHA0T 1400, PHA3T 1400 and PHA10T 1400 respectively), and sintered at 1600°C with 0 and 10 w.% of TiO2 (PHA0T 1600 and PHA10T 1600 respectively).

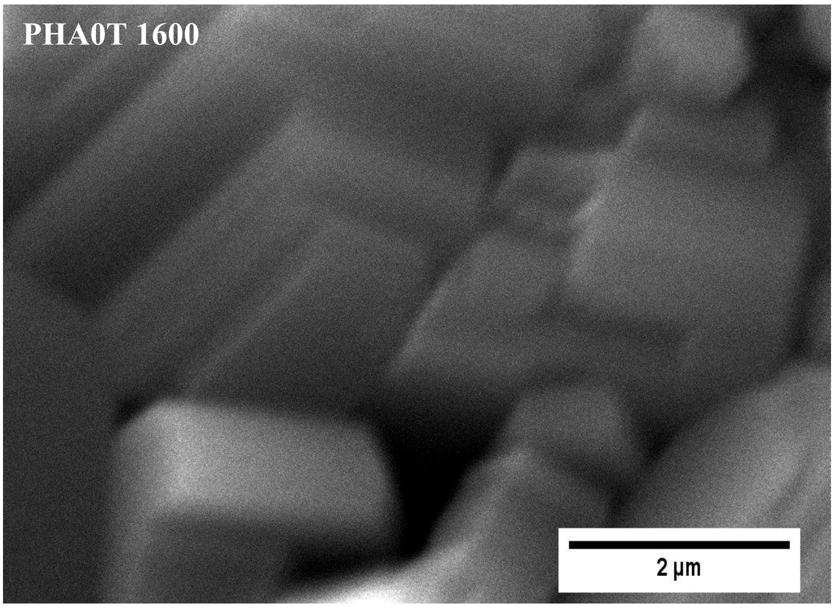

Fig.III.28: superposition of hexagonal lamellae)PH0T, 1600°C(.

References

1. H. Bachouâ, M. Othmani, Y. Coppel, F. Nabil, D. Mongi, B. Badraoui ., Structural and thermal investigations of a Tunisian natural phosphate rock. Journal of Materials and Environmental Science. 2014. **5**(4): p. 1152-1159.
2. I. Denry, O.M. Goudouri, J. Harless, JA. Holloway ., Rapid vacuum sintering: A novel technique for fabricating fluorapatite ceramic scaffolds for bone tissue engineering. Journal of biomedical materials research part b. 2018. **106**(1): p. 291-299. DOI: 10.1002/jbm.b.33825.
3. I. Denry, and JA. Holloway, Low temperature sintering of fluorapatite glass-ceramics. Dental Materials. 2014. **30**(2): p. 112-121. DOI: 10.1016/j.dental.2013.10.009.
4. F-Z, Mezahi, A. Lucas-Girot, H. Oudadesse, A. Harabi., Reactivity features of original sol-gel-derived 52S4 glass versus heat treatment temperature. Journal of the Australian Ceramic Society, 2018. **54**(4): p. 609-619. DOI: 10.1007/s41779-018-0189-0.
5. M. Azami, S. Jalilifiroozinezhad, M. Mozafari, M. Rabiee., Synthesis and solubility of calcium fluoride/hydroxy-fluorapatite nanocrystals for dental applications. Ceramics International. 2011. **37**(6): p. 2007-2014. DOI: 10.1016/j.ceramint.2011.02.025.
6. A. Mokhtari, H. Belhouchet, A. Guermat., In situ high-temperature X-ray diffraction, FT-IR and thermal analysis studies of the reaction between natural hydroxyapatite and aluminum powder. Journal of Thermal Analysis and Calorimetry. 2019. **136**(4): p. 1515-1526. DOI: 10.1007/s10973-018-7812-8.
7. H. Belhouchet, F. Chouia, M. Hamidouche, A. Leriche., Preparation and characterization of anorthite and hydroxyapatite from Algerian kaolin and natural phosphate. Journal of Thermal Analysis and Calorimetry.2016. **126**(3): p. 1045-1057. DOI: 10.1007/s10973-016-5655-8.
8. M. Montazerian, JF. Schneider, BE. Yektaa, VK. Marghussiana. AM. Rodriguesc, ED. Zanottoc, Sol–gel synthesis, structure, sintering and properties of bioactive and inert nano-apatite–zirconia glass–ceramics. Ceramics International. 2015. **41**(9): p. 11024-11045. DOI: 10.1016/j.ceramint.2015.05.047.
9. L. Pagliari, M. Dapiaggi, A. Pavese, F. Francescon., A kinetic study of the quartz–cristobalite phase transition. Journal of the European Ceramic Society. 2013. **33**(15-16): p. 3403-3410. DOI: 10.1016/j.jeurceramsoc.2013.06.014

10. O.H Magdalena, and J. Maciej, Thermal behavior of natural dolomite. Journal of Thermal Analysis and Calorimetry. 2015. **119**(3): p. 2239-2248. DOI: 10.1007/s10973-014-4301-6
11. A. Kenzour, H. Belhouchet, M. Kolli, S. Djouallah, D. Kherifi, S. Rameshef., Sintering behavior of anorthite-based composite ceramics produced from natural phosphate and kaolin. Ceramics International. 2019. 45(16): p. 20258-20265. DOI: 10.1016/j.ceramint.2019.06.299.
12. B. Nasiri-Tabrizi, and A. Fahami, Reaction mechanisms of synthesis and decomposition of fluorapatite–zirconia composite nanopowders. Ceramics International . 2013. **39**(5): p. 5125-5136. DOI: 10.1016/j.ceramint.2012.12.008.
13. N. Böhme, K. Hauke, M. Neuroth, and T. Geisler., In situ Raman imaging of high-temperature solid-state reactions in the $CaSO_4$–SiO_2 system. Minerals. 2019. **6**(2): p. 247-259. DOI: 10.3390/min10030287.
14. N. Betancur-Granados, JC. Restrepo, JI. Tobón, OJ. Restrepo-Baena., Dicalcium silicate ($2CaO\cdot SiO_2$) synthesized through flame spray pyrolysis and solution combustion synthesis methods. Ceramics International. 2019. **45**(7): p. 9589-9595. DOI: 10.1016/j.ceramint.2018.10.073.
15. P. Mazón, and N. Piedad, Porous scaffold prepared from α′ L-Dicalcium silicate doped with phosphorus for bone grafts. Ceramics International. 2018. **44**(1): p. 537-545. DOI: 10.1016/j.ceramint.2017.09.208.
16. M. Zawrah, and E. Hamzawy, Effect of cristobalite formation on sinterability, microstructure and properties of glass/ceramic composites. Ceramics International . 2002. **28**(2): p. 123-130. DOI: 10.1016/S0272-8842(01)00067-0.
17. S. Cole, The conversion of quartz into cristobalite below 1000°c, and some properties of the cristobalite formed*. The American Ceramic Society. 1935. **18**(1-12): p. 149-154. DOI: 10.1111/j.1151-2916.1935.tb19371.x.
18. G. Souza, P. Messer, and W. Lee, Effect of Varying Quartz Particle Size and Firing Atmosphere on Densification of Brazilian Clay-Based Stoneware. The American Ceramic Society. 2006. **89**(6): p. 1993-2002. DOI: 10.1111/j.1551-916.2006.00986.x.
19. E. Hamzawy, A. El-Kheshen, and M. Zawrah, Densification and properties of glass/cordierite composites. Ceramics International. 2005. **31**(3): p. 383-389. DOI: 10.1016/j.ceramint.2004.06.003.

20. F. Shirazi, M. Mehraliab, AA. Oshkoura, HSC. Metselaara, NA. Kadrib, NA. Abu Osmanb., Mechanical and physical properties of calcium silicate/alumina composite for biomedical engineering applications. Journal of the Mechanical Behavior of Biomedical Materials. 2014. **30**: p. 168-175. DOI: 10.1016/j.jmbbm.2013.10.024.
21. F.B. Ayed, and J. Bouaziz, Sintering of tricalcium phosphate–fluorapatite composites by addition of alumina. Ceramics International, 2008. **34**(8): p. 1885-1892. DOI: 10.1016/j.ceramint.2007.07.017.
22. S. Djouallah, H. Belhouchet, A. Kenzour, D. Kherifi., Sintering behavior of fluorapatite-based composites produced from natural phosphate and alumina. Ceramics International, 2021. **47**(3): p. 3553-3564. DOI: 10.1016/j.ceramint.2020.09.202.
23. A. Guidara, K. Chaari, S. Fakhfakh, J. Bouaziz., The effects of MgO, ZrO_2 and TiO_2 as additives on microstructure and mechanical properties of Al_2O_3-Fap composite. Materials Chemistry and Physics, 2017. **202**: p. 358-368. DOI: 10.1016/j.matchemphys.2017.09.039.
24. S.J. Kim, HG. Bang, JH. Song, SY. Park., Effect of fluoride additive on the mechanical properties of hydroxyapatite/alumina composites. Journal of the Korean Ceramic Society. 2009. **35**(4): p. 1647-1650. DOI: 10.1016/j.ceramint.2008.07.016.
25. A. Guidara, K. Chaari, S. Fakhfakh, J. Bouaziz., The effects of MgO, ZrO_2 and TiO_2 as additives on microstructure and mechanical properties of Al_2O_3-Fap composite. Materials Chemistry and Physics. 2017. **202**: p. 358-368. DOI: 10.1016/j.matchemphys.2017.09.039.
26. A. Guidara, K. Chaari, and J. Bouaziz, Effect of Titania Additive on Structural and Mechanical Properties of Alumina–Fluorapatite Composites. Journal of Materials Science & Technology, 2012. **28**(12): p. 1130-1136. DOI: 10.1016/S1005-0302(12)60182-0.
27. S. Sakka, J. Bouaziz, and F. Ben Ayed, Sintering and mechanical properties of the alumina–tricalcium phosphate–titania composites. Materials Science and Engineering: C, 2014. **40**: p. 92-101. DOI: 10.1016/j.msec.2014.03.036.
28. H. Manshor, SM. Aris, AZA. Azhar, EC. Abdullah, ZA. Ahmad., Effects of TiO2 addition on the phase, mechanical properties, and microstructure of zirconia-toughened alumina ceramic composite. Ceramics International, 2015. **41**(3, Part A): p. 3961-3967. DOI: 10.1016/j.ceramint.2014.11.080.

29. S. Mollazadeh, B. Eftekhari Yekta, J. Javadpour, A. Yusefi, T.S.Jafarzadeh., The role of TiO_2, ZrO_2, BaO and SiO_2 on the mechanical properties and crystallization behavior of fluorapatite–mullite glass–ceramics. Journal of Non-Crystalline Solids, 2013. **361**: p. 70-77. DOI: 10.1016/j.jnoncrysol.2012.10.009.

30. A. Leite, G. Costa, W. Hajjaji, M.J. Ribeiro, M.P. Seabra, J.A. Labrincha., Blue cobalt doped-hibonite pigments prepared from industrial sludges: Formulation and characterization. Dyes and Pigments, 2009. **81**(3): p. 211-217.

DOI: 10.1016/j.dyepig.2008.10.008.

Conclusion

General conclusion

In this work, we succeeded in synthesizing FAp and Calcium silicate composites using various Quartz (Q) ratios and Algerian natural phosphate, also Fap-Al_2O_3-CA_6 composite, and to study the mineralogy and microstructure of these elaborated composites, adopting the solid-state reaction to achieve this result.

In the first part of this study, the effects of quartz addition and sintering temperature on the phase development and properties of natural FAp-sintered composites were investigated. The XRD analysis of the sintered composites indicated that a mixed-phase was obtained for all composites with FAp as the major phase regardless of sintering temperature. Minor phases of tricalcium phosphate were observed for composites containing 5 wt% and above quartz content. The formation of dicalcium silicate was observed for the sample with 20 wt% quartz addition and sintered at temperatures > 1200°C. This condition was found to have an adverse effect on densification due to the transient liquid phase's excessive wetting during sintering. The FTIR analysis supported these findings. The addition of quartz was found to alter the composites' microstructure, where it exhibited a rod-like morphology when sintered at 1000°C and a regular rounded grain structure when sintered at 1350°C.

This study showed that the addition of 2.5 wt% quartz is effective in enhancing the densification and Vickers hardness of the FAp, particularly when sintered at a low temperature of 1100°C. Also, the addition of 20 wt% quartz effective in enhancing the micro-hardness, where it reached to 7 GPa, which is beneficial for biomedical applications.

The kinetic study of bioactivity in kokubo mode "immersion in SBF, allowed us to deduce that the samples containing 2.5 and 20% of quartz and treated at 1100 and 1350°C successively is more active than the others, forming apatite after 1 week of immersion in SBF on the surface of the samples FA2,5Q1.1K1W and FA20Q1.35K1W.

Quantitative and qualitative EDX analyses were performed on the surface of the samples after immersion in SBF solution for 16 weeks, where the formation of carbonated hydroxyapatite confirmed the FESEM results.

In the second part, the alumina-fluorapatite composites' sintering behavior from alumina and Algerian natural phosphate was investigated using the conventional sintering method from 1000 to 1600 ° C, and studying the effect of titanium oxide (0, 1, 3, 5, and 10%) on these composites' Physico-chemical properties.

The results indicated that the addition of titanium oxide effectively improved samples' density, especially those containing 3 and 5%, reaching a value of 3.22 g/cm^3, the percentage of open porosity reached 0,94 and 0,64%, respectively.

Also, this study found that titanium oxide has a clear and good effect on microhardness, and using large proportions of additives adversely affects the properties of these composites.

A study of the mechanical properties was examined during this study. Indeed, the optimal values of the fracture toughness of the PHA-T composites are revealed after sintering at 1500°C for 2h (σ_r = 140 MPa with 3 %Wt TiO2).

Therefore, we can say that we achieve the desired objective of this thesis, which is the development of bioceramics for medical applications.

Perspectives

The research work carried out in the framework of this thesis opens the way to numerous possibilities of investigation on biomaterials. Concerning these composites, we can mention :

- the in-vivo study of these biomaterials,
- the study of the mechanical properties of composites as a function of immersion time,
- the manufacture of these materials commercially.

Abstract

In this work, the sintering behavior of fluorapatite (FAp)–silicate composites prepared by mixing variable amounts of natural quartz (2.5 wt% to 20 wt%) and FAp was studied. The composites were sintered at temperatures from 1000 °C to 1350 °C. The effects of temperatures on the densification, phase formation, chemical bonding, and Vickers hardness of the composites were evaluated. All the samples exhibited mixed phases, comprising FAp and francolite as the major constituents along with some minor phases of cristobalite, wollastonite, dicalcium silicate, and/or whitlockite dependent on the quartz content and sintering temperature. The composite containing 2.5 wt% quartz exhibited the best sintering properties. The highest bulk density of 3 g/cm^3 and a Vickers hardness of > 4.2 GPa were obtained for the 2.5 wt% quartz–FAp composite when sintered at 1100 °C. The formation of carbonated HAp in the in-vitro test " immersion in SBF" confirms that we have bioactive materials. In the second part, the alumina-fluorapatite composites' sintering behaviour from alumina and Algerian natural phosphate was investigated using the conventional sintering method from 1000 to 1600 ° C. Besides; we were studying the effect of titanium oxide (0, 1, 3, 5, and 10%) on these composites' Physico-chemical properties. Sintered samples were examined in terms of formed phases by X-ray diffraction, shrinkage rate, bulk density, open porosity ratio, Vickers microhardness, Tensile strength, and SEM's morphological structure. The results indicated that the addition of titanium oxide effectively improved samples' density, especially those containing 3 and 5%, reaching a value of 3.22 g/cm3, and the percentage of open porosity reached 0,94 and 0,64%, respectively. Also, this study found that titanium oxide has a clear and good effect on microhardness, reached to 13.65 GPa and a Hight fracture strength of about 140 MPa, and using large proportions of additives adversely affects the properties of these composites.

Keywords

Natural phosphate, fluoropatite, quartz, alumina, biomaterials, mechanical properties.

الملخص

تم في هذا العمل دراسة سلوك تلبيد مركبات سيليكات الفلوراباتيت (FAp) المحضرة بخلط كميات متغيرة من الكوارتز الطبيعي (2.5٪ إلى 20٪ وزنا) و FAp. تمت دراسة تأثير درجات حرارة التلبيد على التكثيف وتشكل الأطوار والارتباط الكيميائي وصلادة فيكارز للمركبات. أظهرت نتائج التحليل بواسطة جهاز انعراج الأشعة السينية وجود أطوار مختلفة ، تشتمل على FAp و francolite كمكونات رئيسية مع بعض المراحل الثانوية من cristobalite و wollastonite و dicalcium silicate و/أو whitlockite اعتمادًا على محتوى الكوارتز ودرجة حرارة التلبيد. أظهر المركب المحتوي على 2.5٪ وزنا من الكوارتز نتائج بارزة عند تلبيده عند درجة حرارة 1100 درجة مئوية، حيث تم الحصول على أعلى كثافة حجمية تبلغ حوالي 3 غ/سم^3 وصلادة فيكارز> 4.2 جيغا باسكال، كما يؤكد تشكل الهيدروكسي أباتيت الكربوني في اختبار "الغمر في المحلول الفيزيولوجي" أن لدينا مواد نشطة حيويا. في الجزء الثاني ، تم فحص سلوك تلبيد مركبات الألومين–فلوراباتيت المحضرة من الفوسفات الطبيعي المحلي والألومين المخبري الملبدة من 1000 إلى 1600 درجة مئوية. كما درسنا تأثير أكسيد التيتانيوم (0 ، 1 ، 3 ، 5 ، 10٪ وزنا) على الخواص الفيزيائية والكيميائية لهذه المركبات. تم فحص العينات الملبدة من حيث الأطوار المكونة عن طريق حيود الأشعة السينية ، ومعدل الانكماش، والكثافة الظاهرية، ونسبة المسامية المفتوحة، وصلادة فيكارز، وقوة الكسر، والبنية المورفولوجية. أشارت النتائج إلى أن إضافة أكسيد التيتانيوم أدى بشكل فعال إلى تحسين كثافة العينات ، خاصة تلك التي تحتوي على 3 و 5٪ وزنا من أكسيد التيتانيوم، وبلغت قيمة 3.22 غ/ سم^3، حيث بلغت نسبة المسامية المفتوحة 0.94 و 0.64٪ على التوالي. كما وجدنا في هذه الدراسة أن لأكسيد التيتانيوم تأثير واضح وجيد على الصلادة المجهرية، حيث وصلت إلى 13.65 جيجا باسكال وقوة كسر عالية تبلغ حوالي 140 ميجا باسكال ، وأن استخدام نسب كبيرة من الإضافات يؤثر سلبًا على خصائص هذه المركبات.

كلمات مفتاحية

الفوسفات الطبيعي، الفليوراباتيت، الكوارتز، الألومين، المواد الحيوية، الخصائص الميكانيكية.

Ceramics International 47 (2021) 16483–16490

Contents lists available at ScienceDirect

Ceramics International

journal homepage: www.elsevier.com/locate/ceramint

Sintering behaviour of fluorapatite–silicate composites produced from natural fluorapatite and quartz

D. Kherifi [a,b], H. Belhouchet [b], S. Ramesh [c,d,*], K.Y. Sara Lee [e], A. Kenzour [f,g], S. Djoualah [f], M.K. G. Abbas [c], Y.H. Wong [c], S. Ramesh [h]

[a] Physics and Chemistry of Materials Lab, Department of Physics, University Mohamed Boudiaf of M'sila, Algeria
[b] Physics Department, Faculty of Sciences, University Mohamed Boudiaf of M'sila, 28000, M'sila, Algeria
[c] Center of Advanced Manufacturing and Material Processing, Department of Mechanical Engineering, Faculty of Engineering, University of Malaya, 50603, Kuala Lumpur, Malaysia
[d] Department of Mechanical Engineering, Faculty of Engineering, Universiti Teknologi Brunei, Tungku Highway, BE1410, Brunei Darussalam
[e] Department of Mechanical Engineering, Faculty of Engineering and Technology, Tunku Abdul Rahman University College, Jalan Genting Kelang, 53300, Kuala Lumpur, Malaysia
[f] Optics and Precision Mechanics Institute, University of Ferhat, Abbas Setif 1, 19000, Setif, Algeria
[g] Research Center in Industrial Technologies CRTI, P.O. Box 64, 16014, Cheraga, Algiers, Algeria
[h] Centre for Ionics University of Malaya, Department of Physics, Faculty of Science, University of Malaya, 50603, Kuala Lumpur, Malaysia

ARTICLE INFO

Keywords:
Fluorapatite
Quartz
Composites
Sintering behaviour

ABSTRACT

In this work, the sintering behaviour of fluorapatite (FAp)–silicate composites prepared by mixing variable amounts of natural quartz (2.5 wt% to 20 wt%) and FAp was studied. The composites were pressureless sintered in air at temperatures from 1000 °C to 1350 °C. The effects of temperatures on the densification, phase formation, chemical bonding and Vickers hardness of the composites were evaluated. All the samples exhibited mixed phase, comprising FAp and francolite as the major constituents along with some minor phases of cristobalite, wollastonite, dicalcium silicate and/or whitlockite dependent on the quartz content and sintering temperature. The composite containing 2.5 wt% quartz exhibited the best sintering properties. The highest bulk density of 3 g/cm^3 and a Vickers hardness of >4.2 GPa were obtained for the 2.5 wt% quartz–FAp composite when sintered at 1100 °C. The addition of quartz was found to alter the microstructure of the composites, where it exhibited a rod-like morphology when sintered at 1000 °C and a regular rounded grain structure when sintered at 1350 °C. A wetted grain surface was observed for composites containing high quartz content and was believed to be associated with a transient liquid phase sintering.

1. Introduction

Calcium phosphate bioceramics, such as hydroxyapatite (HAp), carbonated HAp, fluorapatite (FAp) and chlorapatite (ClAp) are remarkably used for orthopaedics and orthodontic applications owing to their excellent biocompatibility, osseointegration and osteoconductive properties [1–9]. In particular, FAp ($Ca_{10}(PO_4)_6F_2$) has recently attracted considerable attention because the presence of fluoride enhances the biodegradability and compressive strength and stimulates the formation of bone tissues. Bogdanov et al. [10] demonstrated the viability of preparing fluorapatite glass ceramics by heat treatment process (i.e. melting at 1450 °C/2 h followed by crystallization at 680 °C/12 h) of glass mixture (SiO_2–Al_2O_3–P_2O_5–CaO–CaF). The XRD analysis revealed that FAp was the major crystalline phase with occasionally some minor phases such as apatite, norbergite, vitlokite, fluorphlogopite, fluormargarite and sellaite being present. Mirjalili et al. [11] investigated fluorapatite-based nanocomposites with additions of forsterite (up to 35%) and found that the bioactivity of the composites was enhanced and that the release of silicon ion when exposed in SBF solution intensified for samples containing forsterite. A similar improvement trend was also noted for the compressive strength of the FAp composites. However, a major issue with FAp is the low fracture toughness and poor wear-resistance exhibited by the sintered body, thereby limiting its application in the biomedical field [11]. Hence, different FAp-based

---

* Corresponding author. Center of Advanced Manufacturing and Material Processing, Department of Mechanical Engineering, Faculty of Engineering, University of Malaya, 50603, Kuala Lumpur, Malaysia.
E-mail address: ramesh79@um.edu.my (S. Ramesh).

https://doi.org/10.1016/j.ceramint.2021.02.216
Received 24 January 2021; Received in revised form 17 February 2021; Accepted 23 February 2021

Table 1
Chemical composition (wt%) of natural FAp and natural quartz used in the present work.

Elements	F	Na_2O	MgO	Al_2O_3	SiO_2	P_2O_5	SO_3	K_2O	CaO	Fe_2O_3	ZnO	SrO	Y_2O_3	L.O.I.
FAp	3.65	1.13	0.89	0.87	1.79	28.2	2.55	0.138	59.9	0.455	0.038	0.345	0.044	–
Q	–	0.85	0.75	0.027	99.9	0.001	–	0.002	0.001	0.005	–	–	–	0.01

biocomposites, such as tricalcium phosphate- FAp (β-TCP-FAp) [12], kaolin- FAp [13], zinc oxide- FAp [14] and zirconia-FAp [15], have been studied to improve their mechanical properties.

Numerous studies have demonstrated that silica-containing bioceramics have excellent bioactivity and enhanced mechanical properties, thereby leading to the discovery of their potential in biomedical applications [16–18]. Fuh et al. [16] prepared micro-porous Si-substituted HAp by immersing hydroxyapatite compact disc in tetraethoxysilane (TEOS) followed by hydrolysis and condensation reaction to allow silicon gel formation before sintering. The authors found that the TEOS-treated HA possessed higher biaxial flexural strength and excellent cytocompatibility when compared to pure HAp having the same porosity level. Lin et al. [17] studied the effect of strontium (Sr) and silicon (Si) in $Sr_5(PO_4)_2SiO_4$ bioceramics on the *in vitro* cytocompatibility and osteogenic property for inducing osteanagenesis. Their results indicated that the simultaneous release of Sr and Si ions from the bioceramics played a significant role in improving the proliferation and osteogenic differentiation when compared with pure β-TCP. Khan et al. [18] affirmed the benefits of Si-substituted bioceramics and agreed that Si inclusion improved the biological performance of calcium phosphate based bioceramics. However, the authors inferred that the actual mechanism by which Si improves the osteoconductivity of the bioceramics remains unclear and requires further investigation.

In another study, the incorporation of a 50% wollastonite ($CaSiO_3$) phase in the HAp matrix successfully improved the compressive strength of sintered body by more than 50%, accompanied by higher degradation rate and excellent bioactivity compared with conventional HAp scaffold [19]. Sprio et al. [20] demonstrated that 20 wt% of dicalcium silicate (Ca_2SiO_4) is effective in aiding the densification of HAp. They found that the composite achieved 95% of theoretical density and flexural strength of 70.4 MPa when subjected to hot pressing at 1500 °C, whereas the flexural strength of monolithic HAp only attained 45 MPa [20]. In a recent study, kaolin-FAp composite was prepared, where the main compositions in kaolin are silica and alumina. The density and hardness of the composite increased with an increase in kaolin content. It was shown that the sample with the addition of 57 wt% kaolin achieved a relative density of 97% and the highest hardness of approximately 6.5 GPa when sintered at 1325 °C [13].

Borkowski et al. [21] studied the physicochemical and biological properties of FAp synthesised by using the sol-gel method and sintered at various temperatures. It was found that FAp sintered at 800 °C exhibited optimal porosity and fluoride release capacity thus enhancing the proliferation of osteogenic cells as compared to the control group. Golafshan et al. [22] prepared strontium-fluorapatite (Sr-FAp), magnesium and silicon-doped fluorapatite (Mg-SiFAp) by mechanochemical method. They found that the dopants were effective in promoting *in vitro* cellular proliferation and enhanced bone formation when compared to the undoped FAp. Other dopants such as alumina (Al_2O_3) was also found to be effective in promoting the sintering of FAp. Djouallah et al. [23] investigated the reaction-sintering between fluorapatite and Al_2O_3 using natural phosphate and boehmite by mechanical mixing process. The sintering was performed in air atmosphere at various temperatures (1000–1500 °C). The results revealed that the densification and micro-hardness of FAp improved with increasing Al_2O_3 content and sintering temperature. It was found that the 25% Al_2O_3-doped FAp exhibited the highest density (2.95 g/cm^3) and hardness (6.5 ± 0.25 GPa) when sintered at 1450 °C. The authors also noted that the physical and mechanical properties of the FAp were influenced by the phases formed which were dependent on the alumina content and sintering conditions. Similar improvements in the mechanical properties were also reported by Youness et al. [24] for alumina-based carbonated fluorapatite.

In the present work, silicate-doped FAp composites were prepared for the first time by mixing natural FAp and quartz. This work aimed to investigate the effects of quartz addition up to 20 wt% on the phases and densification behaviour of FAp when subjected to pressureless sintering.

2. Materials and methods

The starting materials used in the present work are natural FAp and natural quartz (Q), which were obtained from Algeria [13]. Varying amounts of quartz, such as 2.5, 5, 10 and 20 wt% were mixed with FAp, and the samples were subsequently labelled as FA2.5Q, FA5Q, FA10Q and FA20Q, respectively. The mixing of the powder was accomplished by using a planetary ball mill (Fritsch P6) at a rotation speed of 350 rpm for 10 h. In a typical powder preparation, the required amounts of quartz and FAp powders were measured and placed inside a 250 ml zirconia jar containing zirconia balls (10 mm diameter) as the milling media and distilled water as the milling medium. The resulting mixture was dried at 120 °C for 24 h and sieved through a 100 μm mesh sieve after the milling is completed. The obtained powder was calcined at 900 °C for 2 h at a heating rate of 10 °C/min to remove any residual organic. The powders were then uniaxially pressed at 100 MPa to produce disc samples (13 mm diameter). The green samples were pressureless sintered in air at various temperatures between 1000 °C and 1350 °C for 2 h at a heating rate of 10 °C/min.

The phases present in the powders and sintered composites were identified through X-ray diffraction (XRD, X'Pert Pro, EMPYREAN, PANalytical, Netherlands) with CuKα radiation at 40 kV and 30 mA. The scan was conducted at a speed of 4°/min and step scan of 0.026°, over the 2θ from 20° to 55°. The phase identification was accomplished by comparing the XRD signatures of the sample with the database provided by the Joint Committee on Powered Diffraction Standards (JCPDS). The elemental composition of the samples was obtained through X-ray fluorescence (XRF).

The resulting chemical functional groups in the samples were determined from the Fourier transform infrared spectroscopy (FTIR) spectra taken over the wavenumber range of 2000 cm^{-1} to 400 cm^{-1} by using a Shimadzu IRAffinity-1S spectrophotometer. For this purpose, 2 mg of powder was mixed with 98 mg of potassium bromide for the FTIR study. Differential thermal analysis (DTA) of the composites was conducted with a LABSYS evo DTA/DSC Setaram equipment. The bulk density of the sintered samples was measured using the Archimedes method. A Vickers microhardness testing machine (Zwick-Roell, ZHV, Germany) was used to measure the hardness of the sintered samples under an indentation load of 300 g and loading time of 10 s. Prior to the hardness test, the samples were polished with a 6 and 1 μ diamond paste. Five measurements were taken on each sample to determine the average hardness. The microstructure of the fractured surface was examined with a Zeiss Sigma field emission scanning electron microscope (FESEM).

3. Results and discussion

The chemical compositions of FAp and quartz as determined from the XRF are presented in Table 1. The FAp in its natural form is composed mainly of CaO (59.9%) and P_2O_5 (28.2%), whereas the quartz comprises predominantly 99.9% SiO_2 with high purity. The XRD

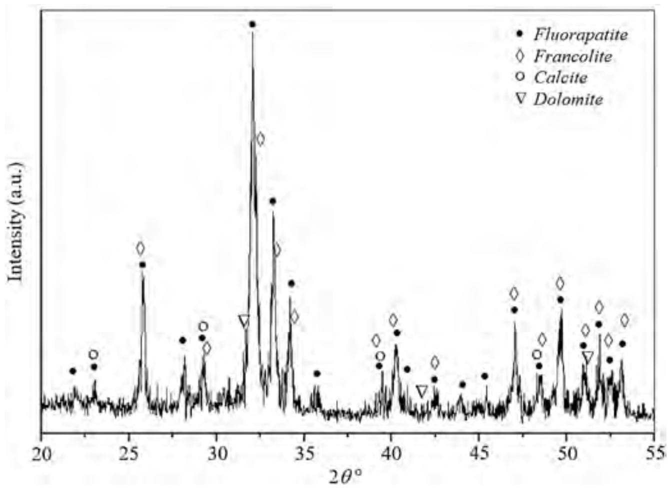

Fig. 1. XRD analysis of the as-received natural FAp powder showing a mix phase was present.

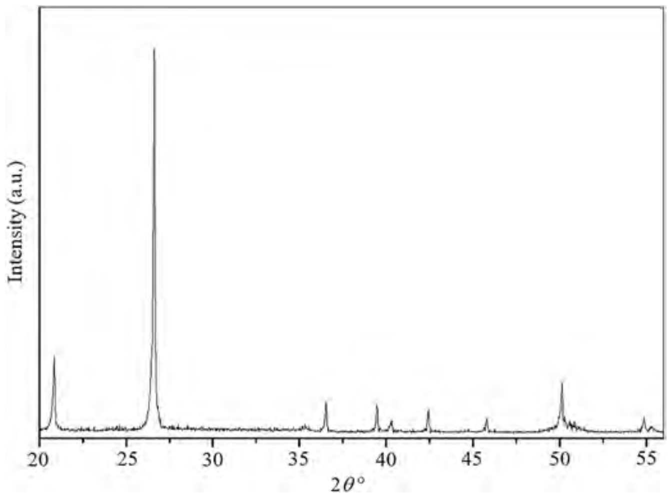

Fig. 2. XRD spectrum of the as-received natural quartz. All the peaks belongs to the SiO_2 phase.

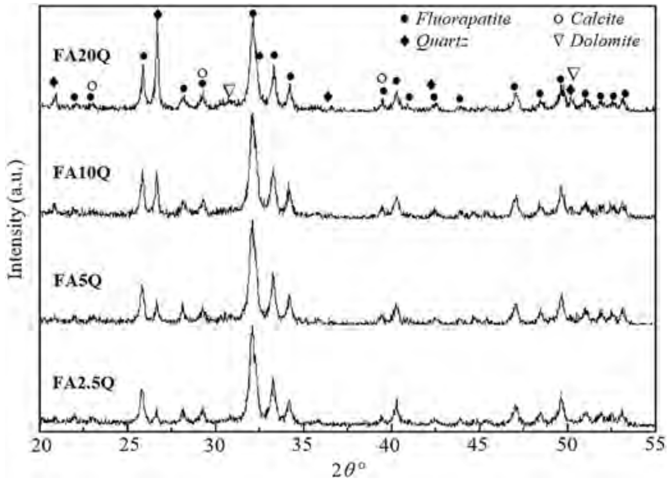

Fig. 3. Comparison of XRD signatures of the composite powders before calcination.

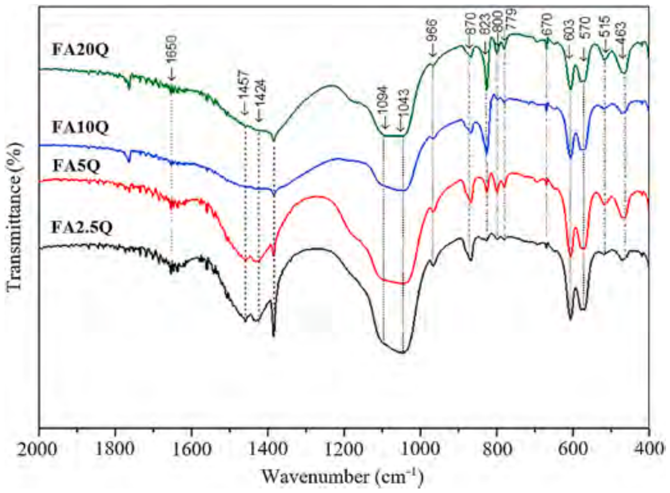

Fig. 4. FTIR spectra of composites before calcination.

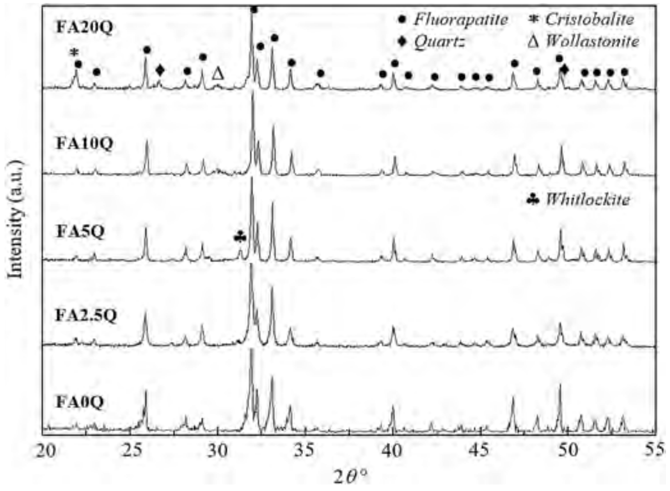

Fig. 5. XRD patterns of composite powders after calcination at 900 °C.

spectrum of the starting FAp (Fig. 1) showed that fluorapatite (JCPDS No. 15-876) and francolite (JCPDS No. 31-267) are the major phases, whereas dolomite (JCPDS No. 83-1530) and calcite (JCPDS No. 47-1743) represent the minor phases. For the natural quartz, silica (JCPDS No. 46-1045) was identified as the main phase (Fig. 2). The XRD patterns of the composite powders before calcination are shown in Fig. 3. Regardless of the quartz content, all mixtures exhibited the major crystalline phases of FAp and quartz, with small amounts of calcite and dolomite. The intensity of quartz, which is noticeable at $2\theta = 26.5°$, increases with the increased in quartz content in the mixture powder.

The FTIR spectra of the composite powders before calcination are presented in Fig. 4. The strong bands detected at 870 and 1385 cm^{-1} and the weak bands at 1424 and 1457 cm^{-1} are related to the presence of CO_3^{2-} group [25,26]. With the increase in the quartz content in FAp, the intensity of these bands decreases. Another strong band at 966 cm^{-1} is related to the mode ν_1 of PO_4^{3-} group, and the band at 1094 and 1043 cm^{-1} corresponds to the mode ν_3 of PO_4^{3-} group [26,27]. Two distinctive bands at 603 and 570 cm^{-1} are associated with the ν_4 of PO_4^{3-} group [26]. The intensity of the bands related to PO_4^{3-} group does not change with the addition of quartz. The bands at 823, 800, 779, 670, 515 and 463 cm^{-1} are associated with the silicate Si–O–Si network vibrations [25,28,29]. As expected, the intensity at 823 cm^{-1} strengthens with the increase in quartz content [30–32].

The effects of calcination on the phases present in the composite

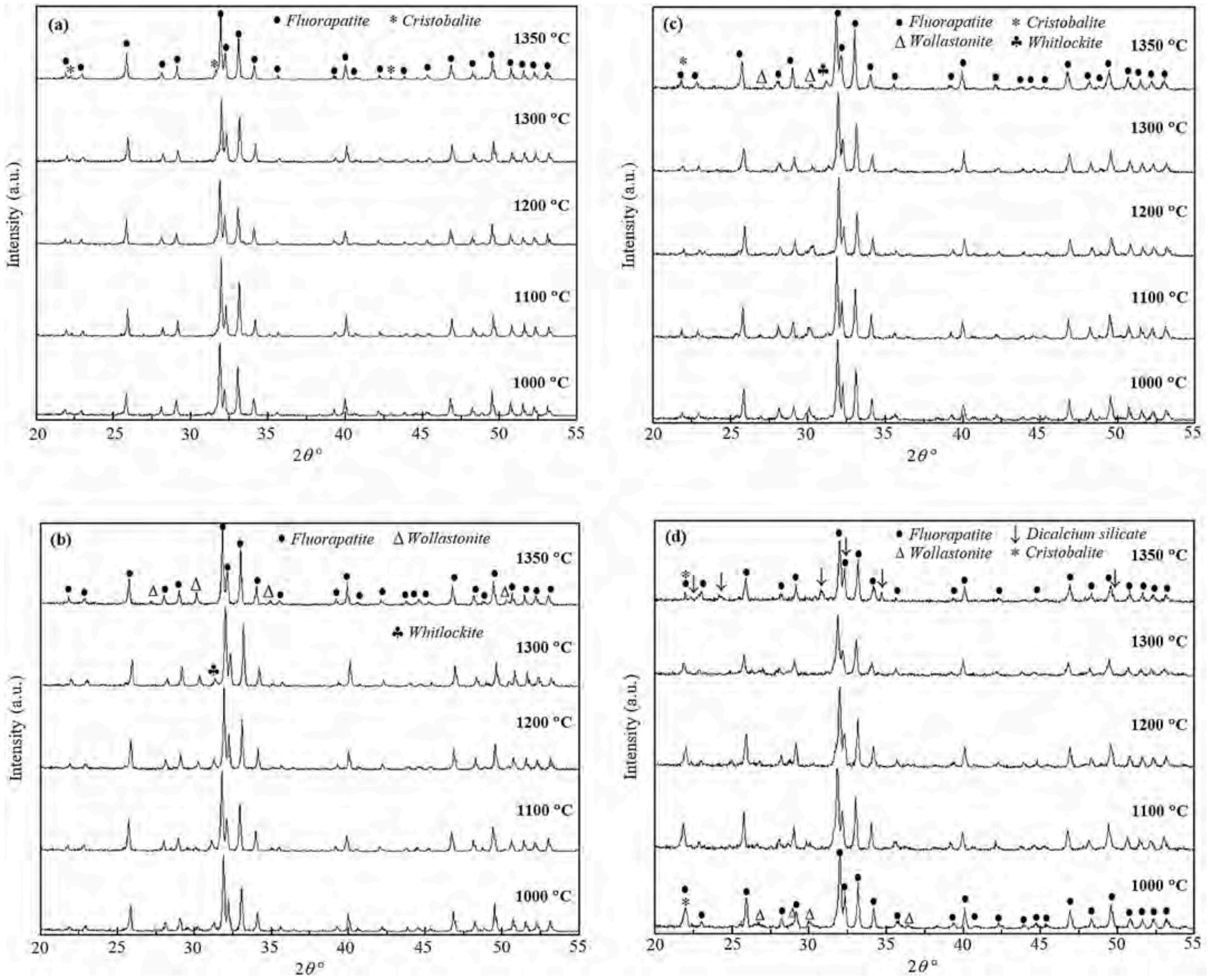

Fig. 6. XRD patterns for the various fluorapatite composites sintered at various temperatures: (a) FA2.5Q, (b) FA5Q, (c) FA10Q and (d) FA20Q.

powders are shown in Fig. 5. All composites consist of the major crystalline phases of FAp regardless of the quartz addition. The peak corresponding to that of quartz, particularly at 2θ ~26.5°, is clearly visible for the FA20Q sample when compared with the undoped powder (FA0Q). The phases that appeared in the composites after calcination include cristobalite (JCPDS No. 39-1425), wollastonite (JCPDS No. 43-1460) and whitlockite (JCPDS No. 09-0169). A strong peak of cristobalite is evident for the composite with 20 wt% quartz addition. Quartz start to transform into cristobalite at approximately 1190 °C and above [33]. However, in this work, the transformation from quartz to cristobalite occurred at a low temperature of 900 °C. A reaction between the FAp and excess quartz contributed to the reduction in quartz–cristobalite transformation temperature. The wollastonite peak started to appear when the composition of quartz was increased to 10 wt%. Free calcium oxide (CaO) decomposed from calcite ($CaCO_3$) and dolomite $CaMg(CO_3)_2$ due to the calcination at 900 °C [34]. The formation of wollastonite ($CaSiO_3$) as observed for FA10Q and FA20Q samples was due to the reaction between the free CaO and cristobalite (SiO_2) based on reaction [13] in accordance with Eq. (1).

$$CaO + SiO_2 \rightarrow CaSiO_3 \tag{1}$$

The formation of wollastonite was also due to the reaction between the calcite and excess SiO_2 present in the composites (FA10Q and FA20Q) in accordance with Eq. (2).

$$CaCO_3 + SiO_2 \rightarrow CaSiO_3 + CO_2 \tag{2}$$

In this work, the presence of whitlockite (tricalcium phosphate) in FA5Q can be associated with the decomposition of FAp at the calcination temperature to form tricalcium phosphate and CaF_2 [35] in accordance with Eq. (3).

$$Ca_{10}(PO_4)_6F_2 \rightarrow 3Ca_3(PO_4)_2 + CaF_2 \tag{3}$$

The XRD patterns of the composites containing different amounts of quartz and sintered at varying temperatures are shown in Fig. 6(a–d). The presence of FAp is clearly visible in all the composites regardless of the sintering temperatures and quartz content. The intensity of FAp is low in FA20Q (Fig. 6d) when sintered at 1300 °C and 1350 °C. This condition can be due to the partial fusion of FAp with quartz. For samples containing 5 wt% quartz and above, trace of whitlockite was detected at 2θ ~31.5° when sintered from 1000 °C to 1300 °C. However, this phase diminished when sintered at 1350 °C. The whitlockite was not detected in sample FA20Q throughout the sintering regime. A distinctive peak of wollastonite at 2θ ~30° was observed for sample FA5Q when sintered from 1200 °C to 1350 °C. The presence of wollastonite was

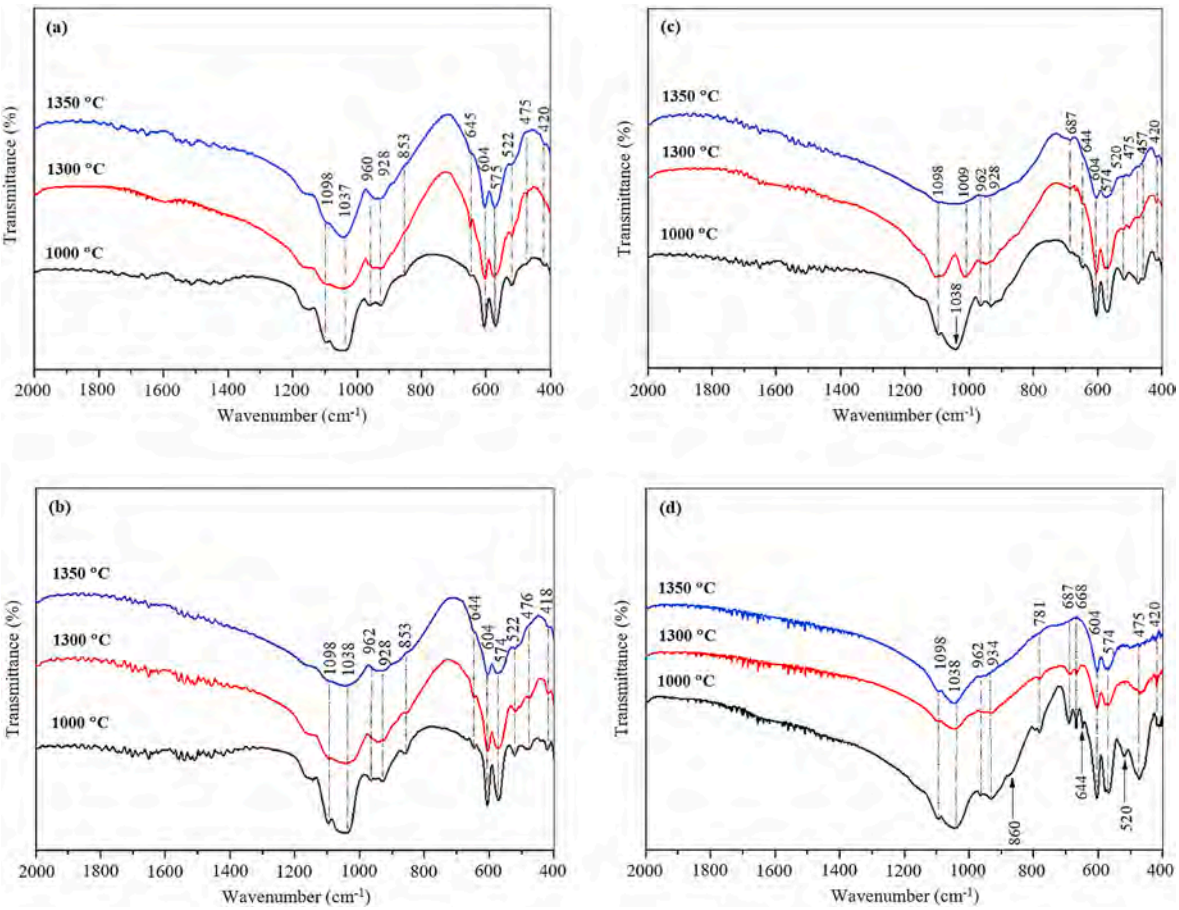

Fig. 7. FTIR analysis of composites sintered at various temperatures (a) FA2.5Q, (b) FA5Q, (c) FA10Q and (d) FA20Q.

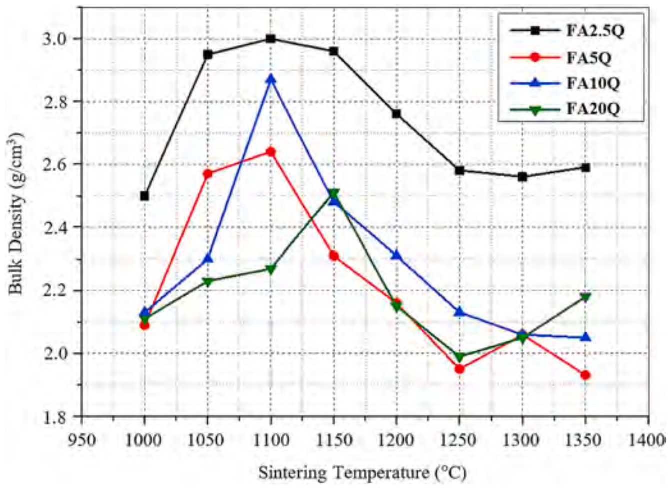

Fig. 8. Effect of sintering temperatures on the bulk density of fluorapatite composites.

Table 2
The bulk density and Vickers hardness of composites sintered at 1100 °C.

Sample	FA2.5Q	FA5Q	FA10Q	FA20Q
Bulk density (g/cm^3)	3.0 ± 0.10	2.63 ± 0.15	2.88 ± 0.17	2.28 ± 0.12
Vickers Hardness (GPa)	4.33 ± 0.32	4.67 ± 0.41	4.45 ± 0.36	4.42 ± 0.45

noticed for sample FA10Q at all sintering temperatures. The intensity of wollastonite peaks started to decrease in sample FA20Q when sintered from 1000 °C to 1100 °C, and this phase was not detected when sintered at 1200 °C and above. A strong peak of cristobalite at $2\theta \sim 22^\circ$ was detected when the quartz content was increased to 20 wt%. The intensity of the cristobalite peak decreases when the sintering temperature increases from 1000 °C to 1350 °C. The formation of dicalcium silicate (JCPDS No. 20-0237) in this composite can be associated with the reaction between wollastonite ($CaSiO_3$) and CaO when sintered at high temperatures above 1200 °C on the basis of the reaction given in Eq. (4) [36].

$$CaSiO_3 + CaO \rightarrow Ca_2SiO_4 \tag{4}$$

The FTIR spectra for the composites sintered at 1000 °C, 1300 °C and 1350 °C are shown in Fig. 7(a–d). Regardless of quartz content, the absorption bands at 1098 and 1038 cm^{-1} corresponding to the v_3 antisymmetric vibration (stretching) mode of PO_4^{3-} group of FAp were present. Other bands corresponding to v_1 and v_4 vibration modes of PO_4^{3-} were observed at 962, 604 and 574 cm^{-1} [31]. However, the characteristic bands of carbonate at 870, 1424 and 1457 cm^{-1} (initially observed in Fig. 4) disappeared after sintering up to 1350 °C. The bands detected between 430 and 600 cm^{-1}, with a sharp peak around 520 cm^{-1} are attributed to the bending vibrations generated by the Si–O–Si group [37]. The bands existing at around 930 and 475 cm^{-1} are associated with the symmetric stretching mode of SiO_4^{4-} group [38,39]. The appearance of these bands can be due to the formation of calcium silicate phases, such as wollastonite and dicalcium silicate, during sintering.

The variation in bulk density of samples with different quartz contents sintered at various temperatures is shown in Fig. 8. For samples

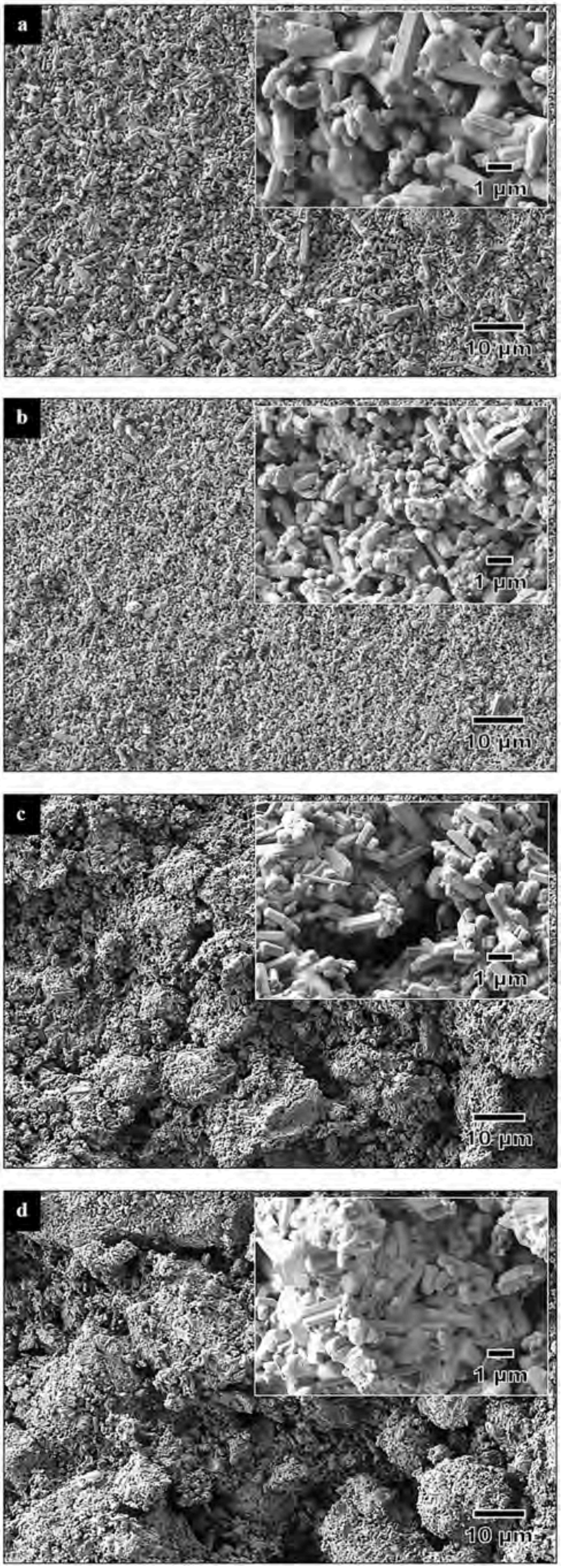

Fig. 9. SEM pictures of composites sintered at 1100 °C: (a) FA2.5Q, (b) FA5Q, (c) FA10Q and (d) FA20Q.

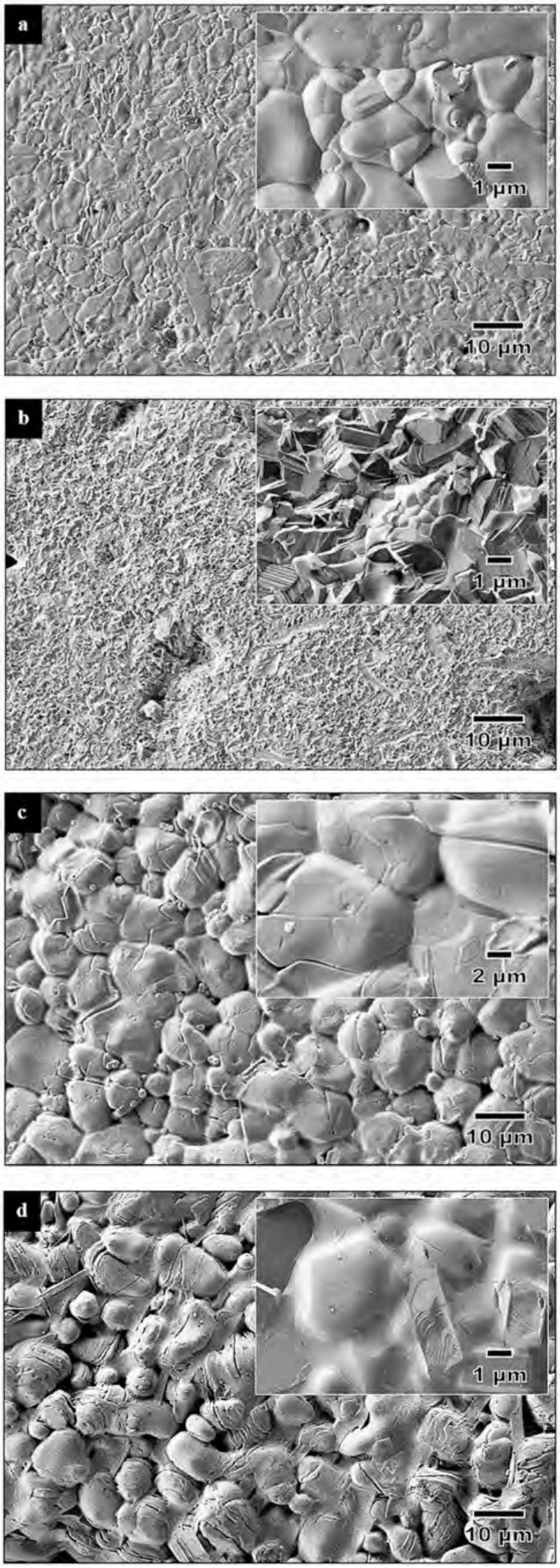

Fig. 10. Comparison of the SEM pictures of composites sintered at 1350 °C: (a) FA2.5Q, (b) FA5Q, (c) FA10Q and (d) FA20Q.

containing up to 10 wt% quartz, the density of the composites increased with the increase in sintering temperature, reached a maximum at approximately 1100 °C, and decreased with the increase in temperature. The composites with the lowest quartz content (FA2.5Q) exhibited the highest density among all the composites regardless of sintering temperature. The maximum density achieved was 3 ± 0.1 g/cm^3 when sintered at 1100 °C. The results suggested that the addition of 2.5 wt% quartz and when sintered from 1050 °C to 1150 °C are effective in enhancing the densification of FAp. Regardless of sintering temperatures, the addition of above 2.5 wt% quartz exhibited low densification. This condition can be attributed to the presence of secondary phases, such as whitlockite and wollastonite, as observed from the XRD analysis. In particular, the FA20Q samples exhibited the lowest densification with maximum bulk density of 2.5 ± 0.12 g/cm^3 measured for samples sintered at 1150 °C. For the Vickers hardness, measurement was only taken for the dense samples sintered at 1100 °C, as presented in Table 2. The hardness varied from 4.32 GPa to 4.67 GPa regardless of quartz addition, thereby indicating that no definite correlation was observed between the hardness and density of the composites.

The FESEM images of composites sintered at 1000 °C and 1350 °C are shown in Figs. 9 and 10, respectively. The morphology of composites evolved from rod-like structure to equiaxed grain morphology when the sintering temperatures increased from 1100 °C to 1350 °C. The composites with high quartz content (i.e. 10 wt% and 20 wt%) and when sintered at 1350 °C exhibited a wetted and smooth appearance of rounded grains. This condition is believed to be due to the excessive liquid phase that was present during sintering and rapidly cooled to room temperature (Fig. 10d). The SEM analysis of samples sintered at low temperature (Fig. 9) revealed a less dense structure, as clearly shown in the inset picture. This condition is in good agreement with the density measurement. However, as the sintering temperature was increased, this was accompanied by a denser microstructure, as shown in Fig. 10.

4. Conclusions

In this work, the effects of quartz addition and sintering temperature on the phase development and properties of natural FAp-sintered composites were investigated. The XRD analysis of the sintered composites indicated that a mix phase was obtained for all composites with FAp as the major phase regardless of sintering temperature. Minor phases of tricalcium phosphate were observed for composites containing 5 wt% and above quartz content. The formation of dicalcium silicate was observed for the sample with 20 wt% quartz addition and sintered at temperatures >1200 °C. This condition was found to have an adverse effect on densification due to the excessive wetting of transient liquid phase during sintering. These findings were supported by the FTIR analysis. This study showed that the addition of 2.5 wt% quartz is found to be effective in enhancing the densification and Vickers hardness of the FAp, particularly when sintered at low temperature of 1100 °C, which is beneficial for biomedical application.

Declaration of competing interest

The authors declare that they have no known competing financial interests or personal relationships that could have appeared to influence the work reported in this paper.

Acknowledgement

This research was supported under the FRGS grant no. FP020-2018A.

References

[1] K.S. Katti, Biomaterials in total joint replacement, Colloids Surf. B Biointerfaces 39 (2004) 133–142.

[2] N. Eliaz, N. Metoki, Calcium phosphate bioceramics: a review of their history, structure, properties, coating technologies and biomedical applications, Mater. (Basel, Switzerland) 10 (2017) 334.

[3] K. Tõnsuaadu, K.A. Gross, L. Plūduma, M. Veiderma, A review on the thermal stability of calcium apatites, J. Therm. Anal. Calorim. 110 (2012) 647–659.

[4] C.Y. Ooi, M. Hamdi, S. Ramesh, Properties of hydroxyapatite produced by annealing of bovine bone, Ceram. Int. 33 (2007) 1171–1177.

[5] G. Muralithran, S. Ramesh, The effects of sintering temperature on the properties of hydroxyapatite, Ceram. Int. 26 (2000) 221–230.

[6] I. Sopyan, M. Mel, S. Ramesh, K.A. Khalid, Porous hydroxyapatite for artifical bone applications, Sci. Technol. Adv. Mater. 8 (2007) 116–123.

[7] S. Ramesh, C.Y. Tan, S.B. Bhaduri, W.D. Teng, I. Sopyan, Densification behaviour of nanocrystalline hydroxyapatite bioceramics, J. Mater. Process. Technol. 206 (2008) 221–230.

[8] M. Safarzadeh, C.F. Chee, S. Ramesh, M.N. Ahmad Fauzi, Effect of sintering temperature on the morphology, crystallinity and mechanical properties of carbonated hydroxyapatite (CHA), Ceram. Int. 46 (2020) 26784–26789.

[9] M. Safarzadeh, S. Ramesh, C.Y. Tan, Hari Chandran, Y.C. Ching, A.F. Mohd Noor, S. Krishnasamy, W.D. Teng, Sintering behaviour of carbonated hydroxyapatite prepared at different carbonate and phosphate ratios, Bol. Soc. Espanola Ceram. Vidr. 59 (2020) 73–80.

[10] B.I. Bogdanov, P.S. Pashev, J.H. Hristov, I.G. Markovska, Bioactive fluorapatite-containing glass ceramics, Ceram. Int. 35 (2009) 1651–1655.

[11] F. Mirjalili, S. Manafi, F. Lotfi, Examination of morphology, degradation and biocompatibility of fluorapatite–forsterite nanocomposite, Ceram. Int. 46 (2020) 21256–21267.

[12] R. Taktak, A. Elghazel, J. Bouaziz, S. Charfi, H. Keskes, Tricalcium phosphate-fluorapatite as bone tissue engineering: evaluation of bioactivity and biocompatibility, Mater. Sci. Eng. C 86 (2018) 121–128.

[13] A. Kenzour, H. Belhouchet, M. Kolli, S. Djouallah, D. Kherifi, S. Ramesh, Sintering behavior of anorthite-based composite ceramics produced from natural phosphate and kaolin, Ceram. Int. 45 (2019) 20258–20265.

[14] B. Nasiri-Tabrizi, A. Fahami, Mechanochemical synthesis of fluorapatite-zinc oxide (FAp-ZnO) composite nanopowders, ISRN Ceram. (2012) 754704, 2012.

[15] B. Nasiri-Tabrizi, A. Fahami, Effect of zirconia content on the mechanosynthesis and structural features of fluorapatite-based composite nanopowders, Ceram. Int. 39 (2013) 7331–7342.

[16] L.J. Fuh, Y.J. Huang, W.C. Chen, D.J. Lin, Preparation of micro-porous bioceramic containing silicon-substituted hydroxyapatite and beta-tricalcium phosphate, Mater. Sci. Eng. C 75 (2017) 798–806.

[17] C. Lin, H. Zhu, Y. Zeng, Sr- and Si-containing bioceramic stimulate in vitro osteogenesis, Surf. Coating. Technol. 365 (2019) 129–133.

[18] A.F. Khan, M. Saleem, A. Afzal, A. Ali, A. Khan, A.R. Khan, Bioactive behavior of silicon substituted calcium phosphate based bioceramics for bone regeneration, Mater. Sci. Eng. C 35 (2014) 245–252.

[19] S.K. Padmanabhan, F. Gervaso, M. Carrozzo, F. Scalera, A. Sannino, A. Licciulli, Wollastonite/hydroxyapatite scaffolds with improved mechanical, bioactive and biodegradable properties for bone tissue engineering, Ceram. Int. 39 (2013) 619–627.

[20] S. Sprio, A. Tampieri, E. Landi, G.C. Celotti, D. Dalle Fabbriche, Bioactive hydroxyapatite/calcium silicate composites obtained by fast hot pressing: structure and flexural strength, Key Eng. Mater. 361–363 (2008) 423–426.

[21] L. Borkowski, A. Przekora, A. Belcarz, K. Palka, G. Jozefaciuk, T. Lübek, M. Jojczuk, A. Nogalski, G. Ginalska, Fluorapatite ceramics for bone tissue regeneration: synthesis, characterization and assessment of biomedical potential, Mater. Sci. Eng. C 116 (2020) 111211.

[22] N. Golafshan, M. Alehosseini, T. Ahmadi, A. Talebi, M. Fathi, M. Kharaziha, G. Orive, M. Castilho, A. Dolatshahi-Pirouzck, Combinatorial fluorapatite-based scaffolds substituted with strontium, magnesium and silicon ions for mending bone defects, Mater. Sci. Eng. C 120 (2021) 111611.

[23] S. Djouallah, H. Belhouchet, A. Kenzour, D. Kherifi, Sintering behavior of fluorapatite-based composites produced from natural phosphate and alumina, Ceram. Int. 47 (2021) 3553–3564.

[24] R.A. Youness, M.A. Taha, M. Ibrahim, Dense alumina-based carbonated fluorapatite nanobiocomposites for dental applications, Mater. Chem. Phys. 257 (2021) 123264.

[25] F.Z. Mezahi, A. Lucas Girot, H. Oudadesse, A. Harabi, Reactivity features of original sol-gel-derived 52S4 glass versus heat treatment temperature, J. Aust. Ceram. Soc. 54 (2018) 609–619.

[26] M. Azami, S. Jalilifiroozinezhad, M. Mozafari, M. Rabiee, Synthesis and solubility of calcium fluoride/hydroxy-fluorapatite nanocrystals for dental applications, Ceram. Int. 37 (2011) 2007–2014.

[27] A. Mokhtari, H. Belhouchet, A. Guermat, In situ high-temperature X-ray diffraction, FT-IR and thermal analysis studies of the reaction between natural hydroxyapatite and aluminum powder, J. Therm. Anal. Calorim. 136 (2019) 1515–1526.

[28] M. Montazerian, J.F. Schneider, B.E. Yekta, V.K. Marghussian, A.M. Rodrigues, E. D. Zanotto, Sol–gel synthesis, structure, sintering and properties of bioactive and inert nano-apatite–zirconia glass–ceramics, Ceram. Int. 41 (2015) 11024–11045.

[29] H. Belhouchet, F. Chouia, M. Hamidouche, A. Leriche, Preparation and characterization of anorthite and hydroxyapatite from Algerian kaolin and natural phosphate, J. Therm. Anal. Calorim. 126 (2016) 1045–1057.

[30] I. Denry, O.M. Goudouri, J. Harless, J.A. Holloway, Rapid vacuum sintering: a novel technique for fabricating fluorapatite ceramic scaffolds for bone tissue engineering, J. Biomed. Mater. Res. B Appl. Biomater. 106 (2018) 291–299.

[31] H.O. Amina Gharbi, A new glance at physico-chemical comportments of silicate bioactive glasses: influence of partial substitution: borosilicate versus fluorosilicate glasses, Int. J. Eng. Innov. Technol. 5 (2015) 74–80.
[32] I. Denry, J.A. Holloway, Low temperature sintering of fluorapatite glass-ceramics, Dent. Mater. 30 (2014) 112–121.
[33] L. Pagliari, M. Dapiaggi, A. Pavese, F. Francescon, A kinetic study of the quartz–cristobalite phase transition, J. Eur. Ceram. Soc. 33 (2013) 3403–3410.
[34] M. Olszak-Humienik, M. Jablonski, Thermal behavior of natural dolomite, J. Therm. Anal. Calorim. 119 (2015) 2239–2248.
[35] B. Nasiri-Tabrizi, A. Fahami, Reaction mechanisms of synthesis and decomposition of fluorapatite–zirconia composite nanopowders, Ceram. Int. 39 (2013) 5125–5136.
[36] N. Böhme, K. Hauke, M. Neuroth, T. Geisler, In situ Raman imaging of high-temperature solid-state reactions in the $CaSO_4$–SiO_2 system, Int. J. Coal Sci. Technol. 6 (2019) 247–259.
[37] N. Betancur-Granados, J.C. Restrepo, J.I. Tobón, O.J. Restrepo-Baena, Dicalcium silicate ($2CaO{\cdot}SiO_2$) synthesized through flame spray pyrolysis and solution combustion synthesis methods, Ceram. Int. 45 (2019) 9589–9595.
[38] P. Mazón, P.N. De Aza, Porous scaffold prepared from α′L-Dicalcium silicate doped with phosphorus for bone grafts, Ceram. Int. 44 (2018) 537–545.
[39] M.F. Zawrah, E.M.A. Hamzawy, Effect of cristobalite formation on sinterability, microstructure and properties of glass/ceramic composites, Ceram. Int. 28 (2002) 123–130.

Abstract

In this work, the sintering behavior of fluorapatite (FAp)–silicate composites prepared by mixing variable amounts of natural quartz (2.5 wt% to 20 wt%) and FAp was studied. The composites were sintered at temperatures from 1000 °C to 1350 °C. The effects of temperatures on the densification, phase formation, chemical bonding, and Vickers hardness of the composites were evaluated. All the samples exhibited mixed phases, comprising FAp and francolite as the major constituents along with some minor phases of cristobalite, wollastonite, dicalcium silicate, and/or whitlockite dependent on the quartz content and sintering temperature. The composite containing 2.5 wt% quartz exhibited the best sintering properties. The highest bulk density of 3 g/cm^3 and a Vickers hardness of > 4.2 GPa were obtained for the 2.5 wt% quartz–FAp composite when sintered at 1100 °C. The formation of carbonated HAp in the in-vitro test " immersion in SBF" confirms that we have bioactive materials. In the second part, the alumina-fluorapatite composites' sintering behaviour from alumina and Algerian natural phosphate was investigated using the conventional sintering method from 1000 to 1600 ° C. Besides; we were studying the effect of titanium oxide (0, 1, 3, 5, and 10%) on these composites' Physico-chemical properties. Sintered samples were examined in terms of formed phases by X-ray diffraction, shrinkage rate, bulk density, open porosity ratio, Vickers microhardness, Tensile strength, and SEM's morphological structure. The results indicated that the addition of titanium oxide effectively improved samples' density, especially those containing 3 and 5%, reaching a value of 3.22 g/cm3, and the percentage of open porosity reached 0,94 and 0,64%, respectively. Also, this study found that titanium oxide has a clear and good effect on microhardness, reached to 13.65 GPa and a Hight fracture strength of about 140 MPa, and using large proportions of additives adversely affects the properties of these composites.

Keywords

Natural phosphate, fluoropatite, quartz, alumina, biomaterials, mechanical properties.

الملخص

تم في هذا العمل دراسة سلوك تلبيد مركبات سيليكات الفلوراباتيت (FAp) المحضرة بخلط كميات متغيرة من الكوارتز الطبيعي (2.5٪ إلى 20٪ وزنا) و FAp. تمت دراسة تأثير درجات حرارة التلبيد على التكثيف وتشكل الأطوار والارتباط الكيميائي وصلادة فيكارز للمركبات. أظهرت نتائج التحليل بواسطة جهاز انعراج الأشعة السينية وجود أطوار مختلفة ، تشتمل على FAp و francolite كمكونات رئيسية مع بعض المراحل الثانوية من cristobalite و wollastonite و dicalcium silicate و/أو whitlockite اعتمادًا على محتوى الكوارتز ودرجة حرارة التلبيد. أظهر المركب المحتوي على 2.5٪ وزنا من الكوارتز نتائج بارزة عند تلبيده عند درجة حرارة 1100 درجة مئوية، حيث تم الحصول على أعلى كثافة حجمية تبلغ حوالي 3 غ/سم^3 وصلادة فيكارز> 4.2 جيغا باسكال، كما يؤكد تشكل الهيدروكسي أباتيت الكربوني في اختبار "الغمر في المحلول الفيزيولوجي" أن لدينا مواد نشطة حيويا. في الجزء الثاني ، تم فحص سلوك تلبيد مركبات الألومين–فلوراباتيت المحضرة من الفوسفات الطبيعي المحلي والألومين المخبري الملبدة من 1000 إلى 1600 درجة مئوية. كما درسنا تأثير أكسيد التيتانيوم (0 ، 1 ، 3 ، 5 ، 10٪ وزنا) على الخواص الفيزيائية والكيميائية لهذه المركبات. تم فحص العينات الملبدة من حيث الأطوار المكونة عن طريق حيود الأشعة السينية ، ومعدل الانكماش، والكثافة الظاهرية، ونسبة المسامية المفتوحة، وصلادة فيكارز، وقوة الكسر، والبنية المورفولوجية. أشارت النتائج إلى أن إضافة أكسيد التيتانيوم أدى بشكل فعال إلى تحسين كثافة العينات ، خاصة تلك التي تحتوي على 3 و 5٪ وزنا من أكسيد التيتانيوم، وبلغت قيمة 3.22 غ/ سم^3، حيث بلغت نسبة المسامية المفتوحة 0.94 و 0.64٪ على التوالي. كما وجدنا في هذه الدراسة أن لأكسيد التيتانيوم تأثير واضح وجيد على الصلادة المجهرية، حيث وصلت إلى 13.65 جيجا باسكال وقوة كسر عالية تبلغ حوالي 140 ميجا باسكال ، وأن استخدام نسب كبيرة من الإضافات يؤثر سلبًا على خصائص هذه المركبات.

كلمات مفتاحية

الفوسفات الطبيعي، الفليوراباتيت، الكوارتز، الألومين، المواد الحيوية، الخصائص الميكانيكية.